FRACTAL ELECTRODES FOR INTERFACING NEURONS TO RETINAL IMPLANTS

by

RICK DANIEL MONTGOMERY

A DISSERTATION

Presented to the Department of Physics
and the Graduate School of the University of Oregon
in partial fulfillment of the requirements
for the degree of
Doctor of Philosophy

December 2014

DISSERTATION APPROVAL PAGE

Student: Rick Daniel Montgomery

Title: Fractal Electrodes for Interfacing Neurons to Retinal Implants

This dissertation has been accepted and approved in partial fulfillment of the requirements for the Doctor of Philosophy degree in the Department of Physics by:

Dr. Miriam Deutsch	Chair
Dr. Richard Taylor	Advisor
Dr. Eric Corwin	Core Member
Dr. Margaret Sereno	Institutional Representative

and

J. Andrew Berglund	Dean of the Graduate School

Original approval signatures are on file with the University of Oregon Graduate School.

Degree awarded December 2014

DISSERTATION ABSTRACT

Rick Daniel Montgomery

Doctor of Philosophy

Department of Physics

December 2014

Title: Fractal Electrodes for Interfacing Neurons to Retinal Implants

With life expectancy on the rise, age-related ailments are a significant strain on the welfare of individuals and the economy. Progress is being made towards combating the leading cause of unavoidable blindness, age-related macular degeneration (AMD). AMD affects ten million Americans and costs the world economy 343 billion dollars annually. Retinal implants promise to restore sight by replacing the eye's damaged photoreceptors with electronic photodiodes. Clinical trials succeed at restoring some vision, but are limited by the stimulating electrodes. We study the electrode-neuron interface with a focus on the geometrical dependence of the electrode.

The functionality of neurons is intimately connected to their branching and curving shape, described by fractal geometry. We examine the morphology of neurons using fractal analysis. The results inform our electrode designs, which are fabricated using top-down lithographic and bottom-up self-assembly techniques.

A novel technique for fabricating a fractal electrode is presented. Heating and cooling a film of poly(methyl methacrylate) on a SiO_2 substrate causes fractal structures to form on the surface. The geometry of the structures is temperature dependent, producing crystalline branches at lower temperatures and diffusion-limited aggregates at higher

temperatures. Subsequent deposition of antimony nanoclusters shows preferred diffusion to the fractal surface features.

The dependence of a photodiode's performance on its top contact geometry is explored using modified nodal analysis. The results reinforce the need to balance a low mean semiconductor-metal separation distance with an adequate contact width for low resistance, all while maximizing light input. Future designs will benefit from the spatial voltage maps produced by the simulation.

The electric field emanating from an electrode is also dependent on the geometry of the electrode. The Faraday cage effect is exploited to achieve similar electric field responses to traditional electrode shapes.

A preliminary study of neural adhesion to SU-8 fractal electrodes is promising. The neuron grows along the electrode even at 90° turns.

The role the fractal geometry plays in neuron and electrode functionality is shown to be significant. Continued study of, and experimentation with, new electrode designs is sure to produce exciting possibilities in the future.

This dissertation includes previously unpublished co-authored material.

CURRICULUM VITAE

NAME OF AUTHOR: Rick Daniel Montgomery

GRADUATE AND UNDERGRADUATE SCHOOLS ATTENDED:

University of Oregon, Eugene, OR
University of Louisiana at Lafayette, Lafayette, LA

DEGREES AWARDED:

Doctor of Philosophy, Physics, 2014, University of Oregon
Master of Science in Physics, 2010, University of Oregon
Bachelor of Science in Physics, 2008, University of Louisiana at Lafayette

AREAS OF SPECIAL INTEREST:

Fractal Analysis
Device Fabrication
Neural stimulation and recording
Cryogenics

PROFESSIONAL EXPERIENCE:

Graduate Teaching Fellow, University of Oregon, 2008–2010, 2014

Graduate Research Assistant, University of Oregon, 2010–2014

GRANTS, AWARDS AND HONORS:

Visiting Scholar, Pufendorf Institute of Advanced Studies, Lund, Sweden 2014

Fellow, Technology Entrepreneurship Program, University of Oregon, 2012

Travel Award to International Conference on Nanoscience and Nanotechnology, Perth, Australia, University of Oregon Physics Departement, 2012

Travel Award to University of Canterbury, New Zealand, National Science Foundation Integrative Graduate Education Research Traineeship, 2011

National Science Foundation Integrative Graduate Education Research Traineeship, 2010–2011

PUBLICATIONS:

R. L. Chamousis, L. Chang, W. J. Watterson, R. D. Montgomery, R. P. Taylor, A. J. Moule, S. E. Shaheen, B. Ilan, J. van de Lagemaat, and F. E. Osterloh. Effect of fractal silver electrodes on charge collection and light distribution in semiconducting organic polymer films, *J. Mater. Chem. A*, 2(39):16608–16616, August 2014.

B. C. Scannell, I. Pilgrim, A. M. See, R. D. Montgomery, P. K. Morse, M. S. Fairbanks, C. A. Marlow, H. Linke, I. Farrer, D. A. Ritchie, A. R. Hamilton, A. P. Micolich, L. Eaves, and R. P. Taylor. Probing the sensitivity of electron wave interference to disorder-induced scattering in solid-state devices. *Phys. Rev. B* 85(19):195319, May 2012.

A. M. See, I. Pilgrim, B. C. Scannell, R. D. Montgomery, O. Klochan, A. M. Burke, M. Aagesen, P. E. Lindelof, I. Farrer, D. A. Ritche, R. P. Taylor, A. R. Hamilton, and A. P. Micolich. Impact of Small-Angle Scattering on Ballistic Transport in Quantum Dots, *Phys. Rev. Lett.* 108(19):196807, May 2012.

ACKNOWLEDGEMENTS

My success in graduate school could not have been possible without the support of my adviser, Professor Richard Taylor. His optimism sustained our scientific progress and his personal philosophy will continue to shape my character throughout my days.

My many attempts to escape my pram were curbed by my family; without them I would surely be lost. Michael and Annette Montgomery, your love and support bridged the distance from Louisiana to wherever I was in the world. Karen Mahoney and Craig Montgomery, you are my Wendy and Michael Darling. Thanks for the adventures. Shawn and Kelli Montgomery, thank you for so gracefully forgiving my absence from far too many family events. Luke, Lane, and Lauren, you three are my fairy dust.

I want to thank Drs. Matt Fairbanks and Billy Scannell for welcoming me into Taylor lab. Matt and Billy trained me in the arts of simulation and experiment. Dr. Ian Pilgrim has been there since the beginning. Our shared interests, which extend far beyond our science experiments, have brought us together as both excellent labmates and friends. Bill Watterson is my prized pupil. You'll be a great dad, Bill. The future of the Taylor lab is safe in the capable hands of Saba Moslehi, Julian Smith, and Michael Dillard.

This is the report of a team of researchers. I could not have accomplished this research without help from the following individuals. Professor Darren Johnson and Kurtis Fairley lent their fabrication expertise for the development of the HafSOx electrodes. Professor John Dalrymple-Alford and Dr. Bruce Harland from the University of Canterbury, New Zealand provided us with the computer models of neurons for analysis. Professor Simon Brown at the University of Canterbury, New Zealand graciously welcomed me into his laboratory to fabricate the fractal electrodes. Drs. Pawel Kowalczyk and Ojas Mahapatras taught me a great many things about microscopes and vacuum chambers. Associate

Professors Christelle Prinz and Maria Thereza Perez, along with Bill Watterson, performed the neural adhesion studies at Lund University, Sweden.

I want to thank Cassandra Niman for our many de-stressing talks over the years. Cassie pushed me in the right direction more than once and helped me find a straight line where I had trouble seeing it myself. Saba Moslehi and Jason Barkeloo untangled a complex problem; let none of us forget to be careful for what you wish. Blake Parris and Ellis Roe were instrumental in the photodiode research. Cooper Boydston played an invaluable role in my understanding of fractal analysis. Shannon Conroy's steady hand and spirit were vital to the electrode analysis.

I want to thank Roger Smith for his unwavering friendship and support and his wavering dance moves. Peter Morse's pep talks carried me through the worst of times. All of my colleagues and friends at the University of Oregon were essential to my happiness. I graciously thank Aimee Todd for encouraging me to turn my questions inward. You prompted an introspection that placed me comfortably between Earth and Neverland. Katherine Zaunbrecher and Douglas Ortego are the best academic family a little brother could ask for (and I never had to). The promise of Stephen Billeaud's gumbo was the afterburner fuel I used to complete this dissertation. From my paran Mitch Fontenot, I inherited my favorite quality: a questioning spirit. Merci, Paran.

I'm very grateful for the many funding agencies that made this research possible. I'd like to thank the following: the Research Corporation for Science Advancement, the National Science Foundation Integrative Graduate Education Research Traineeship, the Office of Naval Research and ONAMI N3 Initiative, and the Pufendorf Institute of Advanced Studies.

This material is based upon work supported by the National Science Foundation IGERT program under Grant No DGE-0549503.

For Paran.

TABLE OF CONTENTS

LIST OF FIGURES

Figure Page

Figure Page

Figure Page

Figure Page

Figure Page

LIST OF TABLES

Table Page

CHAPTER I

INTRODUCTION

During my six years in graduate school, approximately $350\,000$ Americans have been diagnosed with age-related macular degeneration (AMD)[1]. At present, in 2014, more than eight million Americans have an intermediate form of AMD with nearly two million more showing advanced stages of vision loss in the central focusing area of the eye [2]. The expected annual global cost of this disease is significant at 343 billion USD [3]. Another leading cause of blindness, retinitis pigmentosa (RP), is an inherited degenerative disease that affects 1 in 4000 people worldwide [4]. Both of these forms of blindness are due to problems occurring at the layer of photoreceptors in the back of the eye. Researchers have been developing drug therapies to slow and stop the loss of vision from these kinds of degenerative eye diseases [1, 5].

We join a network of researchers that aim to not just stop the loss of vision but to restore it. Stem cells, optogenetics and implantable devices are the three major approaches to restoring vision. Embryonic stem cells have been successfully implanted into human patients with AMD [6]. Visual improvement was reported for the majority of the patients in this study. One of the dangers of implanting stem cells is uncontrolled growth of those cells into tumors. However, the results from this study show medium- to long-term safety. Another approach to restoring vision is optogenetics. Gene treatments hijack ganglion cells in the optic nerve and create photosensitivity [7]. These newly photosensitive neurons absorb light and communicate vision to the brain. Retinal implants are the solution that we choose to pursue. A retinal implant is an electronic device that captures visual information and transmits that information to the brain by stimulating neurons in the eye [8].

The eye is a light sensitive organ that communicates vision to the brain by way of electrically excitable cells called neurons. Over time, the scientific community has developed the ability to reproduce these biological functions. An electronic response to light was first noticed back in 1839 when Edmond Becquerel discovered the photovoltaic effect by placing two electrodes in an electrolytic bath and exposing the setup to sunlight [9]. In 1755, Charles LeRoy was able to elicit a visual response in a blind man by passing current through the tissue of the man's eye [10]. The fields of photovoltaics and neurostimulation have come a long way since these beginnings. In 2000, retinal implants consisting of an array of photodiodes with neurostimulating electrodes were implanted into the eyes of six human patients with RP [11]. Since then a number of clinical trials have been performed on patients with RP or AMD [11–14]. In 2012, the Food and Drug Administration approved the first device for commercial sales in the United States [15].

1.1. Retinal Implants

There are two classes of implantable devices, designated by where the implant is placed in the eye. Epiretinal implants are a multi-unit solution with a camera mounted on a pair of glasses, a computer worn on the hip, and the electrode array implanted in the eye. The camera captures light and sends the information to the computer for processing. The processed visual information is relayed to the epiretinal implant in the eye. The epiretinal implant is an electrode array that sits in front of the retina (in contrast to the subretinal implant), see Figure 1.1. The electrode array is connected to and stimulates the ganglion cells, which pass the signal to the optic nerve. A functioning retina processes a large amount of visual information before the signal is sent to the brain [16]. Because the epiretinal implant bypasses this neural circuitry, the visual information must be processed through computer algorithms before the electrode array is told which ganglion cells to

stimulate. For this reason, using an epiretinal implant requires the patient to wear a camera and a computer, in addition to the invasive operation for implanting the electrode array.

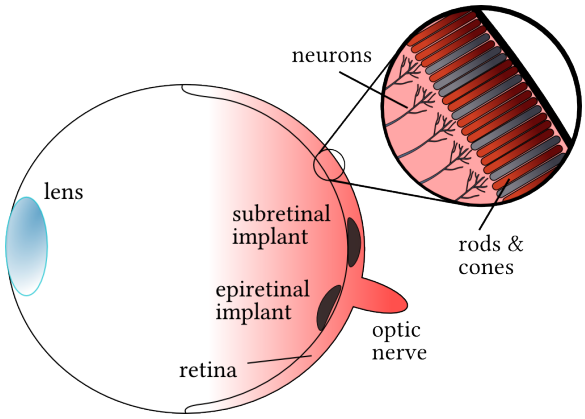

FIGURE 1.1. A schematic of the placement of a retinal implant in the eye. An epiretinal implant sits in front of the retina and stimulates the ganglion cells. A subretinal implant replaces the photoreceptors at the back of the retina and stimulates the bipolar cells. The signal is then processed through the network of bipolar, horizontal, and amacrine cells before being passed onto the ganglion cells and transmitted to the brain via the optic nerve.

Subretinal implants are the second kind of visual prosthesis aimed at stimulating the retinal neurons to restore vision. The subretinal implant is placed at the back of the retina in the space once occupied by the healthy photoreceptors, the rods and cones, see Figure 1.1. This physical location allows the implant to make use of the processing power of the retinal circuitry. The subretinal implant typically consists of an array of photodiodes, each with its own stimulating electrode. A schematic of one such pair is shown in Figure 1.2. The light collected by a photodiode is converted to a current, which acts as the control for a voltage amplifier for the stimulating electrode. Bipolar cells in front of the stimulating electrodes are activated, thus maintaining the spatial information from the incoming light. Once activated, the bipolar cells pass on the visual information

to the brain in their normal, healthy way. This dissertation focuses on the subretinal architecture.

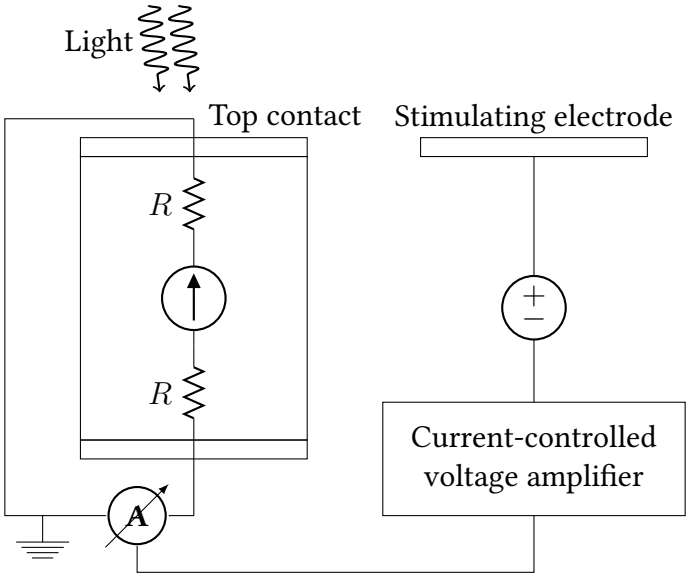

FIGURE 1.2. Schematic of the relationship between the photodiode and the stimulating electrode for a retinal implant. The current of the photodiode operating in short circuit mode is used to control a voltage amplifier that charges a working electrode to stimulate neurons.

The reported visual acuities of patients with retinal implants is much worse than expected by resolving power alone. People with normal visual acuity are said to have $20/20$ vision. For comparison, a person with $20/80$ vision can resolve objects from 20 feet away that a person with $20/20$ vision would be able to see from a distance of 80 feet. A person with $20/20$ vision can discern a gap size (measured as a visual angle) in the Landolt C equal to $1'$, see Figure 1.3. When standing at a distance of 20 feet from an eye chart, 1 arc minute is equivalent to a 1.75 mm gap.

The metric of visual acuity $\mathcal{A}$ is defined as

$$\mathcal{A} = \frac{1}{\theta}, \tag{1.1}$$

where θ is the visual angle in arc minutes. The geometrical relationship (see Figure 1.3) between the visual angle θ, the focal length of the eye f, and the image size d on the retina is

$$\tan(\theta/2) = \frac{d}{2f}. \tag{1.2}$$

For small angles, this relationship is approximated by

$$\tan(\theta) \approx d/f. \tag{1.3}$$

The typical human eye has a focal length of $17\,\text{mm}$. A visual acuity of $20/20$ then corresponds to a distance of $d = 5\,\mu\text{m}$ between the "pixels" at the back of the eye. This distance is between the average size of a photoreceptor ($2\,\mu\text{m}$) and the size of a bipolar cell ($10\,\mu\text{m}$), which is the first processing neuron in the pathway to the brain.

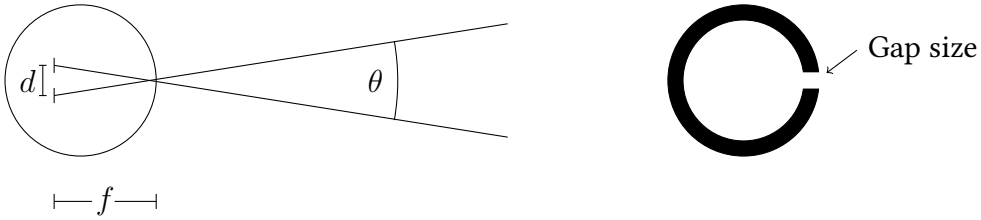

(a) (b)

FIGURE 1.3. Resolving power of the eye. (a) An angular resolution of $\theta = 1'$ is considered normal vision. The average human eye has a focal length of $f = 17\,\text{mm}$, which corresponds to an image size on the retina of $d = 5\,\mu\text{m}$. (b) A Landolt C is used to determine visual acuity. The letter is printed on a chart at various sizes with the gap pointing in different directions. A patient attempts to distinguish which direction the gap is pointing. The visual angle of the smallest gap that was successfully determined is used to measure the patient's visual acuity.

The size of the photodiodes used in subretinal implants is on the order of $20\,\mu\text{m}$, which should correspond to a visual acuity of 20/80. The reported acuity measurements of patients with subretinal implants was no better than 20/1200 [11]. There seems to be something more than pixel density that is limiting the resolution given by a subretinal

implant. It is the working hypothesis of this research team that this low acuity is due to the interconnection between the retinal implant and the neurons. It is the purpose of this dissertation to explore the possibility of creating better interactions between neurons and electrodes by focusing on the geometry of the electrode.

1.2. Outlook

Chapter II introduces the concept of fractal geometry and some tools to characterize fractals. An improved algorithm for analyzing fractals is introduced along with a method for determining the scaling range for certain fractals. The fractal properties of hippocampal neurons from mice are explored using the tools introduced. It is shown that a neuron is fractal because of its branching structure, but the particular quality of the fractal, its fractal dimension, is derived from its curvature.

In Chapter III, we present four fabrication methods for fractal electrodes. A novel self-assembled texturing technique for a polymer substrate is introduced. The fractal dimensions of the resultant fractal geometries are temperature dependent. Metal deposited onto the substrate diffuses to the newly formed textures creating a fractal electrode on an insulating substrate. The deposition of metal onto graphite is also explored as a technique for creating surface features on an electrically conducting substrate. Electron beam lithography is used for the other two fabrication methods. An inorganic hardmask and a photoresist are used to create short and tall electrodes, respectively. These electrodes will be revisited in Chapter IV for their use in neural adhesion studies.

Chapter IV details the roles that fractal electrodes will play in a retinal implant. One use of a fractal electrode is as the top contact of the photodiode, refer to Figure 1.2. A circuit model will be used to explore the electrical performance of two different top contact geometries. Another fractal electrode will replace the traditional stimulating electrode,

again see Figure 1.2. The electric field produced by a fractal electrode is simulated and found to be equivalent to that of a square electrode, but the geometry of the fractal electrode will show promise in our preliminary neural adhesion studies.

There is a statement at the beginning of Chapters II, III, and IV outlining the research efforts of my collaborators.

Due to the various stages of development in the fabrication process and our interest in the role that geometry plays in neural adhesion, the term electrode will be used throughout this document to refer to surface structures even if they are not metallic structures connected to a power supply. For example, when testing neural adhesion to SU-8 surface features on a SiO_2 substrate, we still refer to the device as an electrode.

CHAPTER II

FRACTAL ANALYSIS OF NEURONS

The neuron extraction and imaging described in this chapter was performed by Dr. Bruce Harland at the University of Canterbury, New Zealand. Saba Moslehi and Jason Barkeloo constructed the straightened models of the neurons. Julian Smith generated the ternary fractals. I was the primary contributor to the remainder of the material presented herein.

This chapter introduces the concept of fractals and a number of ways to classify them. A new algorithm for a box counting analysis is presented, as well as a method for determining the domain of length scales over which an object exhibits fractality. These tools are then used to analyze a batch of neurons. The neurons exhibit a narrow range of values for their fractal dimensions. The reason for this is speculated to be the varying curvature of the neuron's branches. Reconstructed models of neurons with straightened branches agree with this reasoning. The projection of a neuron into two dimensions is shown to have the same fractal dimension as the three-dimensional model, but the projection can force a loss of information in the length scale cutoffs.

2.1. Introduction to Fractals

A look around the world provides beautiful panoramas of extremely complex structures. Mountainscapes, cloud formations, and even just the typical tree can make one stop and wonder, in awe, how all of this came about. The explanation behind these three examples of beautiful complexity, as well as plenty of others, lies in a mathematical concept called a fractal. A fractal is an object that exhibits scale invariance. To be scale invariant is to lack the notion of size. It can be impossible to guess the actual size of

some clouds in the sky (without a prior knowledge of meteorology). A large cloud very far away can look just like a small one that is much closer. Likewise, the unfathomable size of some mountain ranges is tied to the presence of many peaks at different heights. Fractals are the scale invariant geometry of trees, clouds, and mountains. The coiner of the term, Benoit B. Mandelbrot, said it best when he titled his book, *The Fractal Geometry of Nature* [17].

Two examples of fractals are shown in Figure 2.1. On the left is a branching pattern that repeats itself exactly at each magnification. On the right, the branching patterns of an actual tree don't repeat themselves exactly, but they do resemble each other. The key to understanding this relationship lies in fractal geometry.

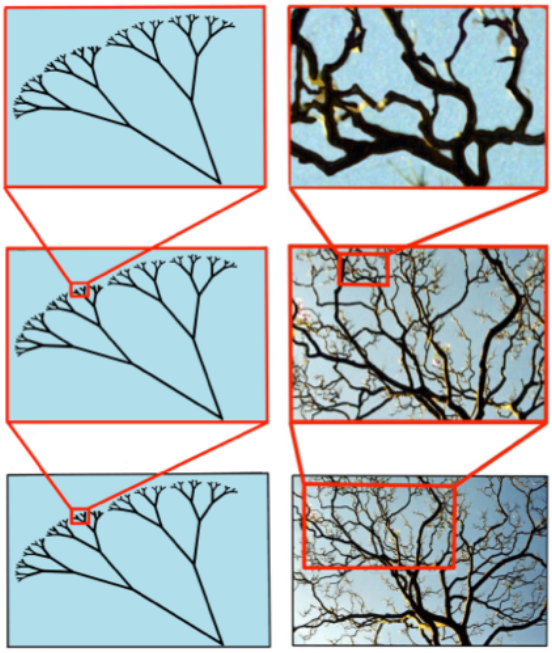

FIGURE 2.1. Two examples of branching fractal patterns. On the left is an exactly self-similar branching pattern that repeats its structure at each magnification. The tree branches on the right are an example of statistical self-similarity. The way in which the patterns occupy space is the same at different magnifications, even if the branching angles are different. Reprinted with permission from the author [18].

Some fractals that will continue to surface through this dissertation include the Sierpinski carpet and Menger sponge, the H tree, and a ternary fractal, all of which are exact fractals. Diffusion-limited aggregates and neurons play the role of the statistical fractals. A variation of the ternary fractal will elucidate one way that exact and statistical fractals can be related.

The Sierpinski carpet is generated by removing the middle third of a square, taking the remaining eight squares and removing the middle third from each of those, and so on. The Menger sponge is analogous to the Sierpinski carpet, but in three dimensions. Divide a cube into twenty-seven smaller cubes and remove the central one, leaving twenty-six cubes whose central pieces are removed at the next iteration, etc. The H tree is grown by sprouting a shrunken H from each of the terminal lines. What we are calling a ternary fractal is not a previously defined fractal, but one generated for this dissertation. It is constructed by letting three lines extend from a point in space. At the end of each line, three shorter lines will extend into a plane perpendicular to the previous line. An example of each of these fractals in their third iteration are shown in Figure 2.2. All of these fractals are generated by performing the same operation, whatever it may be, on the exact same object, but at a smaller length scale.

In Figure 2.3 are examples of statistical fractals. Diffusion-limited aggregation (DLA) clusters and neurons do not follow the same set of shrink-and-add rules that the exact fractals do. They are more organic and involve varying levels of randomness in their construction. DLA is a theory for structure growth based on particles randomly bumping into the main structure and sticking. Neuron growth is much more complex. It is not completely understood yet, but it is known that the dendritic growth is due to both chemical and physical cues [19]. The statistical ternary fractal is generated by allowing

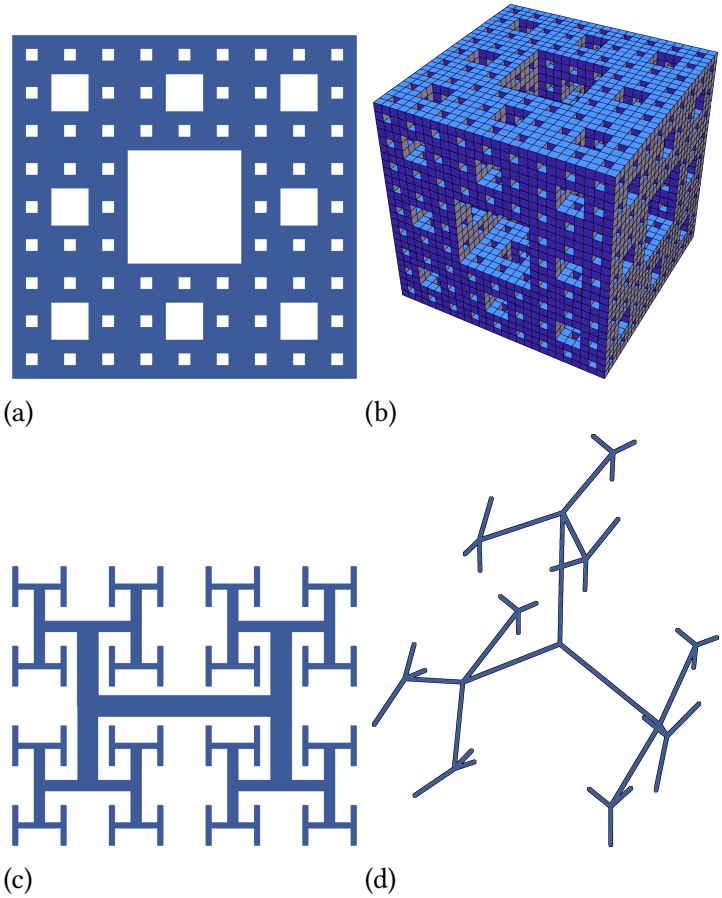

FIGURE 2.2. Four examples of exact fractals each generated to their third iteration: (a) a Sierpinski carpet, (b) a Menger sponge, (c) an H tree, (d) and a ternary fractal.

some randomness to be added to the length of the new lines in the exact generation scheme.

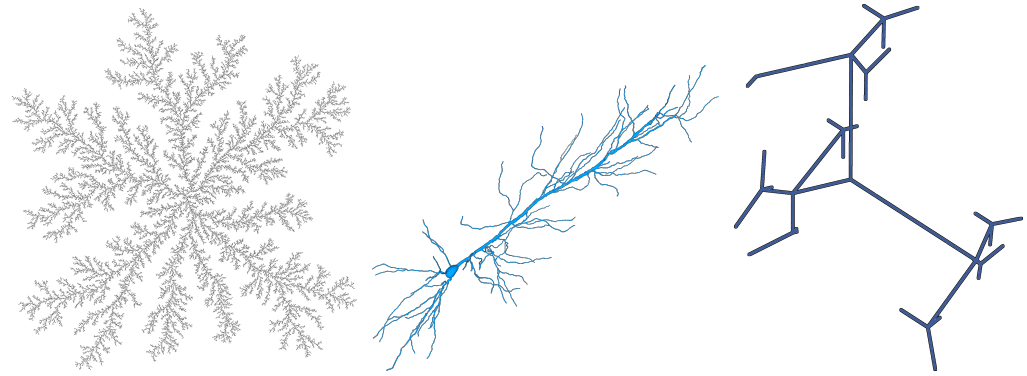

(a) (b) (c)

FIGURE 2.3. Three examples of statistical fractals: (a) a diffusion-limited aggregate, (b) a neuron, (c) and a ternary fractal.

The next section provides a way to characterize these complex objects by their fractal dimension. The box counting analysis is introduced as a way to extract the fractal dimension for a given data set of a fractal.

2.2. Box Counting

Box counting is an analysis method that characterizes an object's physical scaling properties with a parameter called the fractal dimension D_{f}. The fractal dimension provides an understanding of how an object fills space when viewed from different length scales. This method provides a pragmatic approach to estimating the fractal dimension of a visual pattern.

Beginning with an example to build intuition, the dimension of three Euclidean shapes (a line, a square, and a cube) are determined from a box counting analysis. For the one-dimensional line in Figure 2.4, the number of boxes N increases as the box size L decreases in the following way: $N = L_0/L$, where L_0 is total length of the line. For a

square, the number grows as $N = L_0/L^2$. Finally the number of boxes that fill a three-dimensional cube grows by $N = L_0/L^3$ as L is decreased. This leads to the idea of a generalized dimension D that characterizes the scaling relationship in the following way,

$$N \propto L_0/L^D. \tag{2.1}$$

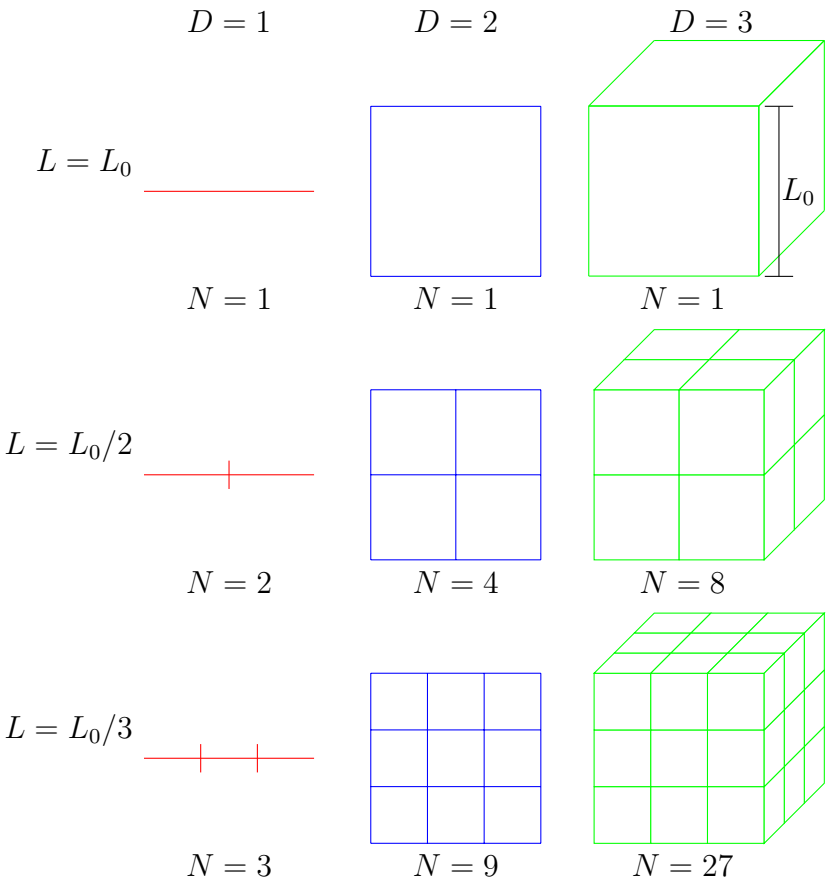

FIGURE 2.4. An intuitive idea of dimension is developed measuring Euclidean objects in one, two, and three dimensions with different size boxes sizes. The number of boxes N that spans the object grows as L_0/L^D, where L is the box size, L_0 is the length of a side of the image, and D is the dimension.

The idea of a generalized dimension can also be applied to more complex systems. Rearranging Equation 2.1 to

$$\log(N) \propto D \log(L_0/L) \tag{2.2}$$

provides an opportunity to extract the dimension D from the graph of $\log(N)$ versus $\log(L_0/L)$. The slope of the log–log plot is the generalized dimension D. The schematic in Figure 2.5 is representative of the power law relationship between the number of occupied boxes and the length scales. For Euclidean objects, D is the integer normally associated with the dimension of that object.

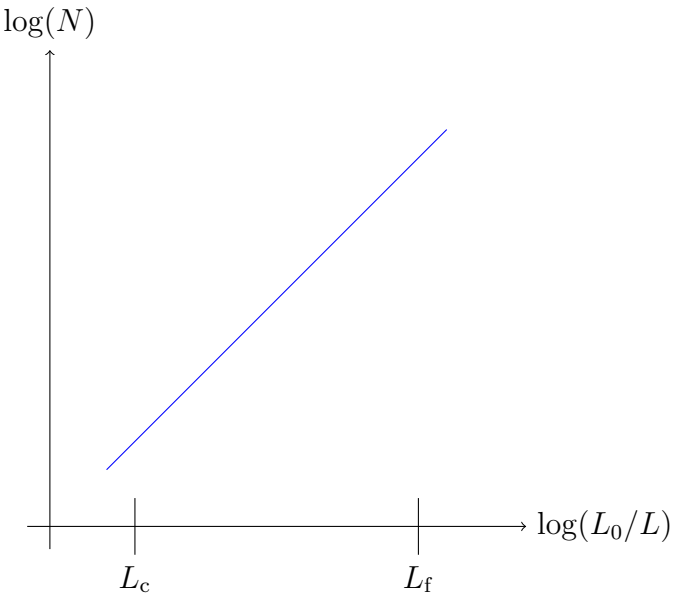

FIGURE 2.5. Schematic of the results of a box counting analysis. The logarithm of the number of occupied boxes is plotted against the logarithm of the box size. The dimension D is given by the slope of the line. The coarser box sizes, denoted by L_c, are on the left hand side and the finer box sizes L_f are on the right hand side.

Performing the same procedure on a fractal object will result in a non-integer D, the fractal dimension D_f. In the following example, box counting is performed on the fractal object that was created by DLA [20] shown in Figure 2.6(a). The $L_0 \times L_0$ pixel image

data is stored in a two dimensional array with a value of 0 representing a white pixel and a value of 1 representing a black pixel. Dividing the image into boxes of side length L, each box that occupies at least one black pixel is counted. Figure 2.6(b,c,d) shows the box counting process with $L = L_0/12, L_0/15, L_0/20$, respectively. The fractal dimension of a diffusion-limited aggregate is $D_{\mathrm{f}} = 1.7$ as shown in Figure 2.7.

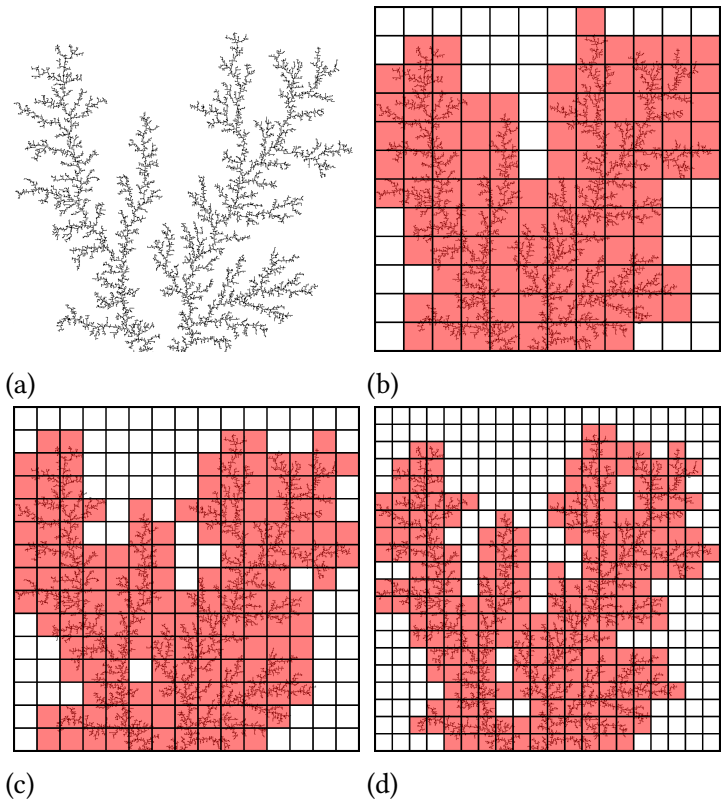

FIGURE 2.6. Example of counting boxes on a diffusion-limited aggregate. As this is a fractal object, the number of colored boxes grows as a function of the box size in a non-integer power.

Fractals that are defined mathematically are scale invariant. However, the scaling behavior of a physically realizable fractal must deviate at some upper and lower bound. These are called limited range fractals. The standard coarse scale cutoff has a limit of $L_{\mathrm{c}} < L_0/5$, such that at least five boxes span the image. The standard fine scale cutoff L_{f} is a box size five times greater than the data resolution. The motivation for this cutoff is that it

takes five points to define a sine curve, which is a minimally simple shape with interesting properties. These standard cutoffs are represented by the vertical bars in Figure 2.7. There has been a debate in the literature over how many orders of magnitude are necessary to describe an object as fractal [21]. Our interest is less in whether or not an object should be called a fractal per se, but whether the fractal analysis provides a meaningful metric on the system.

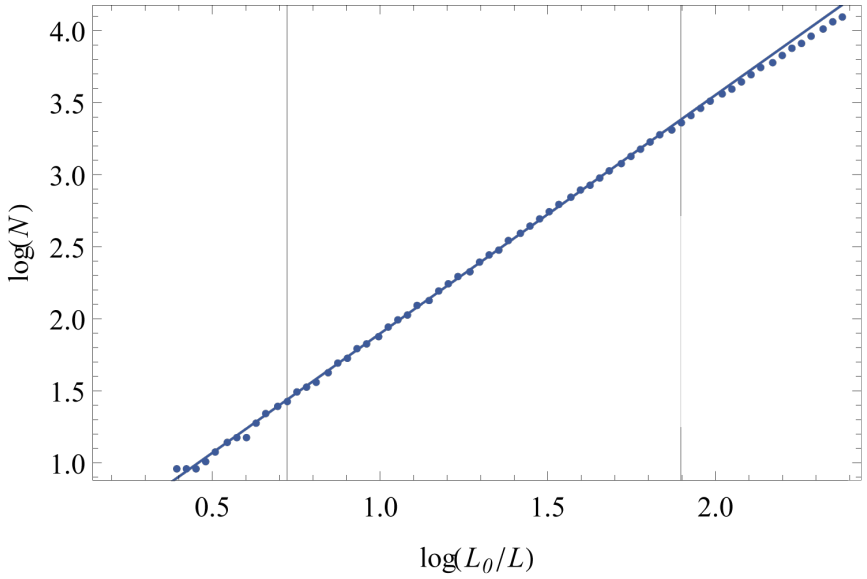

FIGURE 2.7. The scaling plot for the box counting analysis performed on the DLA pattern from Figure 2.6. The slope of the fit line provides a fractal dimension of $D_{\mathrm{f}} = 1.7$. The vertical bars represent the coarse (left) and fine (right) scale cutoffs of $L_{\mathrm{c}} = L_0/5$ and $L_{\mathrm{f}} = 21$ pixels, respectively.

2.3. Binning

The previous algorithm for a three-dimensional box count was a multistep process that recursively divided the image into sets and then recursively traversed those sets, counting the number of data points in each lowest subset. This was a time and resource heavy approach that was applicable only to data sets in three dimensions.

The binning algorithm is a simplified approach that is applicable to any dimension of data. It takes advantage of the binary nature of the black and white image. The image data is stored as a two-dimensional array where every element is a 0 or a 1. This image data can also be stored as a list of the (x, y) coordinates of every occupied element, e.g. $\{(2,1),(3,1),(1,2)\}$. These representations are shown in Figure 2.8. A mathematical operation on the coordinates of the occupied elements reduces the workload of the algorithm.

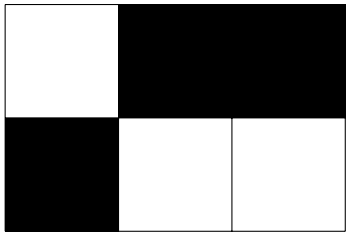

0	1	1
1	0	0

FIGURE 2.8. A simple bitmap image and its data representation.

Consider the one-dimensional image in Figure 2.9. The set of coordinates of the black pixels is $\{2,4,5,9\}$. Starting with a box size of $L_1 = 1$, the count is $N_1 = 4$. Increasing the length of the box $L_1 \rightarrow L_2 = 4$, the count is now $N_2 = 3$, but the relative position of the box is now ambiguous. The boxes are shifted to find the optimal covering, in this case $N_2 = 2$.

To understand this procedure mathematically, begin by taking the ceiling of the set of coordinates divided by the length scale in question,

$$\lceil (\{2,4,5,9\})/4 \rceil = \lceil \{\tfrac{2}{4}, \tfrac{4}{4}, \tfrac{5}{4}, \tfrac{9}{4}\} \rceil = \{1,1,2,3\}.$$

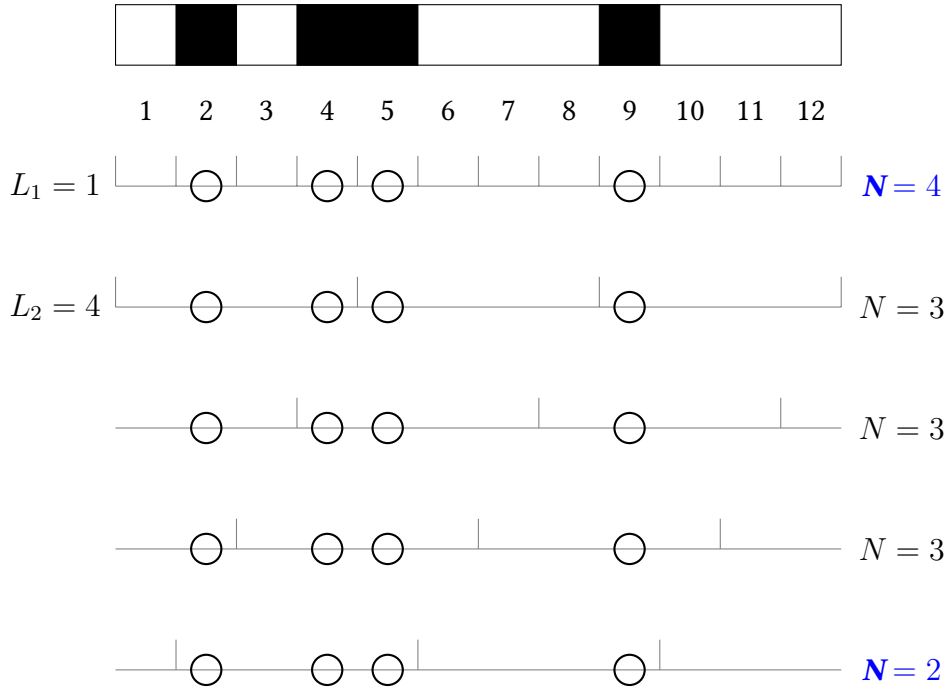

FIGURE 2.9. A representative example of the box counting analysis in one dimension. The data set $\{2, 4, 5, 9\}$ is resampled with a ruler four times longer. The ruler is also shifted relative to the data points to ensure that the minimum number of bins is used to capture all the data.

The shape of the object is dependent on the relative, rather than the absolute, coordinates. Hence shifting the boxes is equivalent to adding an integer to the coordinates,

$$\lceil (\{2,4,5,9\}+3)/4 \rceil = \lceil \{\tfrac{5}{4},\tfrac{7}{4},\tfrac{8}{4},\tfrac{12}{4}\} \rceil = \{2,2,2,3\}.$$

There are $\lceil L_i \rceil$ variations that must be checked for each length scale. At each length scale L_i, each coordinate has three operations performed on it: add an integer, divide by the length scale, and take the ceiling. The number of integers that need to be added is equal to the size of the box (or its ceiling, if it is not an integer). Finally, the duplicates must be removed from the list for an accurate count of N. Overall, this algorithm takes much less time to run than the previous algorithm.

The algorithm is tested on a five iteration Menger sponge. The scaling plot from the analysis is shown in Figure 2.10. The left vertical bar is the standard coarse scale cut off of $L_0/5 = 49$ pixels. The right vertical bar is the standard fine scale cut off of 5 pixels, as a single pixel is the smallest feature size. The best fit line to the data points inside the bars provides the correct fractal dimension for a Menger sponge of $D_\mathrm{f} = 2.7$.

The box sizes are chosen algorithmically to be evenly spaced on a log scale using Mathematica's FindDivisions function [22] between some minimum and maximum. If too many divisions are sought, the data will be oversampled. For example, in Figure 2.10, the staircase pattern on the left side of the graph is from oversampling the length scales. The six largest box sizes are too big to resolve any of the Menger sponge's holes and so count the same number N.

A visual example of the analysis is shown in Figure 2.11. The analysis can be understood as a resampling of the data at various length scales and counting how many pixels are necessary to represent the data at a given length scale. The rescaled Menger sponge is shown at four different box sizes. Note that while the Menger sponge is an

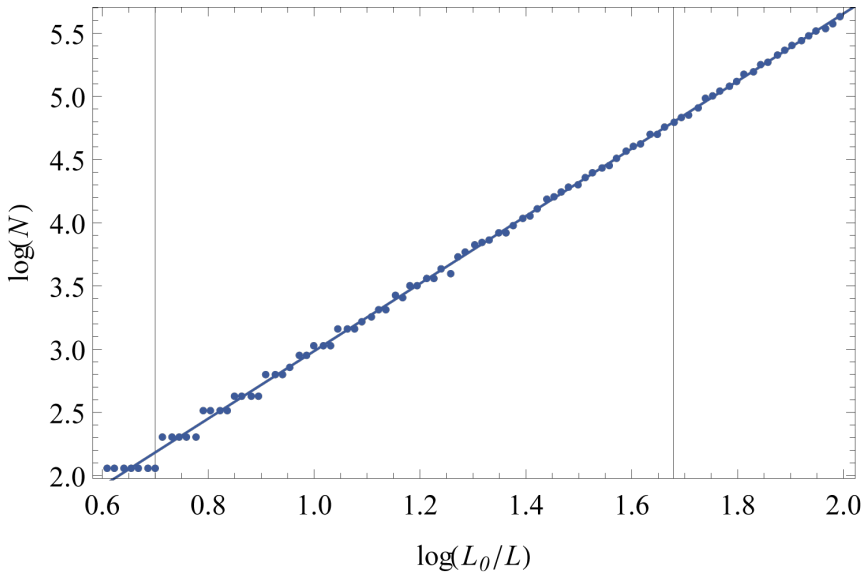

FIGURE 2.10. The scaling plot from a box counting analysis performed on a five iteration Menger sponge. The slope of the fit line provides a fractal dimension $D_{\mathrm{f}} = 2.7$.

exact fractal which repeats itself exactly as the magnification is changed by a factor of $1/3$, the box sizes in the algorithm are chosen to be evenly spaced on a $\log$-scale and therefore will not be whole numbers. This is why the object is misshapen and why the box counting analysis is only an estimate of the fractal dimension.

2.4. Best-of-R^2 Fit

For some fractals, the $\log$-$\log$ scaling plots of objects are not straight throughout the standard scaling range, but they are straight throughout a significant portion of it. The best-of-R^2 fit determines a linear range in the scaling plot and provides a fractal dimension for that region. Linear regressions are calculated for a range of sets of contiguous data points with some chosen minimum number of points. The set with the highest coefficient of determination R^2 is chosen as the set that determines the fractal scaling range.

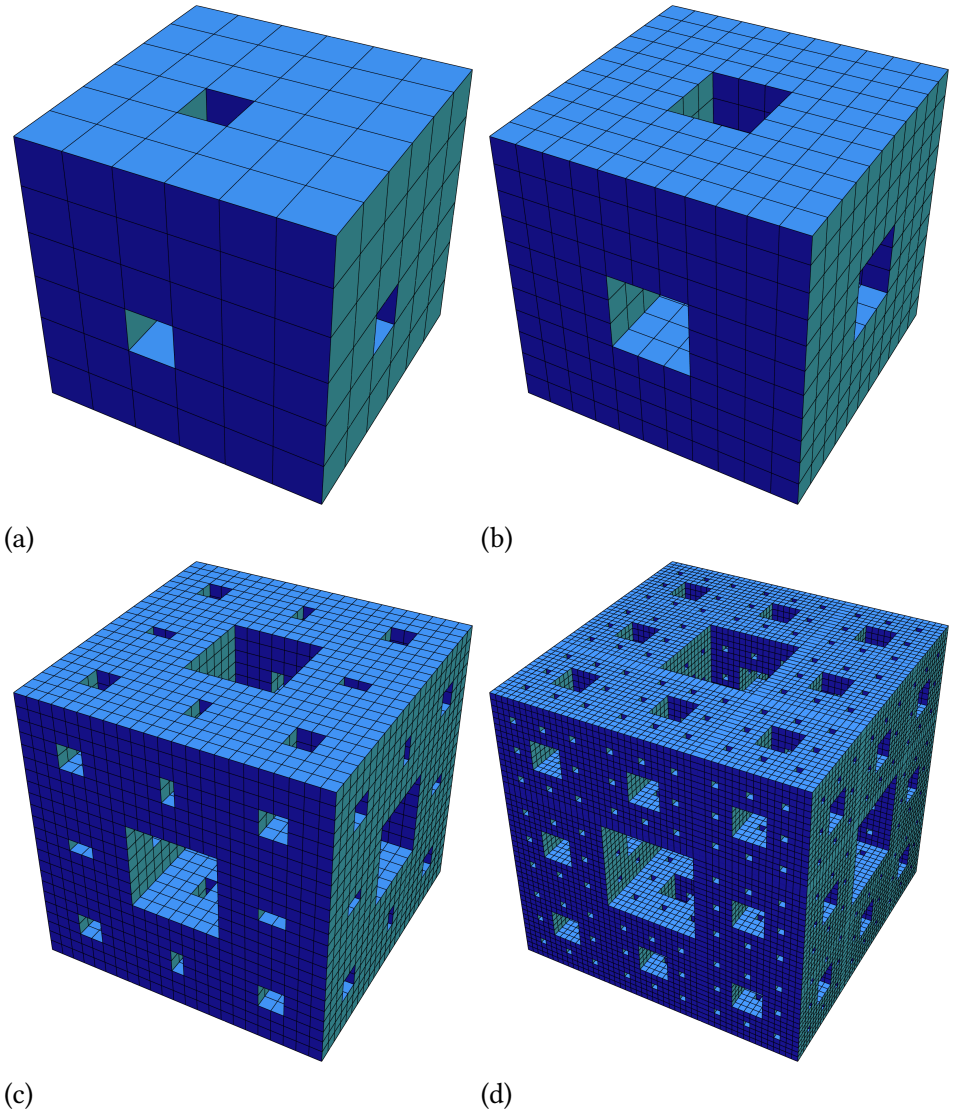

FIGURE 2.11. The visual representation of the Menger sponge at different box sizes: (a) 49 pixels, (b) 23 pixels, (c) 11 pixels, and (d) 5 pixels.

The coefficient of determination R^2 is a measure of the goodness of fit, and is defined by

$$R^2 \equiv 1 - \frac{SS_{\text{res}}}{SS_{\text{tot}}}, \tag{2.3}$$

where $SS_{\text{res}} = \sum_i (y_i - f_i)^2$ is the residual sum of squares, dependent on how far each data point deviates from the given fit, and $SS_{\text{tot}} = \sum_i (y_i - \bar{y})^2$ is the total sum of squares, which is proportional to the sample variance. As the fit line approaches the data, SS_{res} approaches zero. Meanwhile, SS_{tot} increases with each additional data point. There can exist a maximum R^2 that is determined by the balance of these two effects: the benefit to SS_{tot} of additional points and the penalty to SS_{res} because those points are not modeled by the fit. However, this maximum is not guaranteed and the scaling plots must be analyzed with discretion.

This method is tested on the scaling plot of the Menger sponge in Figure 2.10. The linear regression and coefficient of determination were calculated for every set of contiguous data points including at least 30 data points. Figure 2.12 shows the R^2 value for 2015 different fit lines. In this case, a maximum R^2 exists that corresponds to a fit line including 71 points.

The best-of-R^2 fit line and the data points used to determine it are shown in Figure 2.13. The staircase pattern at the coarse scale (on the left) is excluded from the fit, but there is no limit at the fine scale. The lack of a fine scale cutoff in this box counting example is due to a commensurability between the cube-like nature of the Menger sponge and the cubes used to measure it. The fractal dimension from this analysis also provides the correct fractal dimension for the Menger sponge, $D_{\text{f}} = 2.7$.

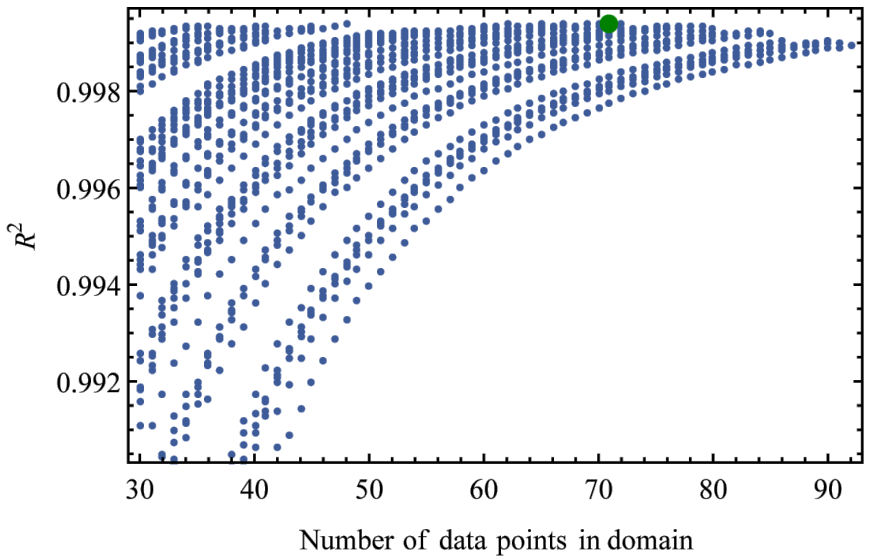

FIGURE 2.12. Plot of the coefficients of determination R^2 from the best-of-R^2 analysis on a Menger sponge. A linear regression was applied to each set of contiguous data points from the box counting analysis (see text) that included at least 30 data points. The highest R^2 value is highlighted in green.

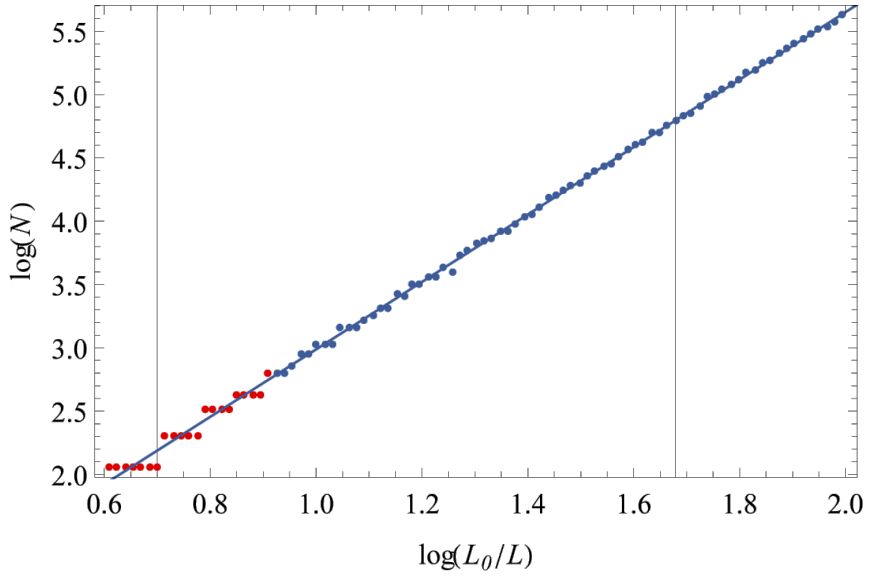

FIGURE 2.13. Scaling plot from the best-of-R^2 analysis on the Menger sponge. The fractal dimension, as determined by the gradient of the fit line, is $D_{\mathrm{f}} = 2.7$. The staircase pattern on the left was excluded by the analysis. The cube-like nature of the Menger sponge matches the boxes used in the box counting analysis in a way that allows the fine scale behavior to extend until the boxes reach a single pixel.

2.5. Neurons

A neuron is a biological cell that responds to electrochemical stimuli and, in response, transmits a signal. There are many different types of neurons, coming in various shapes and sizes, but most are comprise a soma, dendrites, and an axon. The soma contains the nucleus of the cell and acts as the central processing unit of the neuron. The dendrites and the axon branch off of the soma and typically act as multiple inputs and a single output, respectively. This chapter focuses on pyramidal neurons from the CA1 hippocampus of male adult rats. While the framework of analysis presented here is performed on neurons from the brain, a similar approach will be applied to retinal neurons in a future project.

The hippocampus is a region of the brain that plays an important role in memory formation and anxiety [23]. It is also one of the first affected regions in patients with Alzheimer's disease [24, 25]. The early detection of structural changes of the neurons in the hippocampus is an indicator for susceptibility to Alzheimer's disease. For these reasons, it is desirable to understand as much about the geometry of these neurons as possible.

The CA1 pyramidal cell is an important output pathway for long-term memory formation and the development of spatial skills. It is a multipolar cell composed of an apical and basal arbor, each containing many dendrites, and a soma [26]. The apical arbor is named as such because it extends from the apex of the pyramidal soma, with the basal arbor opposite. An example of a CA1 pyramidal cell is shown in Figure 2.14.

The functionality of a neuron is related to its shape [27]. Morphometric parameters like length, surface area, volume, etc. are useful for characterizing distinctive geometries of different neurons. The fractal dimension of a neuron has also been shown to be a useful morphometric parameter that can map the complexity of cortical circuitry through different regions of the brain [28]. An extensive review can be found at [29].

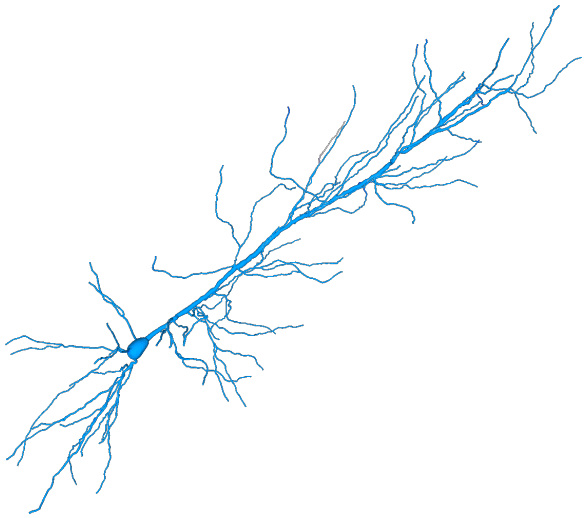

FIGURE 2.14. A CA1 pyramidal cell from the hippocampus of a rat's brain. The soma is the spherical central body. The basal arbor is below the soma and the apical arbor is above.

2.5.1. From Raw Images to Computer Models

A number of steps are involved in analyzing a neuron. After extraction from the rat's brain, the neurons are micrographed and converted into a three-dimensional model. The models are then voxelized for the fractal analysis.

The hippocampus is sectioned into $200\,\mu\text{m}$ slices in the coronal plane (front to back). The sections are stained with a metallic Golgi-Cox stain. This stains $1\text{–}5\,\%$ of the neurons so that their cell bodies and dendritic trees can be visualized. Individual neurons are located using a standard microscope, see Figure 2.15. Because of the large size of the CA1 neurons, a few slides contain a mixture of whole neurons, while most contain basal arbors or apical arbors only.

A Leica laser scanning confocal microscope is used to collect high resolution image stacks for each neuron. The image stacks are created using a $20\times$ glycerol objective with a 0.7 numerical aperture, providing a x and y resolution of $0.378\,\mu\text{m}$. The step size (z distance between image stacks) is $2\,\mu\text{m}$.

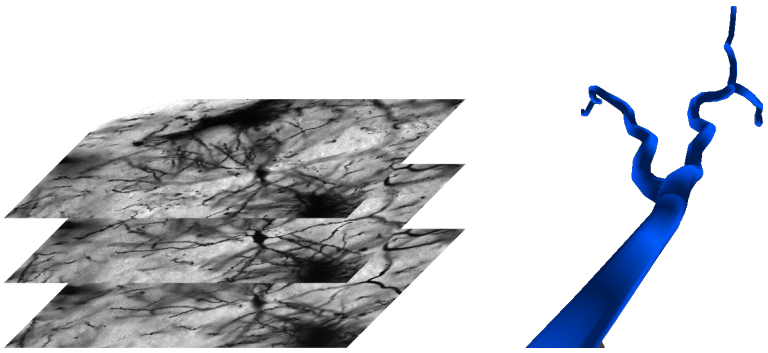

(a) (b)

FIGURE 2.15. Construction of the three-dimensional model of a neuron. (a) Confocal micrographs of a hippocampus. The focal planes are separated by 2 µm. Images taken by Dr. Bruce Harland. (b) A close up of a branching dendrite in the reconstructed three-dimensional model. Figure compiled by the Taylor lab.

The confocal module in Neurolucida[1] converts the layers of pictures into a three-dimensional model. The data can be exported to various formats including the Wavefront .obj format, which played an intermediate role in the analysis here.

The Wavefront files are converted to a voxel data set with a resolution of 4 voxels/µm using binvox[2] [30]. A number of options are available when converting files with binvox. The models are centered inside the bounding box. The model is voxelized "exactly" meaning that if any part of the polygonal model falls inside a voxel, the voxel is added to the list of coordinates. This is in contrast to a more accurate method that uses the graphics card to determine whether a voxel should be occupied. While more accurate, the graphics method limits the object size to $1024 \times 1024 \times 1024$ voxels. Finally, the binary output from binvox is converted to a list of $\{x, y, z\}$ coordinates ready for use with the box counting program written in a Mathematica notebook.

[1] MBF Bioscience.

[2] http://www.google.com/search?q=binvox

2.5.2. Box Counting Analysis of a Basal Arbor

The box counting analysis and best-of-R^2 fit analysis are performed on a basal arbor. The coefficients of determination for each set including at least 25 data points are plotted versus the number of points in that data set in Figure 2.16.

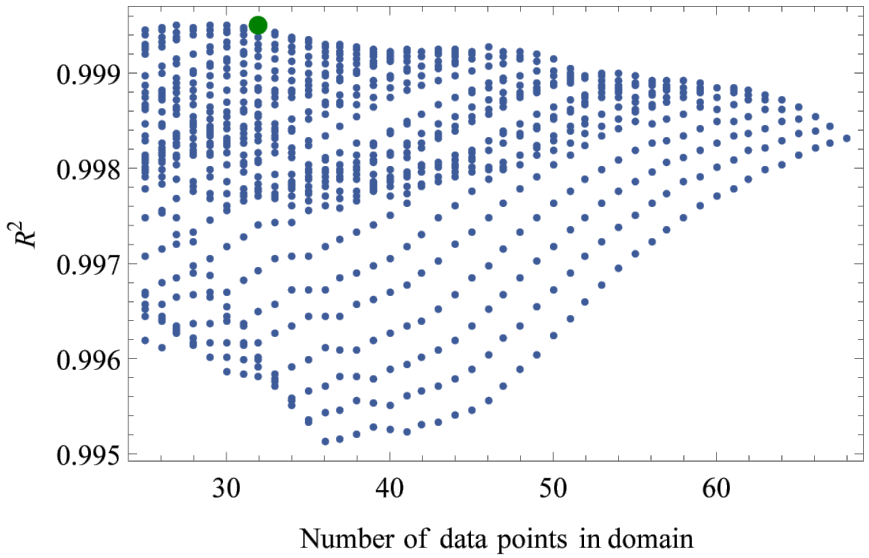

FIGURE 2.16. Plot of the coefficients of determination R^2 from the best-of-R^2 analysis on a basal arbor. A linear regression was applied to each set of contiguous data points from the box counting analysis (see text) that included at least 25 data points. The highest R^2 value is highlighted in green.

The scaling plot is shown in Figure 2.17. The neuron deviates from the fractal behavior, as determined by the best-of-R^2 fit line, at a fine scale cutoff of $L_\mathrm{f} = 3\,\mu\mathrm{m}$, which is slightly larger than the average diameter of its dendrites, which are approximately $1.5\,\mu\mathrm{m}$. The coarse scale cutoff L_c, denoted by the left-most blue point, is $24\,\mu\mathrm{m}$. This value is a little smaller than the statistical coarse scale cutoff of $L = L_0/7 = 32\,\mu\mathrm{m}$. These length scale cutoffs do generally depend on the spacing of the data points and should not be taken as highly accurate values for where the scaling behavior begins and ends. Rather, they should serve more as comparisons between objects that should exhibit the same kind of behavior.

The limiting behavior is as expected. When the box sizes become large enough, all of space will be filled and the slope will tend to $D = 3$. As the box sizes become smaller than $3\,\mu\text{m}$, they begin to resolve the hollow of the cylinder and the gradient becomes 2. At a small enough box size, the analysis probes the connectedness of the data. These data are a set of points, which have $D = 0$.

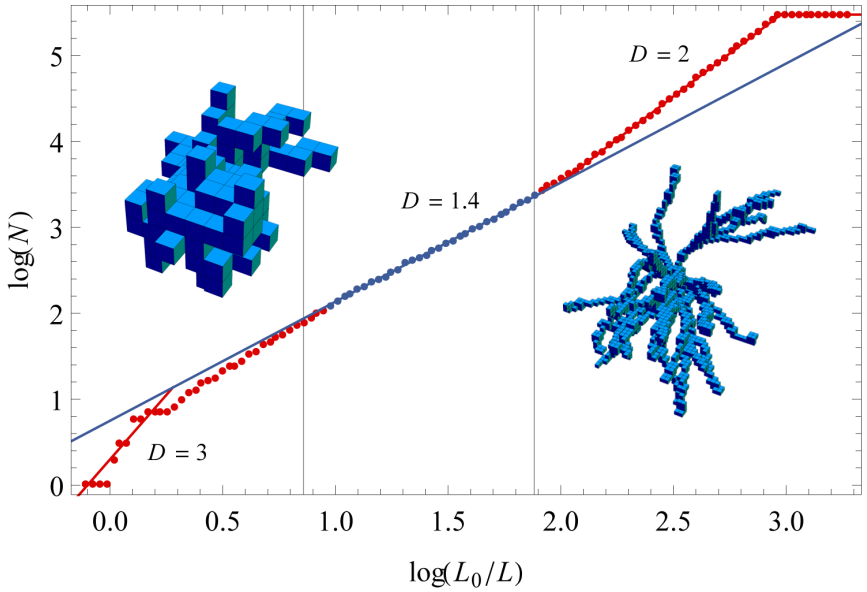

FIGURE 2.17. The scaling plot from the box counting analysis on the basal arbor from a CA1 neuron. The neuron exhibits fractality in the scaling range 3–$24\,\mu\text{m}$ and has a fractal dimension $D_\text{f} = 1.4$, according to the best-of-R^2 fit. The vertical lines denote the statistical coarse (left) and fine (right) scaling limits. The scaling behavior deviates to $D = 3$ at the coarse scale, as expected because the box sizes are so big that they must fill space. Smaller than $3\,\mu\text{m}$, the scaling behavior goes to $D = 2$ as the boxes resolve the hollow cylindrical nature of the dendrites. Once the box size is smaller than the distance between the data points, the scaling behavior goes to $D = 0$, indicative of the point-like nature of the data. It is interesting that the fractal dimension lies between 1 and 2, rather than between 2 and 3.

It is interesting to note that the tangent of the plot data does not smoothly transition from three-dimensional to zero-dimensional behavior. The scaling plot transitions from $D = 3$ to $D_\text{f} = 1.4$ before experiencing another sharp transition to $D = 2$. This is in contrast to a simple fractal, which transitions as a smooth arc. We believe that

these transitions and the length scales at which they occur will be important in future experiments for testing neural adhesion, see Chapter IV.

2.5.3. A Neuron's Projection

Projecting a fractal object into a space with a lower dimension D_p will not change its fractal dimension D_f as long as the fractal dimension is less than the dimension of the space into which it is being projected, $D_\mathrm{f} < D_\mathrm{p}$ [17]. For a neuron, which occupies space in three dimensions and has a fractal dimension of $D_\mathrm{f} = 1.4$, a two-dimensional projection of the neuron should still have a fractal dimension of $D_\mathrm{f} = 1.4$. However, the practicalities involved with imaging neurons can sometimes lead to inconsistency in the results of the fractal analysis [31]. This section will show that although the box counting analysis provides the correct fractal dimension for the projection of these neurons, there is relevant information in the length scale cutoffs that is lost.

The same three-dimensional model of a neuron from Section 2.5.2 was projected into three orthogonal planes. The resulting two-dimensional models were analyzed using the best-of-R^2 analysis, see Figure 2.18. All three projections maintained a fractal dimension of $D_\mathrm{f} = 1.4$, but the fractal scaling regions changed.

Recall that the three-dimensional model exhibited fractality in the range 3–$24\,\mu\mathrm{m}$. The length scale cutoffs from the projections in Figure 2.18 are 2–$13\,\mu\mathrm{m}$, 1–$32\,\mu\mathrm{m}$, and 2–$11\,\mu\mathrm{m}$, respectively.

Focusing first on the fine scale cutoff, projecting the neuron into a plane collapses the hollow of the dendrite. In three dimensions, a box size smaller than $3\,\mu\mathrm{m}$ would begin to resolve the two-dimensional nature of the surface of the cylinder. However, in two dimensions, the hollow is now filled, allowing smaller boxes to be incorrectly counted as filled. The three-dimensional model is a model of the surface of the neuron. Projecting it

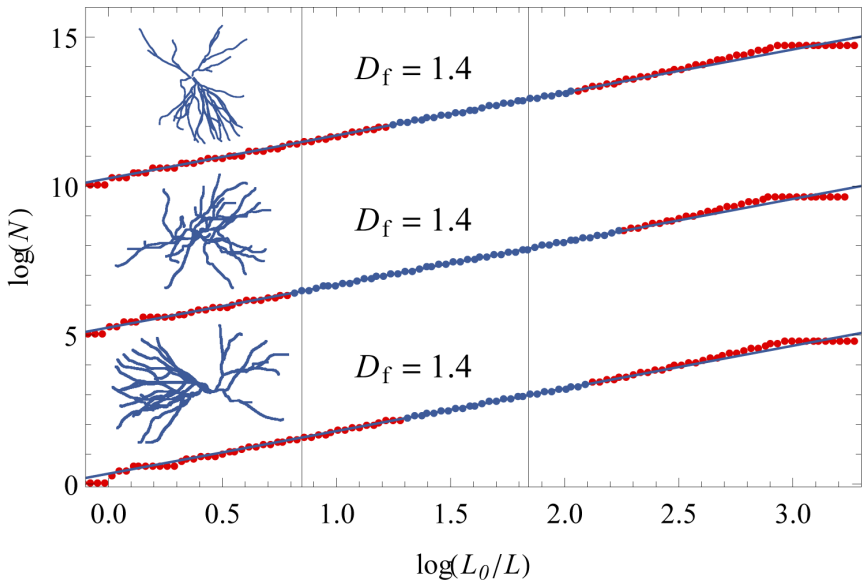

FIGURE 2.18. A basal arbor projected into three different planes. The data shows a fractal dimension equivalent to the 3D analysis of $D_f = 1.4$, but the length scale cutoffs have lost some of their meaning. The data sets are vertically offset for clarity.

into two dimensions creates an object that represents surface area, rather than perimeter. The fine scale limiting behavior of these projections has a slope equal to 1.7. The neuron is beginning to fill more space, but it is still too spindly to reach $D = 2$.

The changes in coarse scale cutoffs are more extreme. In the two cases (top and bottom) where two different arbors can be visually distinguished from each other, the coarse scale cutoff is reduced by half. The counts on the left are low, indicating that the empty space between the two arbors is contributing to the shortened fractality. The head-on view that collapses the two arbors has a coarser cutoff than even the three-dimensional model. This is due to the overlap of dendrites. The empty space that separated the dendrites in three dimensions is now being counted as a filled box in two dimensions. This inaccurately extends the scaling range.

These details are part of the reason why it is important to understand what the box counting analysis is actually measuring. The details of the scaling plot can provide more useful information than just a fractal dimension for an object.

2.6. Similarity Dimension

Before moving onto the self-similarity model, there are three reasons to believe that the box counting analysis is quantifying a genuine fractal quality in the neuron. First, the gradient of the scaling behavior shifts away from $D_{\mathrm{f}} = 1.4$ at the expected scaling limits. Second, the analysis is not simply finding a tangent line in a smooth curve to denote as the straight region. Rather, the data experiences a sharp transition at both scaling limits. Third, the neuron structure and its projection share the same fractal dimension, as expected for a fractal.

To understand where this fractal behavior in the neuron comes from, the self-similarity model will be applied to the neuron. The similarity dimension D_{s} is introduced using a ternary fractal. The methodology of the similarity dimension will then be applied to the neuron. We will see that the self-similarity model does not explain the fractality of the neuron, but there are interesting insights in the analysis.

The box counting analysis can determine the fractal dimension for any fractal. There are some fractals, though, for which a simple self-similarity model can be adequate for quantifying the scaling behavior. The similarity dimension D_{s} of a fractal is calculated by counting how many replicas N have been added at a contraction rate r, using the formula:

$$D_{\mathrm{s}} = \log(N)/\log(1/r). \tag{2.4}$$

There are two different methods for counting N, depending on whether the fractal is forking or branching at each iteration. For fractals such as the Sierpinski carpet, N is

counted via the forking rules. At a given iteration, an existing part is broken into N parts, each smaller by a factor of r. The original square is replaced by $N = 8$ squares that are $r = 3$ times smaller. This provides a similarity dimension of $D_s = \log(8)/\log(1/3) \approx 1.89$. The branching rules dictate counting N in a different way. Take the H tree, for example. The largest H is the zeroth iteration branch. Four Hs are shrunk by a factor of 2 and added to the original H as the first iteration branches. The H tree has a similarity dimension of $D_s = \log(4)/\log(1/2) = 2$.

Consider a ternary fractal expanding into three dimensions, Figure 2.19. Three lines branch from an origin into a plane, separated by 120° each. The line forks into three new lines, which are r times smaller. These new lines lie in a plane that is perpendicular to the previous iteration. The forking rules dictate that $N = 3$. The fractal dimension can be tuned by adjusting the contraction rate,

$$r = N^{-1/D_s}. \tag{2.5}$$

To match the fractal dimension of the neuron $D_f = 1.4$, the length scale should be contracted each iteration by ≈ 0.43.

A statistical fractal can be modeled from this exact one by allowing fluctuations in the length of each new line. An exact and a statistical ternary fractal, both of 6 iterations, are shown in Figure 2.19. The branch lengths of the exact fractal are multiplied by 0.43 at each iteration. For the statistical fractal, the length at each iteration is chosen from a Gaussian distribution, where the mean is determined by the exact contraction rate and the standard deviation is $50\,\%$ of that.

The count N and mean branch lengths $\langle L \rangle$ can be plotted to recover the fractal dimension in a way that is nearly identical to the box counting analysis, i.e. $\log(N)$ vs. $\log(L_0/\langle L \rangle)$. The similarity dimension scaling plot in Figure 2.20 shows a similarity

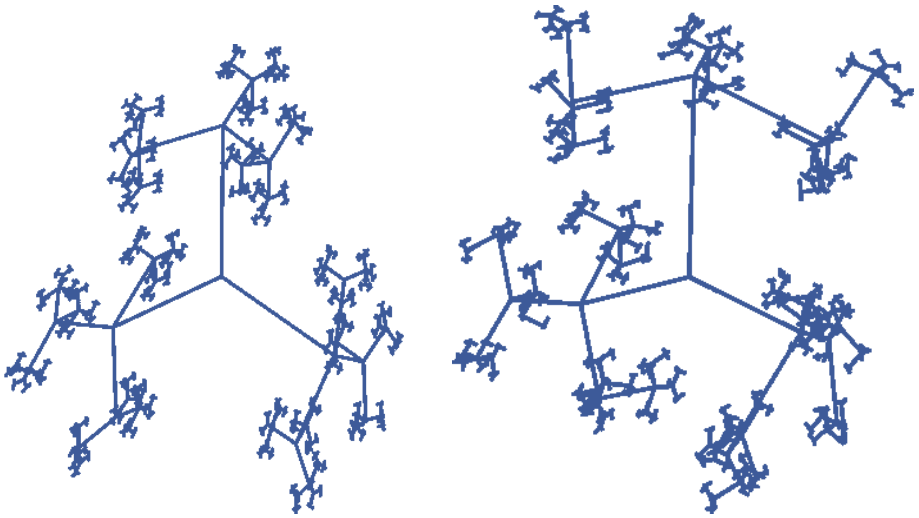

(a) (b)

FIGURE 2.19. (a) An exact ternary fractal and (b) a statistical ternary fractal. They both have a similarity dimension of $D_s = 1.4$. The branch lengths of the exact fractal contract at the same rate for each iteration, while those of the statistical are randomly distributed around a mean that matches the different iterations of the exact fractal. Fractals generated by Julian Smith.

dimension of $D_s = 1.4$ for both the exact and statistical ternary fractals. The variation in branch lengths does allow different iterations to have overlapping branch lengths. That is, some of the third iteration branches will be longer than some of the second iteration branches, etc.

To apply the similarity dimension model to the neuron, the neuron's branches were assigned iteration numbers via the forking rule. Refer to Figure 2.21 for this analysis of the neuron. This is the same rule used in the ternary fractal example. The histogram of the branch lengths shows there are multiple length scales in the neuron but there is no sequence as there is in the ternary fractal. The similarity dimension scaling plot (also in Figure 2.21) shows that this model is insufficent to explain the fractal behavior of the neuron. The branching rules were tested and also found insufficient.

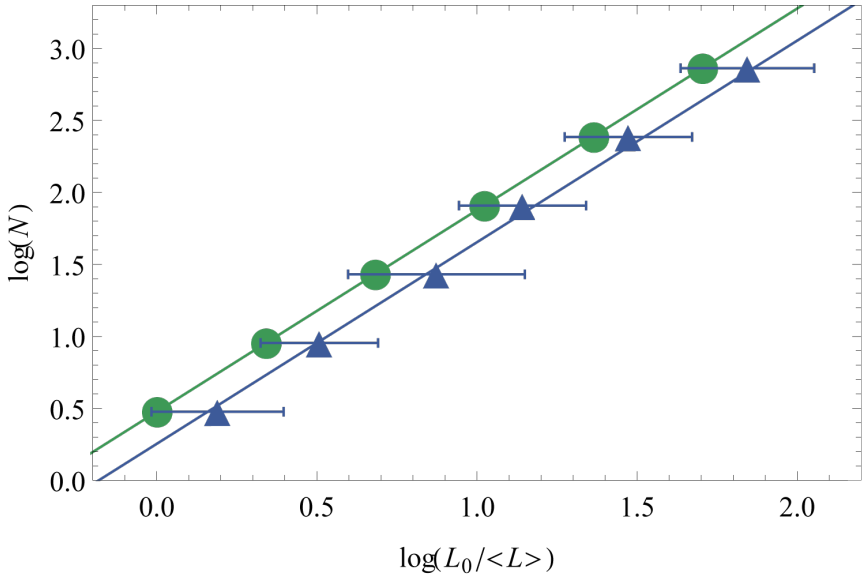

FIGURE 2.20. The similarity dimension scaling plot for the exact (green) and statistical (blue) ternary fractal. The variation in branch lengths does not change the scaling behavior of the means. The statistical data is shifted to the right because the variation introduced into the lengths lets $L_0 > \langle L \rangle$.

The similarity dimension does not provide a meaningful characteristic of the neuron, but the existence of the branches is nevertheless important. The multiple branches are necessary for a neuron to be a fractal, as will be explored in the next section.

2.7. Limiting Iterations

In this section, a certain amount of branching is shown to be necessary to generate the fractal behavior of the neuron. The branching rules are used to assign iteration numbers to the different branches of the neuron.

The rule set here places the longest branches in the zeroth iteration, the next longest branches are in the first iteration, etc. Tracing from the soma, the decision for which path to take at each splitting point is chosen by the path with the longest distance to a terminal branch. In this way, the four branches originating from the soma are the four zeroth order branches. There are 10 first iteration, 10 second iteration, and 4 third iteration branches.

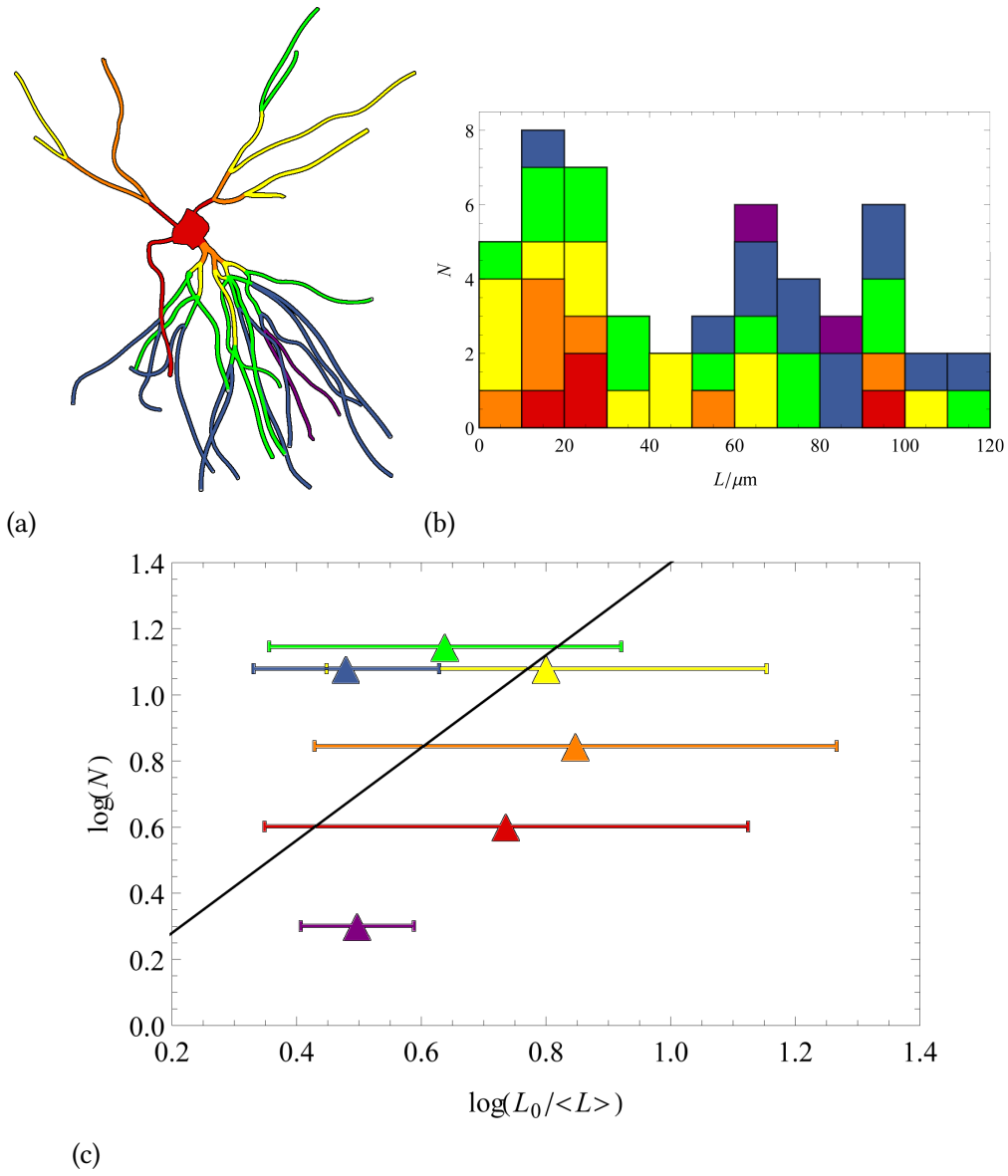

FIGURE 2.21. Simple self-similarity model applied to a neuron. (a) The neuron's branches are colored according to their iteration number under the forking model, from red to purple, through the rainbow. (b) The stacked histogram of the branch lengths for the neuron. The colors are matched to the branch distribution in (a). Note that there are fourth iteration branches (green) at every length scale. This model could still work as long as the mean of those branches follows the power law distribution. (c) The scaling plot for the similarity dimension of the neuron. The number of branches versus the mean branch length at each iteration does not follow a power law. The line demonstrates what a fractal with a similarity dimension of $D_s = 1.4$ would behave like. The self-similarity model does not explain the fractal behavior of the neuron.

The neuron model is analyzed with varying number of included iterations. At low iteration level, the neuron does not exhibit fractal behavior, as is shown in Figure 2.22 by the narrow domain over which the blue data points fit the line. It is only when enough branches have been added in that the scaling plot starts to behave like the object is a fractal.

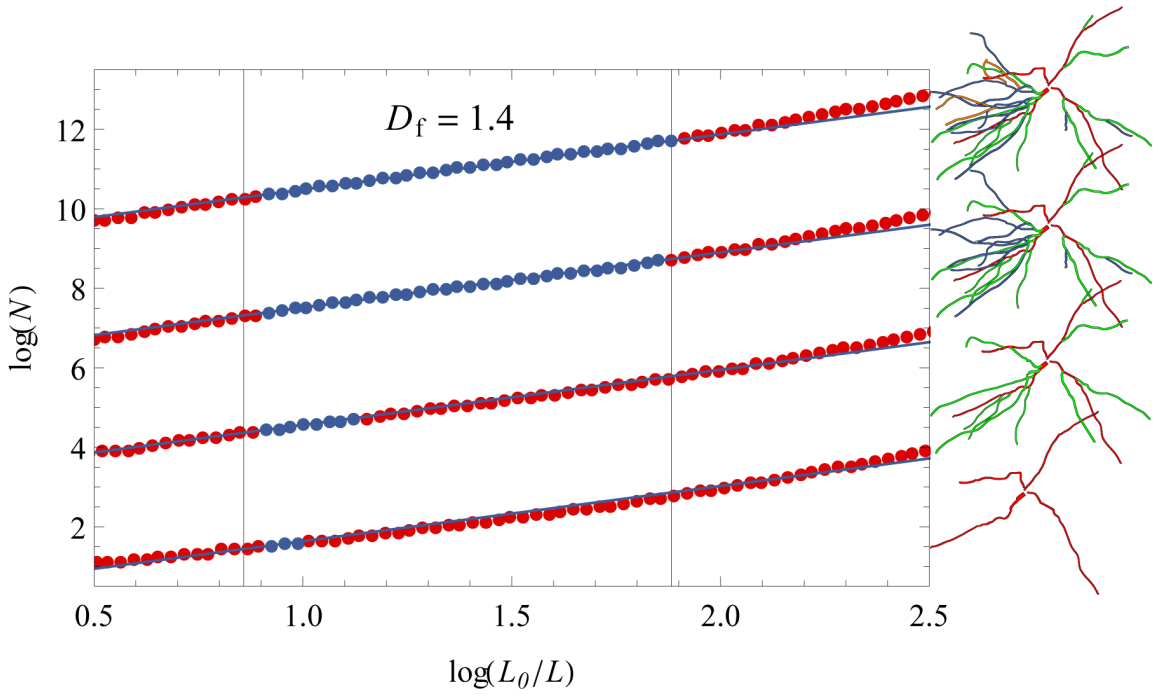

FIGURE 2.22. The scaling plot results for a neuron from its zeroth to third iteration in a branching model. The plots are vertically offset for clarity. The neuron does not exhibit fractal behavior until most of the branches are present in the third iteration.

The fractal behavior does not derive from a simple self-similarity model, but it does require a certain number of branching iterations. The only other option for the origin of the fractal behavior is that the curvature of the branches through space creates the fractal characteristic. In the next section, two neuron models are reconstructed without curves to explore this idea.

2.8. The Dependence of Fractal Dimension on Curvature

Given that the similarity dimension fails to explain the fractal dimension, the remainder of this chapter returns to the box counting analysis. The box counting analysis was performed on 239 basal arbors and 218 apical arbors. The variation in the fractal dimension of these different neuron arbors is shown in Figure 2.23. The basal arbors have a mean fractal dimension of $\langle D_{\mathrm{f}} \rangle = 1.4$, with a standard deviation of $\sigma = 0.03$. The apical arbors also have a mean fractal dimension of $\langle D_{\mathrm{f}} \rangle = 1.4$, with a standard deviation of $\sigma = 0.04$.

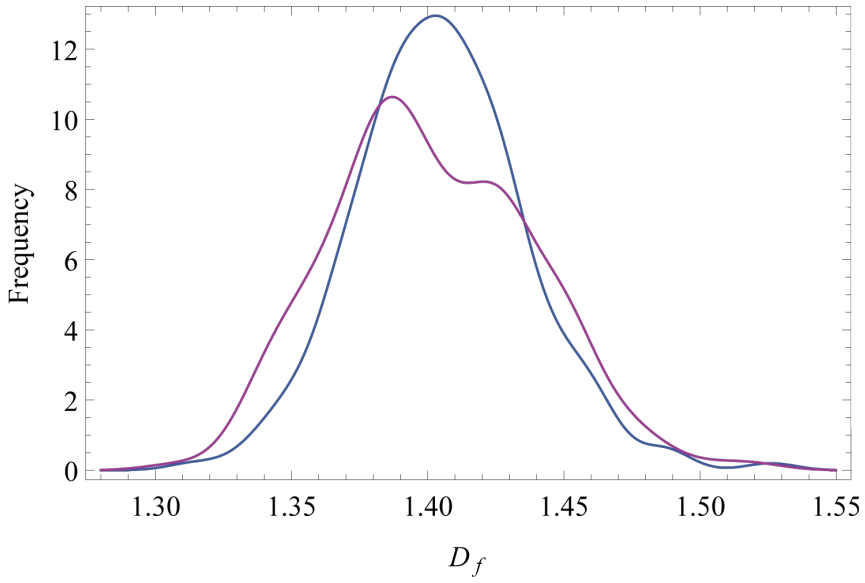

FIGURE 2.23. Smooth histograms of the fractal dimensions of the apical and basal arbors. The variation is due to different levels of weaving.

The working hypothesis is that the variation in the fractal dimension of the neurons arises from different amounts of curvature in the dendrites of the neurons. To test this hypothesis, two neuron models are reconstructed without curves. The branch of a neuron is modeled by a series of connected cylinders whose axes point in slightly different directions. This allows the branch to weave through space. In the reconstruction of

the neuron model, all of the cylinder axes within a branch are set to point in the same direction.

When a branch splits into two, there are two angles that define the new axes, see Figure 2.24. The cross product of the new axes defines a plane. The sweeping angle measures the distance between the two new axes in the plane. The declination angle measures how that plane differs from the originating axis. Each of these angles for the two models were measured using MeshLab[3]. The lengths and angles were then used to construct new models in a CAD program.

In Figure 2.25, we see the results indicating that the fractal dimension of one of the straightened neurons was reduced from $D_{\mathrm{f}} = 1.4$ to $D_{\mathrm{f}} = 1.3$. This reduction in fractal dimension happens because the straightened neuron is filling less space at the finer length scales. The smaller number of boxes needed to resolve the straight lines at the fine scales brings the slope of the line down. However, the fractal dimension of the other neuron was not changed by straightening the branches.

We believe it is the varying levels of curvature in the neurons that account for the spread in fractal dimension of the arbors. The arbors with more tightly packed curves will have higher D_{f} than those which are reaching further away from the soma with straighter branches. It is this closer proximity of branches that is associated with a higher functional capacity in some neurons, but there is still work to be done before the direct link to various processing functions can be drawn from the dendritic morphology [32].

2.9. Summary

The analysis performed on the CA1 neurons in this chapter does not provide the final word on the fractality of neurons. This chapter presents a toolbox that is part of

[3]Developed with the support of the 3D-CoForm project.

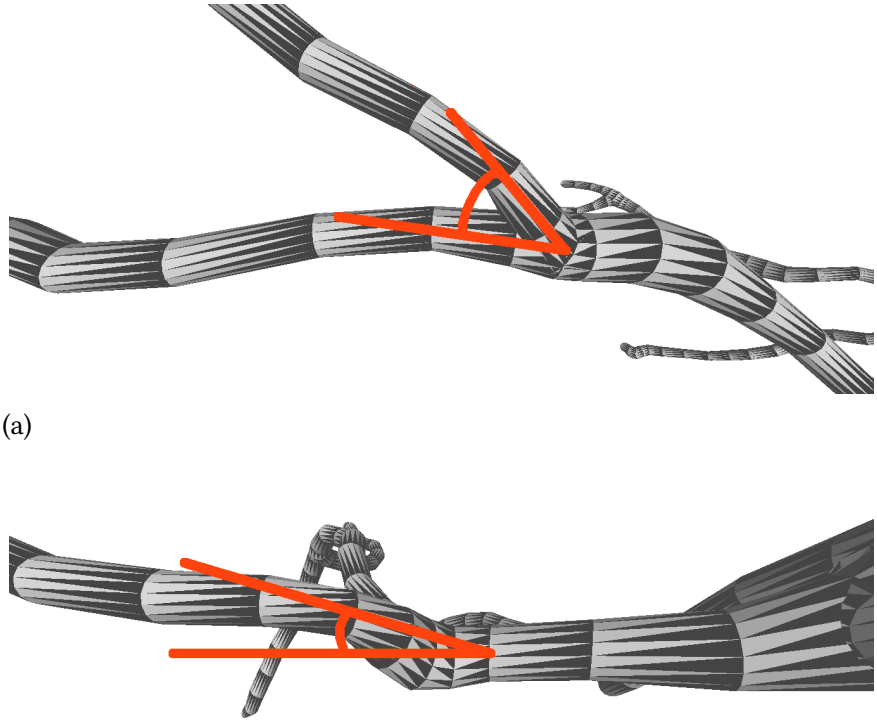

(a)

(b)

FIGURE 2.24. The two angles at a branch point in the original model are preserved in the straightened reconstruction. (a) The sweeping angle measures the distance in the plane created by the cross product of the two axes. (b) The declination angle measures the angle between the old axis and one of the new axes.

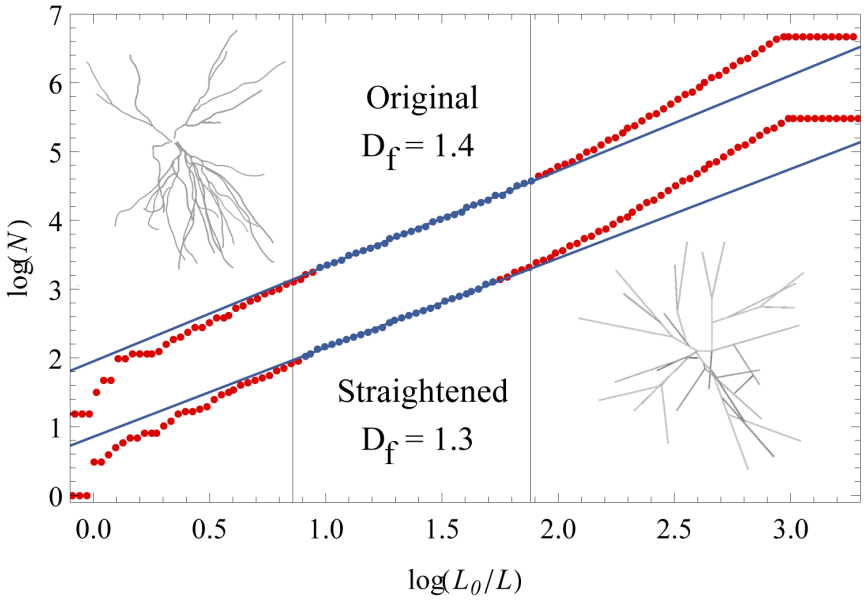

FIGURE 2.25. The scaling plots for an unaltered neuron and a straightened neuron. The data sets are vertically offset for clarity.

a larger picture explaining how to think about neuron morphometrics. Not only is the fractal dimension of a neuron relevant to how it fills space and thus interacts with its neighbors, but also the domain of fractal length scales can provide useful information about the neuron.

The fractal character of a neuron derives from its branching structure, but not in a way that can be accounted for by a simple self-similarity model. The forking and branching models for similarity dimension are insufficient to model the shape of the neuron, but perhaps a hybrid or another model could. The curvature of the dendrites affects the fractal dimension and produces variation within a set of neurons that otherwise behave similarly.

A new algorithm for box counting was developed that provides a significant increase in speed over the previous algorithm used in the Taylor lab and more flexibility than previously published box counting programs, such as FracLac [33], a plug-in for ImageJ [34]. The time saved by the new algorithm allows for more length scales to be examined

and opens the possibility of being more precise in length scale cutoffs. This new algorithm is also dimension-independent. No modifications are necessary to analyze data in one, two, three or n-dimensions.

A method for determining which points should be included in a linear fit was presented. This method provides a systematic way of determining length scale cutoffs so that large sets of fractals can be processed automatically. It should be noted that the error involved with the length scale cutoffs can be significant and this tool should be used more as a comparison between fractal objects, rather than as absolute values.

It was shown that while the projection of a fractal into a lower dimensional space D_{p} preserves the fractal dimension D_{f} (as long as $D_{\mathrm{f}} < D_{\mathrm{p}}$), it can distort the length scale cutoff behavior. When possible, it is best to perform the box counting analysis on the data in whichever dimensional space the object existed in.

With respect to designing electrodes that interact more effectively with neurons, there are two key points that we learned from the fractal analysis. First, the particular way in which the neuron weaves through space has an effect on its fractal dimension D_{f}. This will become even more important when we see in Chapter IV that the neuron shape can be affected by the geometry of an electrode. Second, the fractal dimension of the three-dimensional neuron is the same as that of its projection into two-dimensional space. We are not yet sure of the practical implications of this property, but it might be the case, for example, that a planar fractal electrode with a fractal dimension $D_{\mathrm{f}} = 1.4$ could lead to enhanced adhesion to a neuron.

CHAPTER III

FABRICATION AND CHARACTERIZATION OF FRACTAL ELECTRODES

The electrodes in this chapter were fabricated and characterized by a number of people including Kurtis Fairley, Bill Watterson, Dr. Stephen Golledge, and Shannon Conroy. Kurtis Fairley fabricated the HafSOx electrodes. Bill Watterson fabricated the SU-8 electrodes. Dr. Stephen Golledge assisted with two of the characterization techniques on the Sb-PMMA electrodes. Shannon Conroy assisted with the fractal analysis of the surface features in PMMA. Within the context of their contributions, I designed the electrode geometries, performed the remainder of the Sb-PMMA characterization, developed the fractal analysis and completed the analysis of the surface features in PMMA.

This chapter is focused on the construction of electrodes with fractal surface features. These electrodes are intended to electrically stimulate neurons. Four different approaches to fabricating electrodes will be discussed in this chapter. Two exact fractal designs will be introduced at the beginning of this chapter and revisited in Chapter IV to test their usefulness. The remainder of this chapter will focus on two electrode designs with statistical fractals.

Creating an exact fractal requires a predetermined top-down approach. The benefit to using statistical fractals is that certain growth processes naturally create fractal shapes. By harnessing these growth dynamics, design parameters can be tuned to fit particular applications. An example of each kind of device can be seen in Figure 3.1.

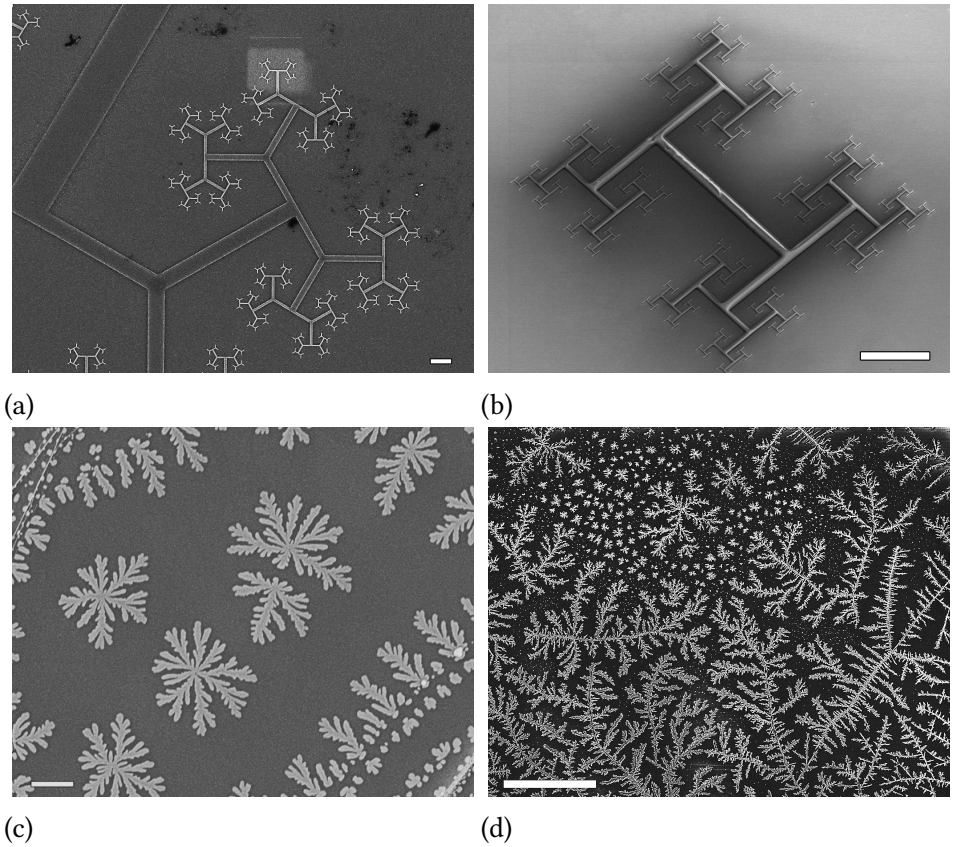

FIGURE 3.1. The four kinds of electrodes presented in this chapter are made of (a) HafSOx, (b) SU-8, (c) Sb-HOPG, and (d) Sb-PMMA.

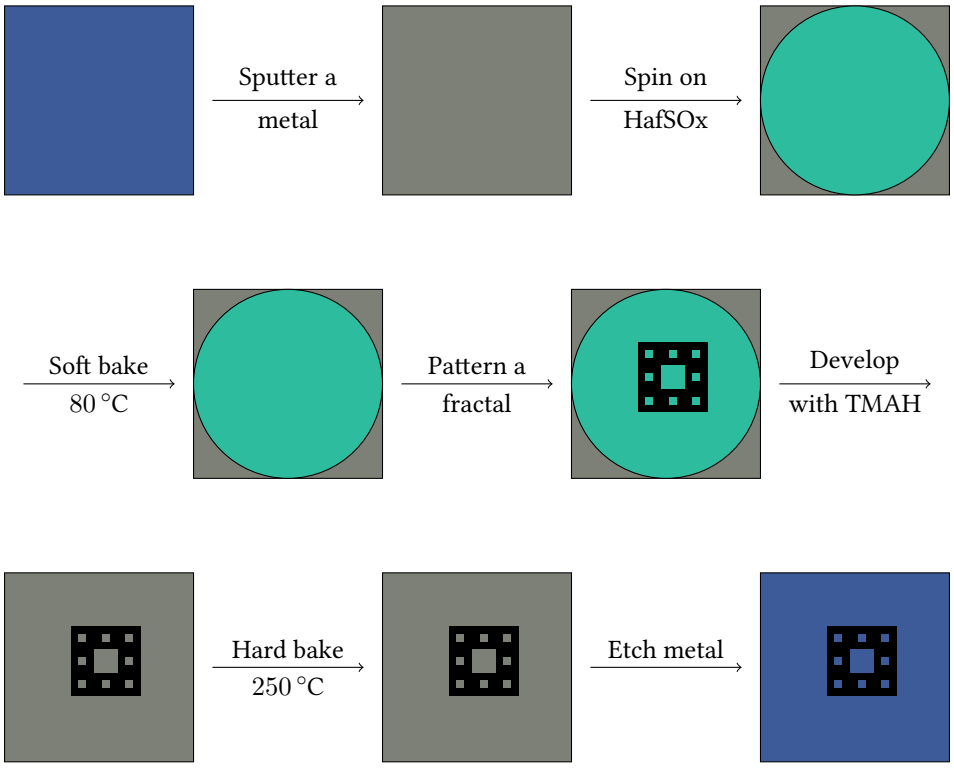

FIGURE 3.2. The flow chart for HafSOx fabrication.

3.1. Exactly Self-similar Electrodes

This section deals with two different electrode designs based on exactly self-similar fractals.

3.1.1. HafSOx Electrode

The HafSOx electrode design is based on a lithographic patterning of the material $\mathrm{Hf(OH)_{4-2x-2y}(O_2)_x(SO_4)_y \cdot qH_2O}$ (HafSOx). The fabrication technique is an electron beam milling process that uses HafSOx as a mask [35]. The final product is a continuous surface electrode with a fractal relief of an exactly self-similar design. While HafSOx has been used to produce very narrow line widths [36], its hardness limits the height of the structures that can be made. A flow chart for the fabrication process is shown in Figure 3.2.

After a metal is sputtered onto a substrate, a $20\,\text{nm}$ layer of HafSOx is spin-coated onto the metal. A soft bake at $80\,^{\circ}\text{C}$ prepares the sample for electron beam lithography. Exposure to the electron beam cross-links the HafSOx, causing it to harden. The unexposed HafSOx is washed away in the developer tetramethylammonium hydroxide (TMAH). The remaining HafSOx structure is hard baked at $250\,^{\circ}\text{C}$. Finally, the metal is etched in a milling process that leaves behind the hardened HafSOx regions on the original substrate. The sample is then ready to be electrodeposited with the electrode metal of choice.

Scanning electron microscope (SEM) pictures of a Sierpinski Carpet and an H tree are shown in Figure 3.3. The five iteration Sierpinski carpet spans $100\,\mu\text{m}$ and has a smallest hole of $19\,\text{nm}$ and has a $D_\text{f} = 1.89$. The H tree is a six iteration fractal spanning $100\,\mu\text{m}$ with a smallest line width of $21\,\text{nm}$. The fractal dimension of this H tree is $D_\text{f} = 1.9$. The fractal dimension of the H tree can be tuned by adjusting the contraction rate, $r = 4^{-1/D_\text{f}}$.

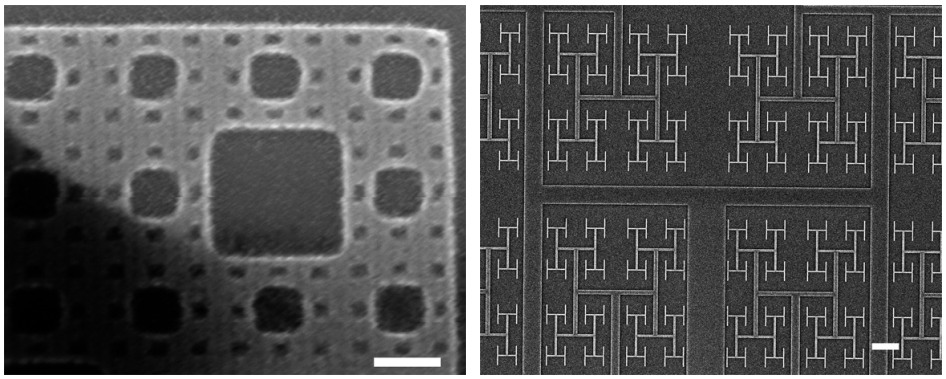

(a) (b)

FIGURE 3.3. SEM photographs of two HafSOx designs. (a) A $100\,\mu\text{m}$ wide five iteration Sierpinski carpet. The smallest hole is $19\,\text{nm}$ and the scale bar is $100\,\text{nm}$. (b) An H tree of $D_\text{f} = 1.9$ that spans $100\,\mu\text{m}$ and has a narrowest line width of $21\,\text{nm}$. The scale bar is $2\,\mu\text{m}$. Images taken by Kurtis Fairley.

A number of different fractal patterns were produced using this technique, including Sierpinski carpets, H trees, angled H trees, arrays of pillars, fractal arrangements of uniformly sized pillars, and square platforms.

3.1.2. SU-8 Electrode

This section details the fabrication of electrodes using SU-8 electron beam lithography, which is capable of making taller structures than the HafSOx technique. This electrode is also designed using a lithography technique but this time with the negative photoresist SU-8. The exposed regions of a negative photoresist are hardened and remain after rinsing the sample in developer.

Four different designs are chosen for SU-8 fabrication. Two H trees of $D_\mathrm{f} = 1.5$ and $D_\mathrm{f} = 2$ are fabricated, as well as a uniform array of the smallest iteration of the H tree. The fourth pattern is a square platform that spans the same area as the other three, approximately $2500\,\mu\mathrm{m}^2$. The three more interesting patterns are shown in Figure 3.4.

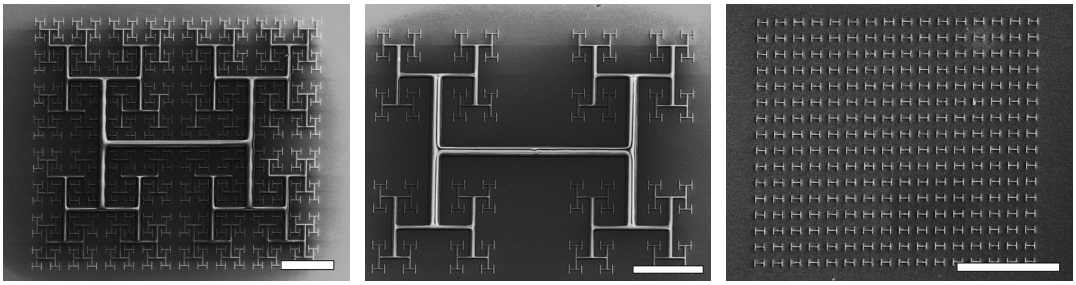

(a) (b) (c)

FIGURE 3.4. Three electrode geometries made using SU-8. (a) A five iteration H tree of $D_\mathrm{f} = 2$ spans an area of $464\,\mu\mathrm{m} \times 406\,\mu\mathrm{m}$. The scale bar is $100\,\mu\mathrm{m}$. (b) A four iteration H tree of $D_\mathrm{f} = 1.5$ spans an area of $560\,\mu\mathrm{m} \times 492\,\mu\mathrm{m}$. The scale bar is $100\,\mu\mathrm{m}$. (c) An array of the smallest Hs used in the previous designs, spanning an area of $550\,\mu\mathrm{m} \times 490\,\mu\mathrm{m}$. The scale bar is $200\,\mu\mathrm{m}$. Images taken by Bill Watterson.

A clean substrate is essential for succesful lithography. The preparation of the substrate wafer includes a $30\,\mathrm{s}$ plasma etch at $150\,\mathrm{W}$ with $30\,\%$ O_2. Spin coating with

nanopure water at 2000 rpm ensures there is no dirt or dust left on the substrate. A few drops of SU-8 2002 are deposited in the center of the wafer with an eye dropper. Slowly ramping the spin coater up to speed can create a more evenly distributed film. The wafer was ramped at 100 rpm/s to 500 rpm for 10 s, before ramping at 200 rpm/s to 2000 rpm for 30 s. This produces a nominal height of 2 μm.

The sample is soft baked in a convection oven at two ramping speeds. First it is heated to 65 °C for 4 min at a ramping speed of 450 °C/h, followed by heating to 95 °C at 8 min at a ramping speeed of 120 °C/h. The patterns are exposed with a 30 kV electron beam with a current density of 0.5 μC/cm^2, using a 7.5 μm aperture. There is also a post exposure bake using the same ramping rates and temperatures as the soft bake. The sample is sonicated in SU-8 developer for 60 s. An additional 30 day hard bake at 150 °C was performed on some samples.

SU-8 lithography is a well-studied and robust fabrication technique that will be relied on for future electrode development. It can provide a wide range of structure heights (0.5–100 μm) and a high aspect ratio for those structures [37].

3.2. Statistically Self-similar Electrodes

The remainder of this chapter will focus on the development of electrodes with fractal geometries of a statistical nature. Recognizing that the intended counterpart to these electrodes are neurons, the fabrication of electrodes that match the fractal properties of the neuron seems sensible. Two different approaches are taken. The first is a technique that harnesses DLA, a growth process that has been studied in great detail [20, 38]. The second approach employs a novel polymer supercooling technique [39] to create fractal structures of varying fractal dimension based on the temperature gradient.

3.2.1. Sb-HOPG Electrode

The fabrication technique discussed here is called nanocluster deposition [38, 40]. Nanoclusters of a metal are evaporated from a crucible and deposited onto a substrate. The resultant structures are described by the theory of DLA. Variables such as deposition rate and total amount of material deposited can be tuned to control different features.

The experiment is performed in a high vacuum deposition chamber, see Figure 3.5. This is a three stage vacuum chamber. A roughing pump evacuates the system to a pressure suitable to be exposed to a sorption pump, approximately 10 mTorr. The sorption pump is a cylinder containing a molecular sieve. The pump is submersed in liquid nitrogen, dropping the pressure along with temperature, see Figure 3.5. Once exposed to the higher pressure of the deposition chamber, the pressure gradient draws particles into the sorption pump that are then trapped in the molecular sieve reducing the pressure. The sorption pump reduces the pressure to levels suitable for the ion pump, e.g. 10^{-5} Torr. The ion pump is a high voltage capacitor wrapped in a large electromagnet. The large electric field produced by the capacitor plates ionizes any particles remaining in the chamber. These ions are then accelerated in the magnetic field, circling inside the ion pump until they reach the outer wall, also made of titanium, and are trapped there, again reducing the pressure. With a clean and well dehydrated chamber, the ion pump in this system can reach pressures as low as 10^{-9} Torr.

There are many considerations in the construction of a deposition chamber such as this. No plastics can be used inside the chamber, as they will continue to outgas, preventing the chamber from reaching a suitably low pressure. The lack of plastic requires clever solutions to problems such as keeping electrical wires, for say, button heaters or thermocouples, from shorting. This problem is exacerbated by the need for the electrical components to be able to move along with the sample holder from the loading chamber

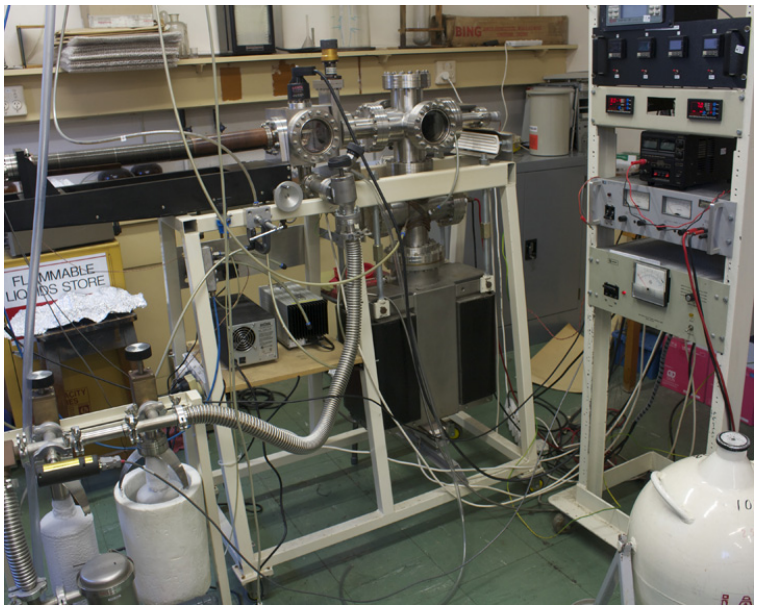

FIGURE 3.5. A high vacuum deposition chamber. A roughing pump (not shown) and the sorption pumps (bottom-left) prepare the chamber to pressures suitable for the ion pump (center). The samples are maneuvered into position using the accordion sleeve design. The electronics rack (right) houses the power supply for the crucible heating and the barometer readouts.

to the deposition chamber. An accordion sleeve design allows flexibility in the chamber setup but must be adjusted with caution to avoid shorting the electrical components.

Pressures near atmosphere are measured with a digital barometer and a cold cathode ion gauge is used for the lower pressures. The sample holder is equipped with two button heaters and two thermocouples. Above the sample holder, there is a high temperature incandescent light bulb. In order to get clean diffusion on the surface of a sample, it is necessary to remove any adsorbates, such as water molecules, before depositing the chosen material. The button heaters and incandescent light bulb are used in conjuction to remove the adsorbates.

The metal is sublimated from a ceramic crucible (see Figure 3.7) in the 4-way cross located between the 6-way cross and the ion pump. The 4-way cross is separated from the 6-way cross by baffles that collimate the sublimated particles into a beam. The deposition

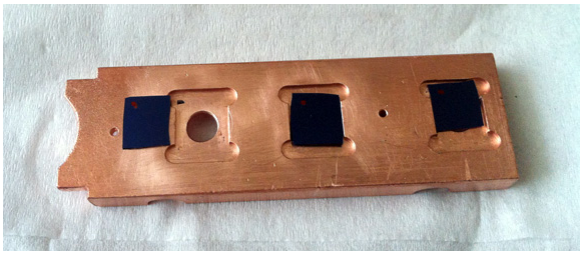

(a)

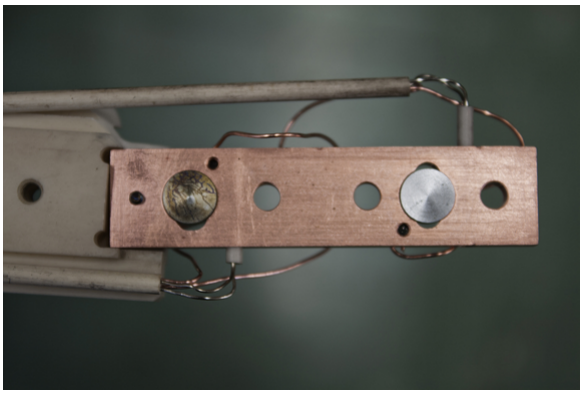

(b)

FIGURE 3.6. The sample holder and the support arm. (a) The sample holder shown from above with the samples face down. (b) The support arm for the sample holder is shown from below with two button heaters (circles) and two thermocouples (cylinders).

material is sublimated using resistive heating of the ceramic crucible by a power supply that can deliver up to 15 A of current. The 4-way cross is also wrapped with watercooling copper pipes to ensure the chamber does not overheat.

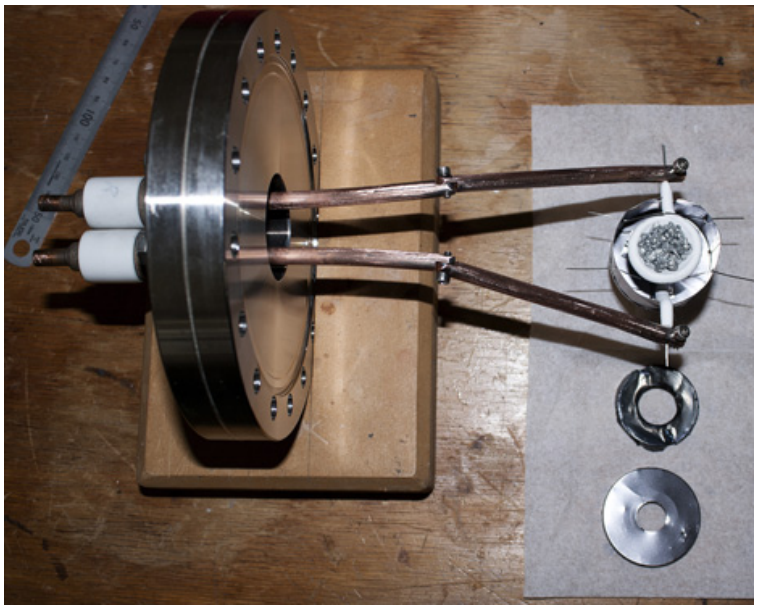

FIGURE 3.7. A ceramic crucible is resistively heated to evaporate the antimony (or bismuth) it holds.

The metal vapor is collimated through a baffle and deposited on a substrate, in this case highly-oriented pyrolitic graphite (HOPG). The sample is mounted face down in the sample holder, as shown in Figure 3.6. The metal is deposited through a hole with a diameter of 3 mm. A schematic view of the deposition chamber is shown in Figure 3.8.

In the sublimation of bismuth (Bi) and antimony (Sb), the typical molecule emitted from the crucible is Bi_2 or Sb_4 [38]. Given the smoothness of the substrate, these nanoclusters diffuse along the surface until encountering another nanocluster, a defect, or a step-edge in the graphite. The clusters continue to aggregate, creating geometries that are dependent on the material being deposited, and the lattice structure of the substrate. Bi forms rods [41] and Sb, which is the focus of this section, forms branched, dendritic

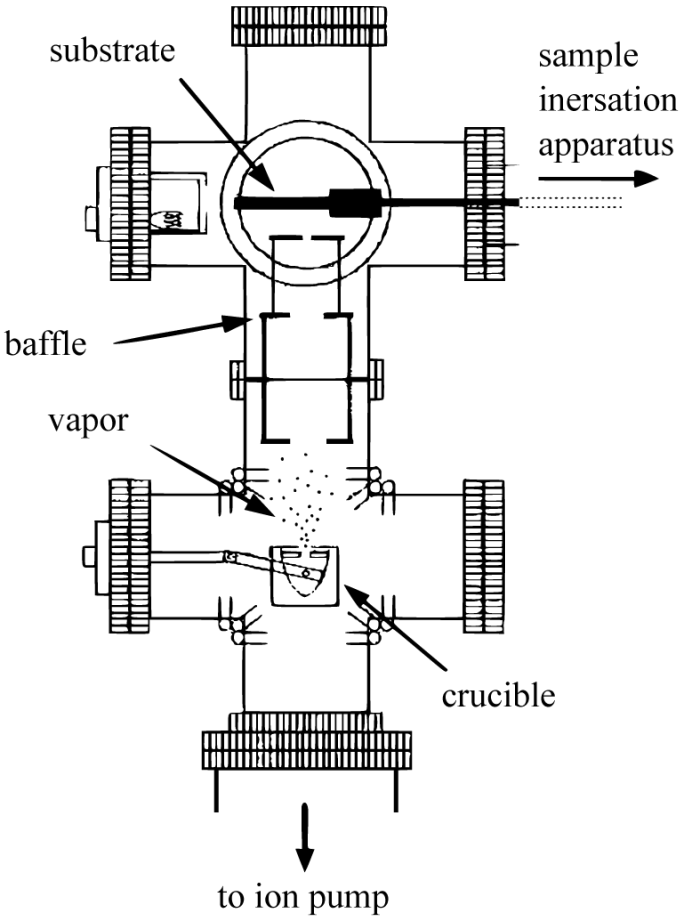

FIGURE 3.8. A schematic of the nanocluster deposition apparatus. Once the ion pump has reduced the pressure to a suitable range (10^{-6}–10^{-7} Torr), the crucible is heated until a vapor forms. The vapor is collimated by the baffles and forms a beam. The deposition rate is monitored by a crystal rate monitor. The sample substrate is then positioned in line with the beam for the appropriate deposition time. From Ref. [38].

patterns [42]. The dynamics of nanocluster deposition are well modeled by the framework of DLA, discussed in the next section.

The crystal properties of Bi dictate a rod-like or a six-fold geometrical figure growth, as shown in Figure 3.9 [41, 43]. Bi was tested in the deposition chamber to ensure that the equipment functioned properly. An increase in film thickness from 0.50 nm to 0.83 nm allowed the growth to transition from rods to six-fold figures.

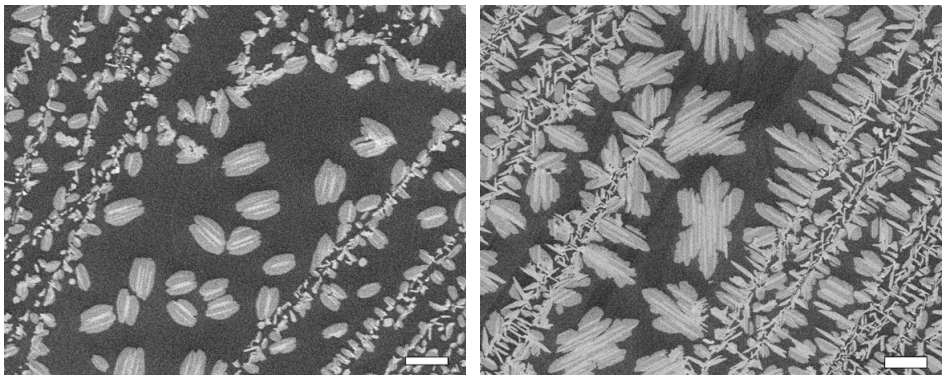

(a) (b)

FIGURE 3.9. Nanoclusters of Bi aggregate into a six-fold symmetry structure. (a) A film thickness of 0.50 nm deposited at a rate of 0.002 nm/s allows the pecan-shaped structures to grow. (b) Depositing 0.83 nm at the same rate provides enough material to allow the symmetry to manifest itself. The scale bars in both pictures are 1 μm.

Sb is known to produce DLA-like structures, but with fat branches. Figure 3.10 shows the results of Sb deposition in this vacuum chamber. Given that the substrate and surface structures are both metal, this design can be used as an electrode with fractal features.

It has been demonstrated that these DLA structures can be grown at chosen locations by preparing the substrate using focused ion beam ablation [44]. In theory, then, an array of seeds could be used to grow these fractal electrodes at pre-determined sites. This would be useful in the design of a fractal electrode taking advantage of both top-down and bottom-up approaches.

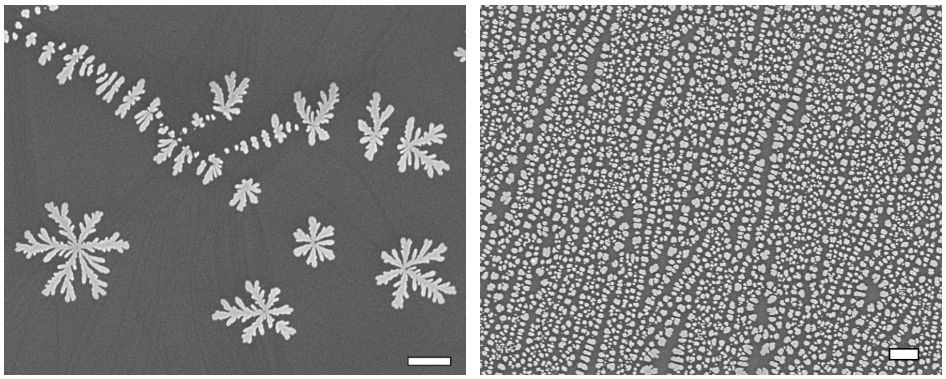

(a) (b)

FIGURE 3.10. Nanoclusters of Sb diffuse on HOPG to create DLA structures. (a) A film thickness of 0.62 nm deposited at a rate of 0.04 nm/s creates isolated DLA islands. (b) A film thickness of 0.31 nm deposited at 0.2 nm/s produces too high of a flux of incoming particles for diffusion to take place. The lined rows indicate the presence of step edges in the graphite substrate as well. The scale bars in both pictures are 1 μm.

3.2.1.1. Diffusion-Limited Aggregation

DLA theory describes the growth and morphology of accreting particles, typically on a two-dimensional surface. One variation of the model allows a particle to randomly walk across a square lattice until encountering a pre-determined seed particle, at which point its location becomes fixed. A new particle is randomly placed on the lattice and allowed to walk until it encounters a fixed particle. Another particle is then added and the process continues until the set number of particles is achieved. This simple generating process produces surprisingly complex structures, as can be seen in the 1.5×10^5 particle aggregate in Fig. 3.11. These structures exhibit self-similarity with a fractal dimension of 1.7.

The diffusing particle, in its random motion, is unlikely to make the necessary steps to navigate to the center of the structure. It comes into contact with, and sticks to, a particle near the outside of the structure, perputating the branching. One variation allows particles to stick to a nearest neighbor or to a next-to-nearest neighbor. Another variation

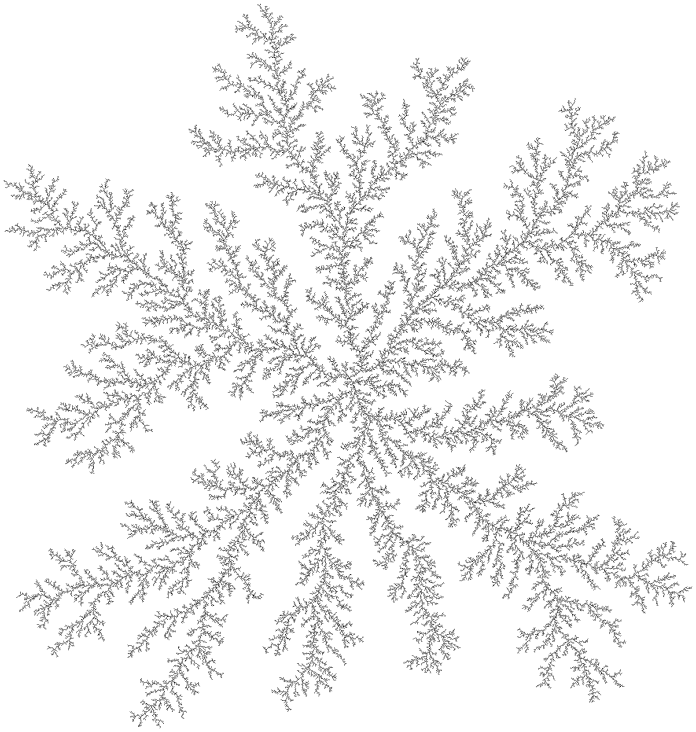

FIGURE 3.11. A DLA structure with 1.5×10^5 particles.

models competitive capture by allowing multiple seed sites. The likelihood of a particle landing at the connecting pixel between two neighboring structures is practically zero. This creates an avoidance phenomenon such that the two structures will continue to grow but stay separate. This competitive capture can be exploited to design electrically isolated structures, such as electrodes. An example is shown in Figure 3.12. This process can be realized experimentally by seeding the substrate with a focused ion beam [44].

The theory of DLA is a powerful tool for explaining many complex processes in nature and will be revisited in the next section.

3.2.2. Sb-PMMA Electrode

The following section details the hindsight of a serendipitous discovery. The previous section presented the results of growing Sb fractals on HOPG, which is a conductor. This

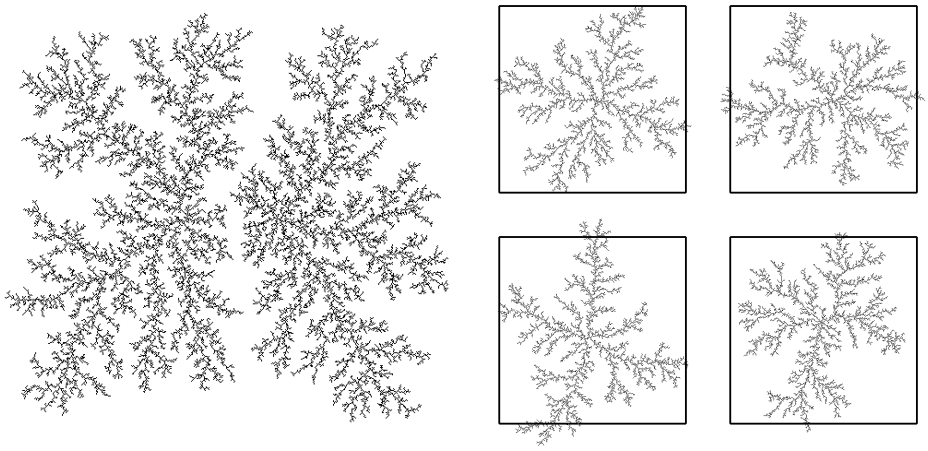

(a) (b)

FIGURE 3.12. DLA structures exhibiting competitive capture. (a) A DLA simulation with two seed particles in close proximity. The avoidance phenenomen keeps islands separate, even as they grow near each other. (b) A DLA simulation with four seed particles set at the center of the boxes. The boxes represent the electrical isolation of the electrodes.

section presents the growth of Sb fractals on an insulating substrate. Based on a result that demonstrates Sb preferentially diffusing from poly(methyl methacrylate) (PMMA) to polystyrene [45], the methodology from the HOPG experiment is applied to depositing Sb on PMMA. One successful result is the early onset of DLA growth of Sb on PMMA, which is presented here. However, a more interesting result is also presented. During the preparatory heating of the PMMA substrate, the high molecular weight polymer begins to depolymerize. The newly freed low molecular weight chains undergo different dynamics depending on the local cooling rate. The most common morphology is dendritic crystals that crystallize from the low molecular weight chains. The deposited Sb then migrates to these dendritic crystals, creating the prototype for a fractal electrode on an insulating substrate. Future work includes tuning the Sb deposition parameters to ensure well-connected electrodes.

3.2.2.1. Polymer Crystallization

PMMA is a polymer often used in industrial applications as an alternative to glass and in lithography as a photoresist. When a polymer is heated above its melting temperature T_{m}, it can crystallize upon cooling. The crystal morphology depends on the rate of cooling and the temperature the sample is allowed to crystallize at, called the crystallization temperature T_c [39]. More directly, there is a strong dependence on the difference of those two temperatures, $\Delta T = T_{\mathrm{m}} - T_c$. The morphology of the surface structures presented herein range from dendritic crystals to DLA islands to square crystals, in order of increasing T_c. This section discusses the results observed in PMMA samples heated and cooled in the vacuum chamber from Figure 3.8.

The formation of surface structures on PMMA takes two dominant morphologies. The largest structures, spanning up to half of a millimeter, are formed by the lower crystallization temperatures. These structures have a long backbone with two smaller generations of branches extending at roughly $90°$. This pattern is similar to that of electrodeposited silver [46]. The second morphology is that of a typical DLA island [42]. These range in size from $100\,\mathrm{nm}$ to $5\,\mu\mathrm{m}$. A third crystal morphology emerges when the crystallization temperature is very near the glass transition temperature, that is, at small ΔT. While many of the dendritic and DLA islands suffer thermal degradation at this high T_c, there is at least one example of a region that developed square crystals. An example of each of these can be seen in Figure 3.13.

The depolymerization of PMMA via thermal degradation happens via both chain-end scission and random chain scission [47]. Chain-end scission is the release of a monomer or oligomer from either end of a polymer chain. Random chain scission is the splitting of a polymer at any point along its chain. 40–$47\,\%$ of a PMMA sample will degrade in the temperature range 220–$270\,°\mathrm{C}$. This batch of PMMA has an average molecular weight of

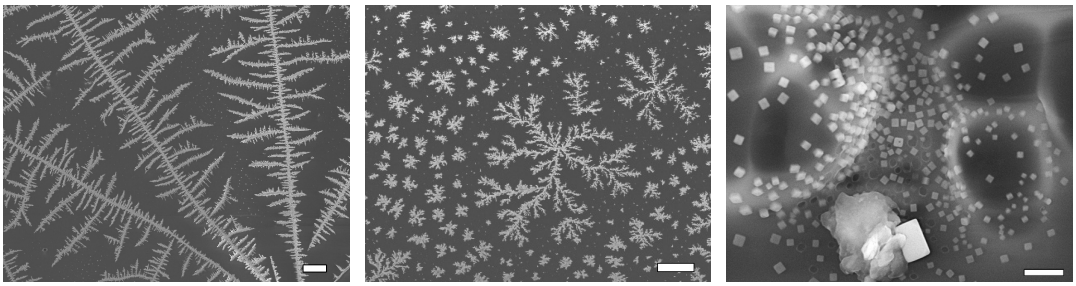

(a) (b) (c)

FIGURE 3.13. Three growth morphologies of surface structures on PMMA. (a) Dendritic crystals grow at large ΔT, when the temperature is near the crystallization temperature T_c. The scale bar is $10\,\mu$m. (b) DLA islands appear at an intermediate ΔT, when extra thermal energy allows the monomers to diffuse at a faster rate. The scale bar is $10\,\mu$m. (c) Square crystals appear at small ΔT, when the sample has been cooled to the crystallization temperature and reheated to the melting tempearture. The lighter colored circles are bubbling of the PMMA. The scale bar is $1\,\mu$m.

$120\,000$ g/mol. The depolymerization then produces a broad range of molecular weights. These newly released products are free to aggregate and crystallize [39, 48].

The ceiling temperature $T_{ceiling}$ of a polymer is the temperature at which there is a dynamic equilibrium between polymerization and depolymerization. There is a wide variety in the reported ceiling temperature for PMMA because $T_{ceiling}$ heavily depends on the physical states of the polymer chains and the monomers. Reported values range from $197\,^{\circ}$C to $400\,^{\circ}$C [49–51].

Heat is delivered to the sample by conduction through the copper sample holder, see Figure 3.6. The deposition hole in the sample holder creates a radial temperature gradient that explains the distribution of morphologies. Being in direct contact with the copper, the PMMA near the edges of the sample receives the most heat. In addition, the rate of heating and cooling will be faster for this region. The dendritic crystals, with the 90° branching, appear nearest the perimeter, where T_c is low. The region towards the center cools slower and this higher heat allows DLA dynamics to dominate the morphology. Reheating the sample after the onset of crystallization produces the square crystal morphology [39].

3.2.2.2. Experimental Methods

The substrates are prepared in a way similar to that for photolithography, but with some modifications. $5\,\text{mm} \times 5\,\text{mm}$ squares are scribed and broken from a SiO_2 wafer. They are cleaned using a spray bottle of acetone and then IPA, followed by a nitrogren blow dry. The average molecular weight of the PMMA used is $120\,000\,\text{g/mol}$. It was purchased in 1997 from Aldrich Chemical Company Inc. (now Sigma Aldrich). The powder is mixed into chlorobenzene at $10\,\%$ by weight in 2009. A drop or two of the photoresist solution is deposited onto the substrate from an eyedropper and spun at 3000 rpm for $60\,\text{s}$ to achieve a nominal thickness of $100\,\mu\text{m}$. The sample is then heated in a convection oven to $250\,^\circ\text{C}$ at a rate of $3\,^\circ\text{C/min}$ and cooled at $2\,^\circ\text{C/min}$ for a total of $3\,\text{h}$ at an elevated temperature. Note that the usual annealing recipe for PMMA is $180\,^\circ\text{C}$ in a convection oven for 60–$90\,\text{s}$ [52], but this recipe is designed to increase the diffusion rate of Sb on PMMA [53].

The sample is placed PMMA-side down in the copper sample holder with a $3\,\text{mm}$ hole drilled below where the sample sits, see Figure 3.6. The sample holder is loaded into the high-vacuum chamber. After the chamber is pumped down to 10^{-8} Torr, the sample is heated to between $200\,^\circ\text{C}$ and $300\,^\circ\text{C}$ by two ultra high vacuum (UHV) button heaters situated below the sample holder. Note that this temperature is well above PMMA's glass transition temperature of $105\,^\circ\text{C}$ [52]. PMMA begins to slowly degrade at a temperature of $220\,^\circ\text{C}$ and up to $47\,\%$ will degrade between 220–$270\,^\circ\text{C}$ [47]. The sample is then removed from the vacuum chamber and data is collected by a range of instrumentation.

3.2.2.3. Scanning Electron Microscope

The pictures in this section were taken using a JEOL-7000F field emission SEM. The polymer surface experiences severe charging effects due to the electron beam. Depositing a metal layer for imaging is avoided because of the small height of the structures.

Figure 3.14 shows an example of the difficulty in imaging a non-conducting surface. The wrong imaging conditions can hide the relevant information. The optimal method for imaging these structures in the SEM is to use a $4\,\text{keV}$ beam to create contrast in the surface, followed by a $20\,\text{keV}$ beam to discharge the surface. The electrons penetrate deep enough that they make it to the Si substrate and are conducted away. Then after changing the beam energy to $1\,\text{keV}$ or $4\,\text{keV}$, a picture is taken with good contrast but without severe charging.

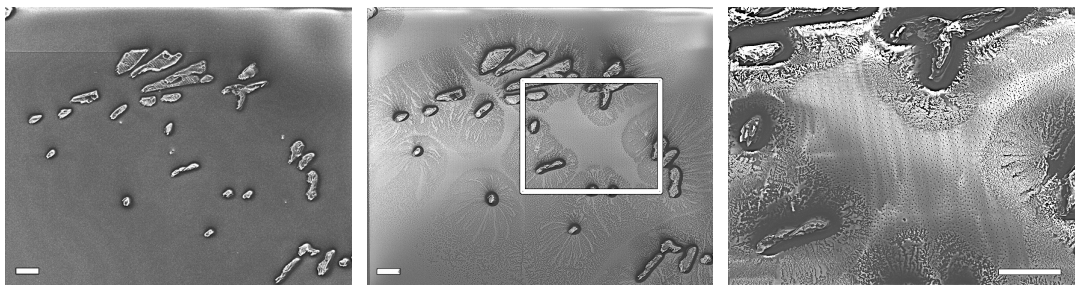

(a) (b) (c)

FIGURE 3.14. Effect of electron beam charging on the PMMA sample. Three SEM images at the same location after different levels of exposure to the electron beam for imaging. (a) The PMMA surface is not a conducting surface. Besides the visible surface defects, there is no obvious structure on the PMMA. (b) After a few seconds of exposure, the electrons charge the PMMA surface, producing contrast for imaging. Large networks of dendritic crystals become visible. The white square provides the location of the magnified image in (c). (c) After too many seconds, the PMMA starts to degrade from heating and charging effects, worsening the image quality. The scale bar in all of these images is $100\,\mu\text{m}$.

One of the properties of a fractal is that small, intricate details exist over very large distances. In order to understand how the crystal morphologies vary across the sample, many individual pictures are taken at a high magnification and stitched together

in Photoshop, see Figure 3.15 (Note that the CAMCOR facility at the University of Oregon now has the ability to do this automatically). This stitched picture covers a width of approximately 2.5 mm and a height of 0.75 mm. The dendritic branches are more prevalent near the edge of the sample and the DLA islands are closer to the center of the sample.

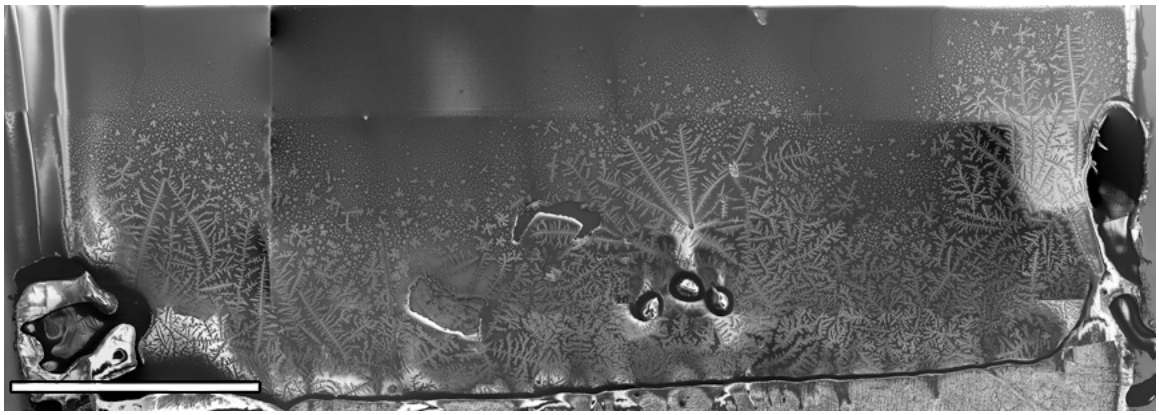

FIGURE 3.15. Forty SEM pictures stitched together provide a high resolution view of a large area of the sample. The transition from dendritic crystals to DLA islands is a function of distance from the edge of the sample (bottom of the picture). The scale bar is 0.5 mm.

3.2.2.4. Energy-dispersive X-ray Spectroscopy

Energy-dispersive X-ray spectroscopy (EDS) is an analysis technique performed in an SEM to determine the atomic constitution of a surface. An electron beam is accelerated to an adequate energy to knock out core shell electrons from atoms in the sample. An electron from a higher energy level falls into the empty lower energy state and a photon equal to the difference in energy is emitted. Different atoms have different spacings between their energy levels. By recording the energy of the emitted photon, the type of atom whence it came can be determined. These studies are performed with an electron beam of 15 keV at a magnification of $400\times$. The probe current is 0.59 nA.

The analysis shown in Figure 3.16 reveals that the spot analyzed comprises $84\,\%$ carbon, $9\,\%$ silicon, and $7\,\%$ oxygen. The high carbon and oxygen content comes from

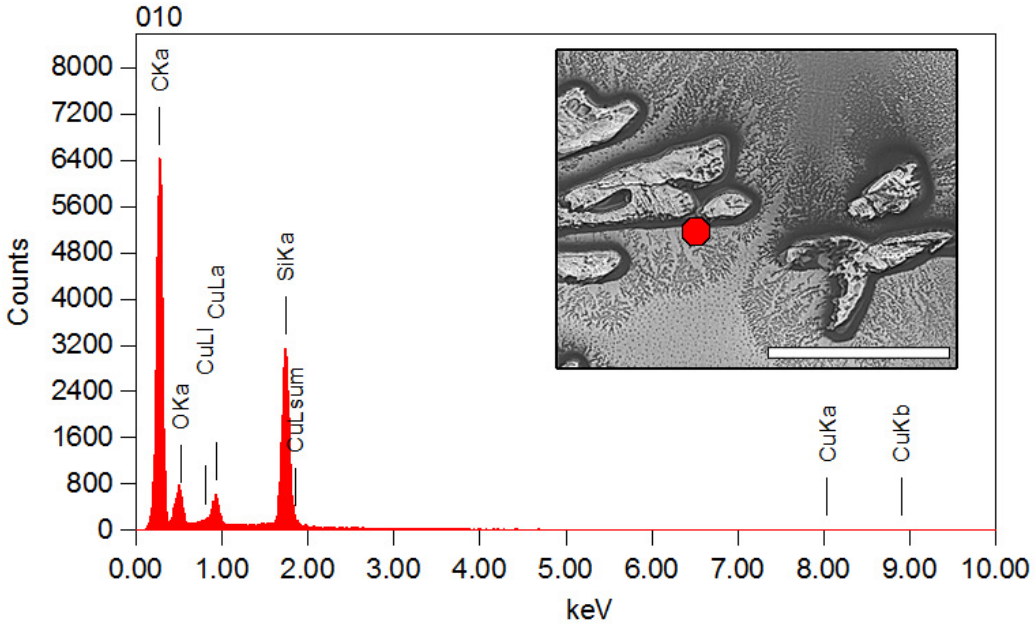

FIGURE 3.16. EDS analysis of dendritic crystals on a PMMA sample. The SEM picture in the inset shows the focus of the electron beam (red dot). The surface at this point consists of 84 % carbon and 9 % silicon with 7 % oxygen. This is consistent with the theory that the fractal structures are made of hydrocarbons. The scale bar in the inset is 200 µm.

the PMMA. While hydrogen is also present in PMMA, it is too light to be measured using EDS. The silicon content comes from the SiO_2 substrate. These results are consistent with the proposed idea that the fractal structures are reorganizations of the PMMA.

3.2.2.5. Time-of-Flight Secondary Ion Mass Spectrometry

Time-of-flight secondary ion mass spectrometry (TOF-SIMS) is a powerful tool to analyze the molecular constitution of a sample. A focused particle beam is rastered across a sample ablating the top 5 nm of the surface. The free molecular ions are accelerated with an electric field away from the sample and through a magnetic field that curves the paths of the molecules. The time it takes for the molecule to reach the detector is dependent on its mass m and charge q, and is given by the forumla, $t = k\sqrt{q/m}$, where the proportionality constant k depends on the particular setup of the measurement apparatus.

Specifically, $k = d/\sqrt{2V}$, where d is the distance from the sample to the detector and V is the accelerating voltage. This technique offers high mass resolution at the expense of image quality and vice versa. A Bi_3+ primary ion source is used to analyze the sample. The imaging mode and spectroscopy mode both use a 25 kV beam. The beam diameter for imaging is focused to 200 nm at a current of 0.1 pA. To take high mass resolution data, the spectroscopy mode uses a 3 µm beam diameter at a current of 0.4 pA. No charge neutralization is used in this analysis.

The results provide more information about the molecular content of the hydrogen and carbon content that was seen in the EDS analysis. The molecules detected are not necessarily the most prevalent on the surface, but rather the ones that are most easily removed by the ion source. There is no presence of any metals save a trace amount of aluminum. A number of different molecules are detected, including C_3H_7, C_4H_7, C_4H_9, C_4H_{11}, C_5H_9, C_6H_{11}, $C_2H_3O_2$, C_4H_5O, C_5H_7O, and PDMS. The highest contrast images are shown in Figure 3.17. The fractals produce a signal with a strong contrast for the hydrocarbons C_4H_9 and C_4H_7. A signal is also detected at a molecular weight of 83 Da (note: the dalton Da is used in mass spectrometry, but is equal in measure to the unified atomic mass unit u), but there appears to be three different molecules that are contributing to the signal. C_6H_{11}, C_5H_7O, and another CHO variant are the most likely candidates. The prevalence of these lightweight hydrocarbons as the most populous materials on the surface is consistent with the hypothesis that heating the high molecular weight PMMA degrades the polymer and produces smaller molecules.

3.2.2.6. NiCr/Au Seeding

The following experiment is performed in an attempt to initiate fractal growth from a patterned edge. Samples are deposited with 5 nm of NiCr (used as an adhesive) followed by

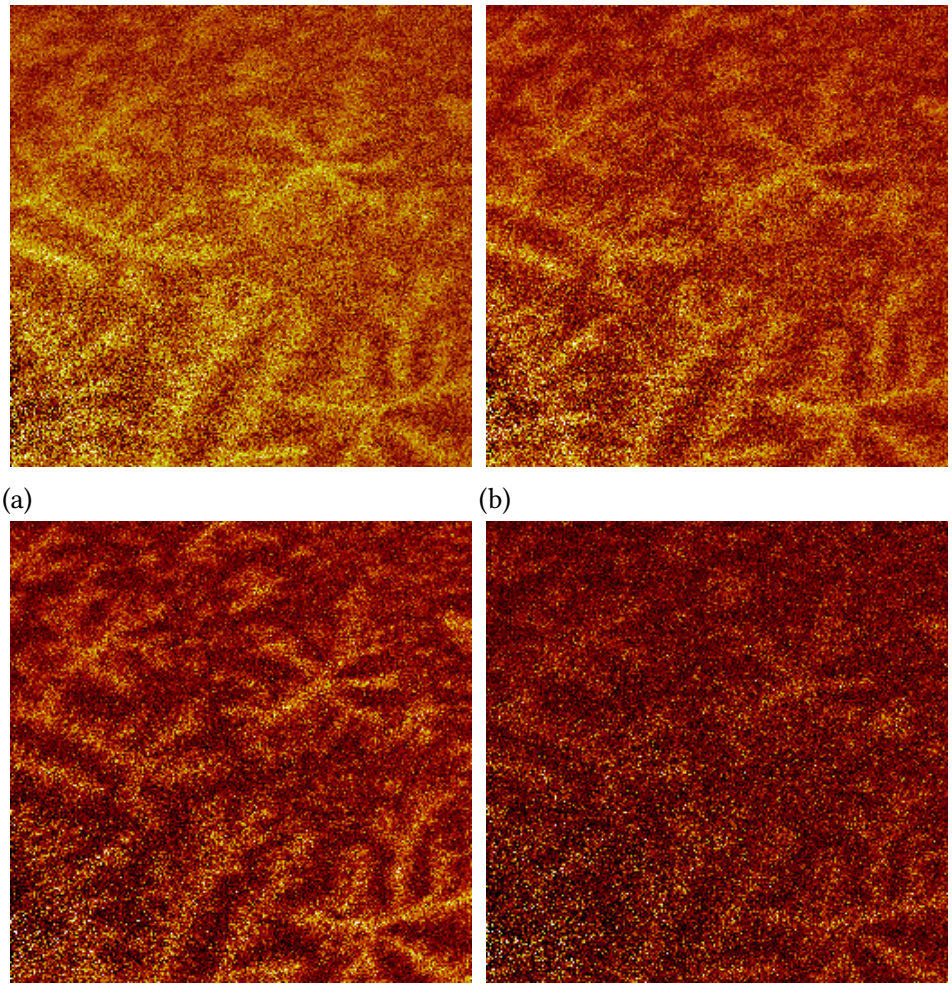

(a) (b)

(c) (d)

FIGURE 3.17. ToF-SIMS high spatial resolution micrographs for the higher contrast molecules. Lighter colors represent higher concentrations of (a) C_3H_7, (b) C_4H_7, (c) C_4H_9, and (d) a signal containing three molecules with an atomic weight near 83 Da. The most significant contribution comes from C_6H_{11} with minor contributions from C_5H_7O and a weak signal, which is most likely another CHO variant. Images taken by Dr. Stephen Golledge.

a 45 nm layer of Au. The deposition is masked using a membraneless TEM grid. Figure 3.18 summarizes the results of the seeding experiment. The polymer crystallization is not seeded by the deposited metal, but rather the crystals form below the metal and show through in relief.

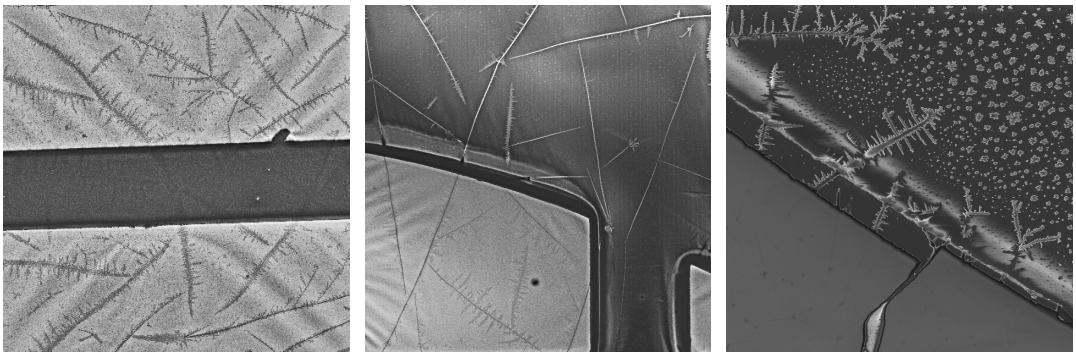

(a) (b) (c)

FIGURE 3.18. NiCr/Au seed pattern does not work as expected. (a) The PMMA forms fractals underneath the Au. (b) The fractal structures in the PMMA show through the gold pads in relief. (c) The gold has started to peel away and the fractal structure can be seen to extend below where the gold was.

3.2.2.7. Sb Deposition and Diffusion

Sb nanoclusters are deposited onto PMMA substrates after crystallization. Sb is chosen to be the deposited material because of the reported high diffusivity on PMMA [45]. The samples are heated to various temperatures after the deposition of Sb, see Figure 3.19. The nanoclusters tend to aggregate to the PMMA fractal structures with and without heating. Excessive heating (199 °C) begins to degrade the dendritic crystals.

3.2.2.8. Atomic Force Microscopy

This section compares the PMMA fractals with and without a deposition of Sb. The height profiles for the PMMA fractal surface features and the deposited Sb were measured

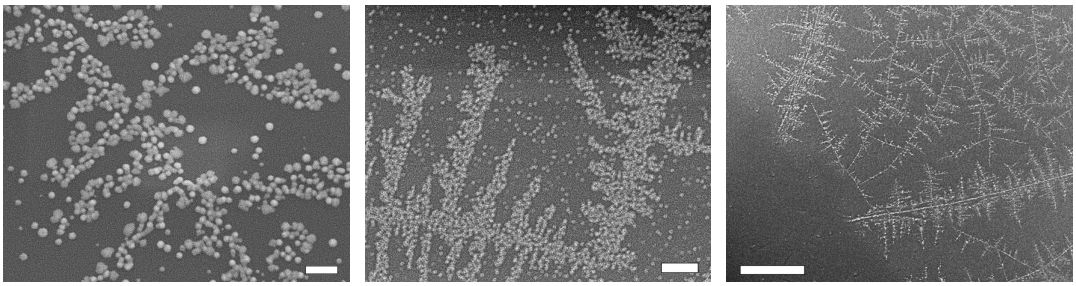

(a) (b) (c)

FIGURE 3.19. Sb was deposited onto four different crysallized PMMA samples. (a) This sample was not heated post-deposition. The scale bar is 200 nm. (b) This sample was heated to 58 °C. The scale bar is 1 µm. (c) This sample was heated to 199 °C. The crystal structure begins to degrade at this temperature. The edge of the Sb deposition can be seen. The scale bar is 50 µm.

using a Digital Instruments Dimension 3100 atomic force microscope (AFM). Pictures of the DLA island morphology are presented in Figure 3.20.

The height profiles of a dendritic crystal pattern are shown in Figure 3.21. The structure's height varies between 9 nm and 32 nm. The rod-like height variations might be due to the particular folding pattern of the polymer crystal.

The Sb nanoclusters diffuse on the surface of the PMMA and aggregate on the fractal structures. The isolated Sb clusters range in height from 15 nm to 21 nm. The clusters that diffuse and aggregate onto the fractal structure reach a height up to 43 nm above the surface of the PMMA.

3.2.2.9. The Onset of DLA

If possible, it would have been an easier task to allow the Sb clusters to diffuse on the PMMA surface and form DLA structures on their own, rather than having to rely on the PMMA fractal patterns to act as seeds. Only one example of the beginnings of DLA islands is found, see Figure 3.23. The cauliflower-like shapes in the Sb nanoclusters are the precursors of DLA structures [42]. A film thickness of 0.62 nm is deposited on the

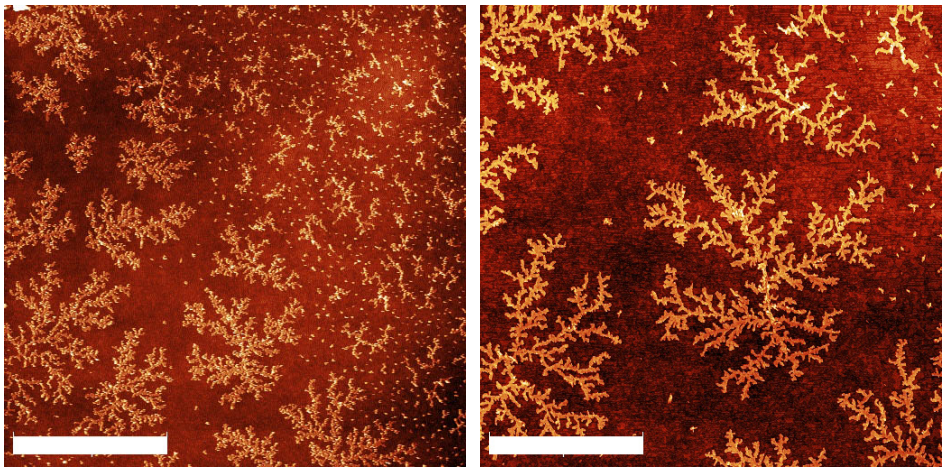

(a) (b)

FIGURE 3.20. AFM images of DLA islands formed from low molecular weight polymer chains. (a) The transition in morphology is most likely due to a temperature gradient in the surface. The polymers on the right cannot overcome the activation energy necessary to diffuse into the DLA structures. The scale bar is $10\,\mu$m. (b) A magnified view of (a) showing the random branching angles indicative of DLA. The scale bar is $5\,\mu$m.

sample and it is not heated post Sb-deposition. This is the first example of nanocluster diffusion to form DLA precursors on PMMA. However, it would be extremely difficult to reproduce even this little amount of growth. The growth dynamics of DLA cannot match the millimeter-size of the dendritic crystals.

3.2.2.10. Fractal Analysis of Surface Structures

The fractal surface features are analyzed using the box counting technique described in Chapter II. The fractal dimension of the structures formed is a function of the crystallization temperature T_c [39]. The fractals measured from these samples range from $D_f = 1.5$ to 1.7.

For a structure to be analyzed with the box counting technique, the SEM photograph must be converted to a binary bitmap. The outline of the binary bitmap is traced by hand using a Wacom Intuos5 tablet. A box counting analysis is performed on the images and the

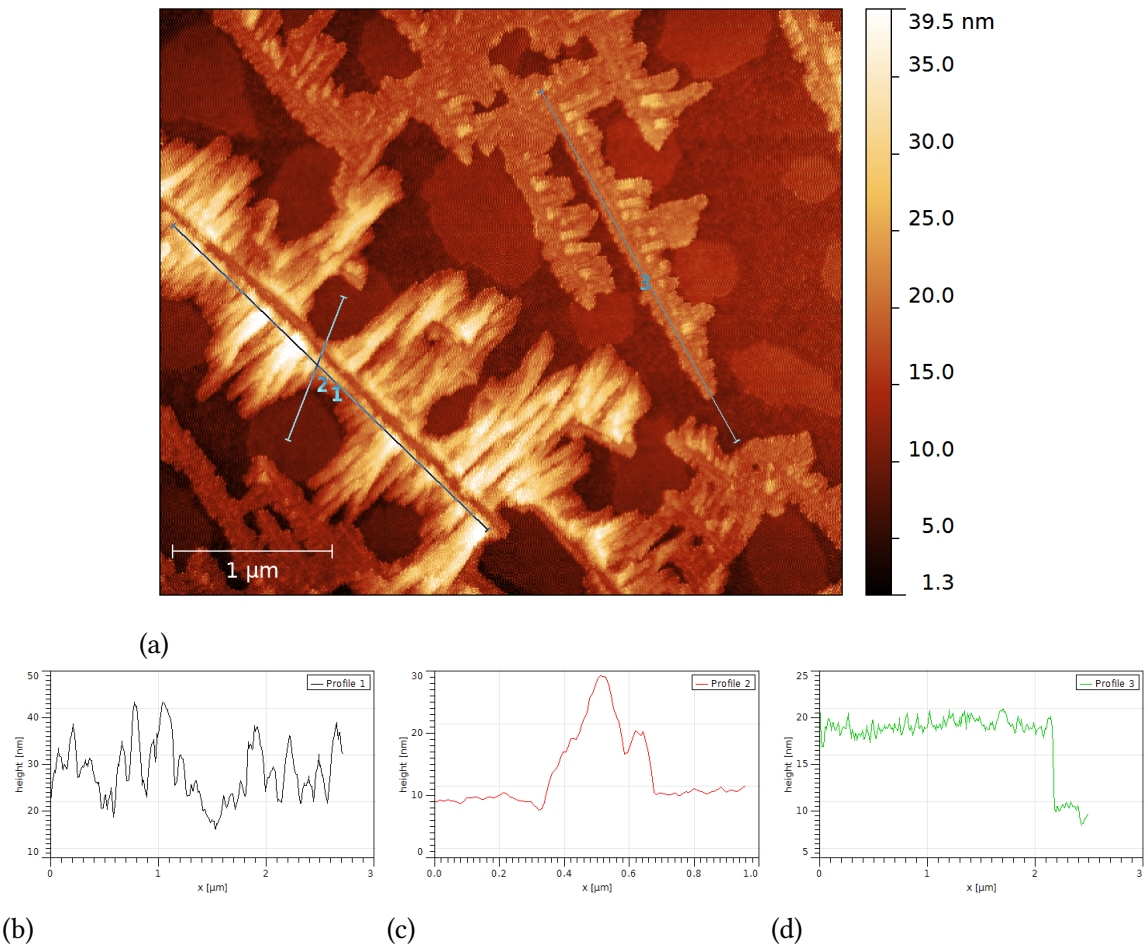

FIGURE 3.21. (a) The AFM height profiles of various features of a dendritic crystal in PMMA. The structures range between 9 nm and 32 nm. (b) Height profile along the tall backbone showing fluctuations on the order of 20 nm. (c) Cross section of the tall backbone showing a maximum height of 20 nm above the surface of the PMMA. (d) The shorter branch has an average height of 7 nm.

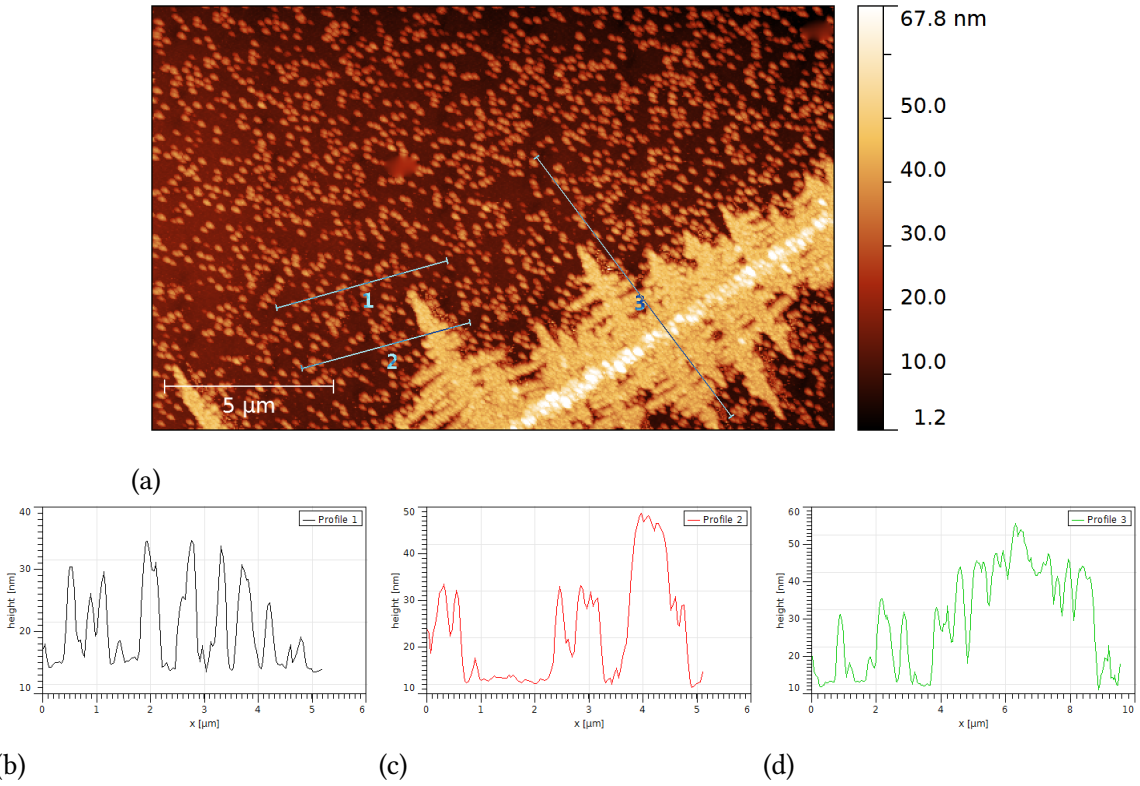

FIGURE 3.22. (a) The AFM height profiles of Sb clusters deposited onto a PMMA sample with dendritic crystals. The tallest structure is 43 nm above the surface of the PMMA. (b) The Sb clusters range in height between 10–20 nm. This variation is likely due to measuring off center of some of the Sb clusters. (c) The Sb clusters are 19 nm tall. With the assumption that this branch is equivalent to the shorter of the branches in Figure 3.21(a), then the Sb clusters have nearly doubled their height by coalescing to 37 nm on the fractal branch. (d) If the backbone here is 20 nm tall, the Sb clusters are their typical height of 21 nm along the peak.

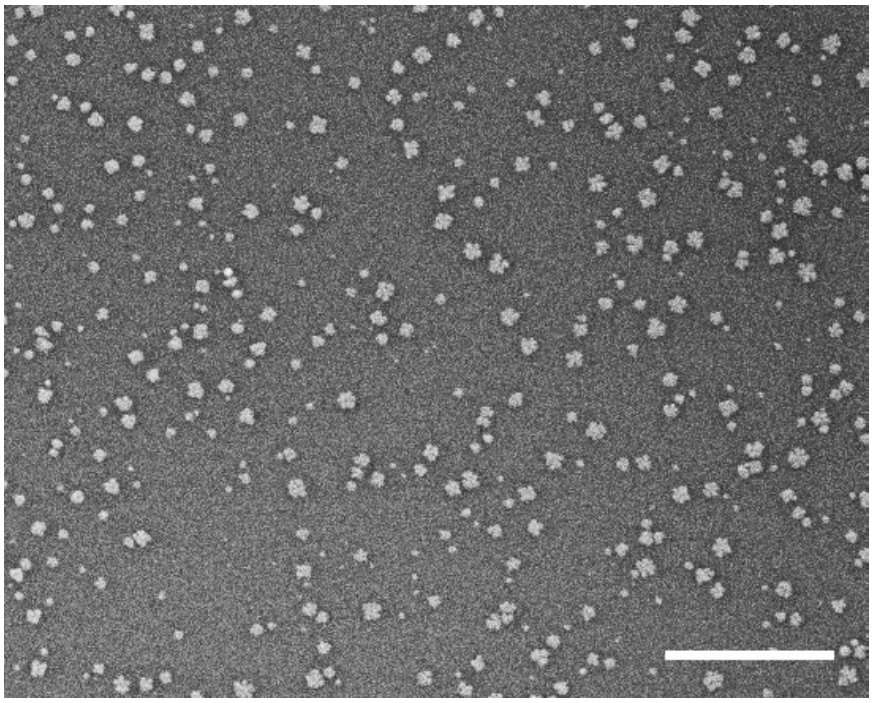

FIGURE 3.23. The onset of DLA of Sb clusters on PMMA. The cauliflower shape is a precursor to DLA growth

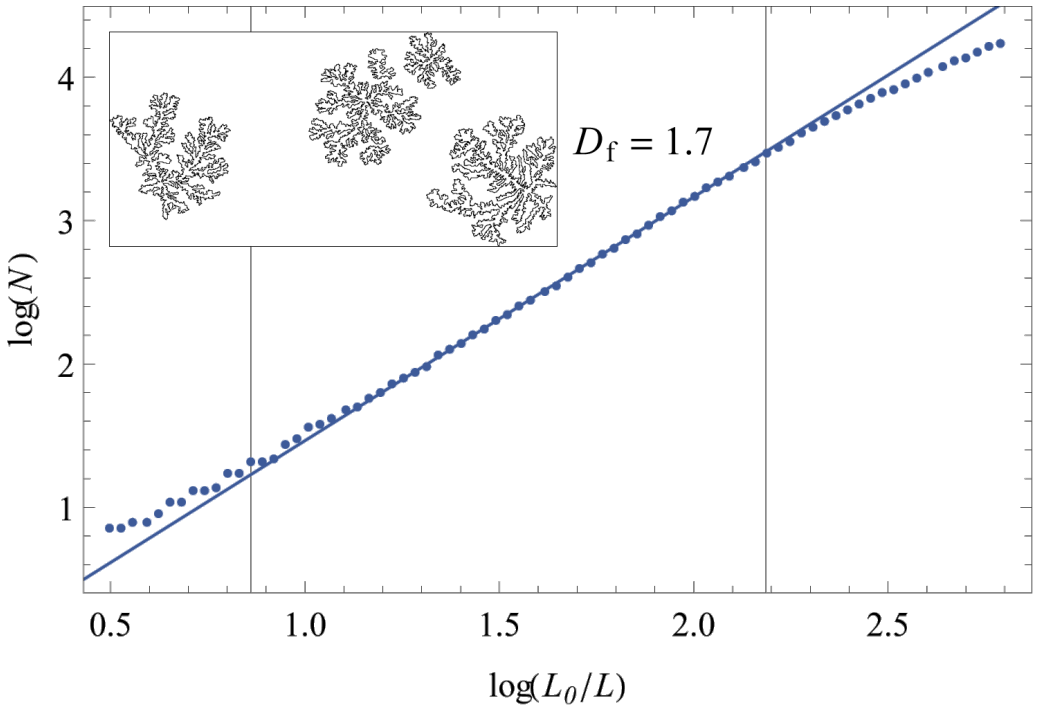

FIGURE 3.24. Fractal analysis of the DLA islands. The fractal dimension is the slope of the line $D_f = 1.7$.

results are shown in Figures 3.24 and 3.25. The PMMA DLA island has a fractal dimension $D_{\mathrm{f}} = 1.7$, which matches that found in the literature [20]. The PMMA dendritic branches have a slightly smaller value of $D_{\mathrm{f}} = 1.6$.

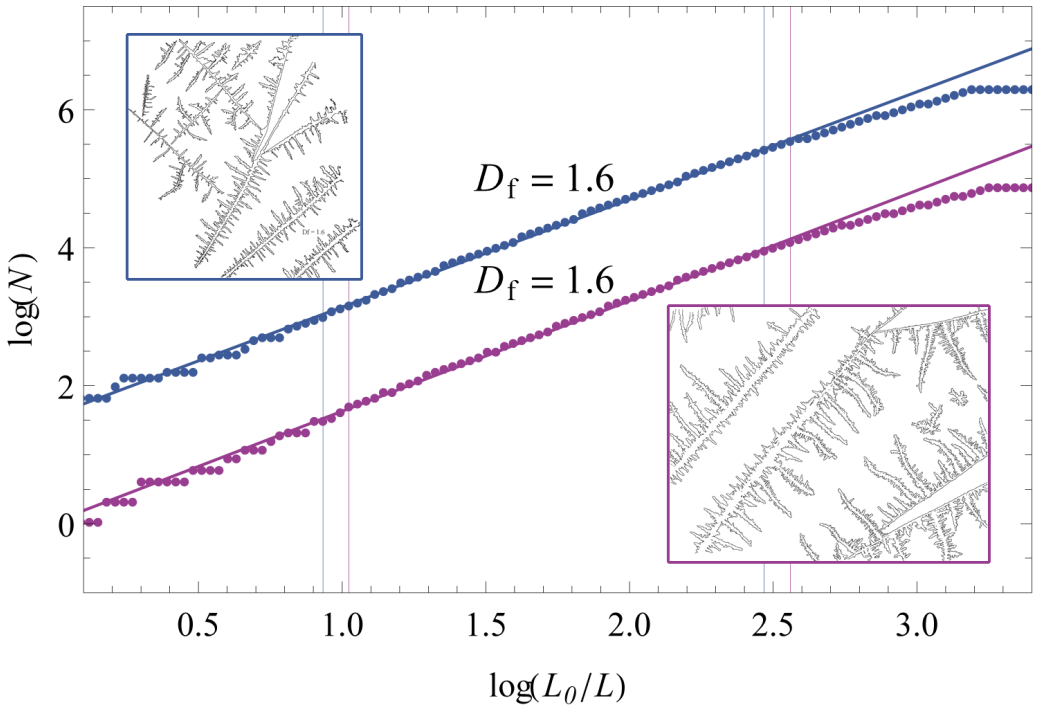

FIGURE 3.25. Fractal analysis of the dendritic crystals on one sample without Sb deposition (top-left) and another sample with Sb deposition (bottom-right). The fractal dimension of both dendritic crystals is $D_{\mathrm{f}} = 1.6$. The presence of the Sb nanoclusters does not affect the fractal dimension. The data are vertically offset for clarity.

The fractal analysis of a dendritic crystal at two different magnifications is combined to show that the object exhibits fractality for 2.5 orders of magnitude. The zoom sequence for the data analyzed is shown in Figure 3.26. The outlines are traced in white and shown again as insets in the scaling plot, see Figure 3.27. The slope of the data transitions away from a fractal dimension of $D_{\mathrm{f}} = 1.6$ at a fine length scale of 90 nm. This length is the diameter of the Sb nanoclusters. That is to say that the deposition of the Sb nanoclusters does not reduce the fractality except at the length scale that the individual clusters can be resolved.

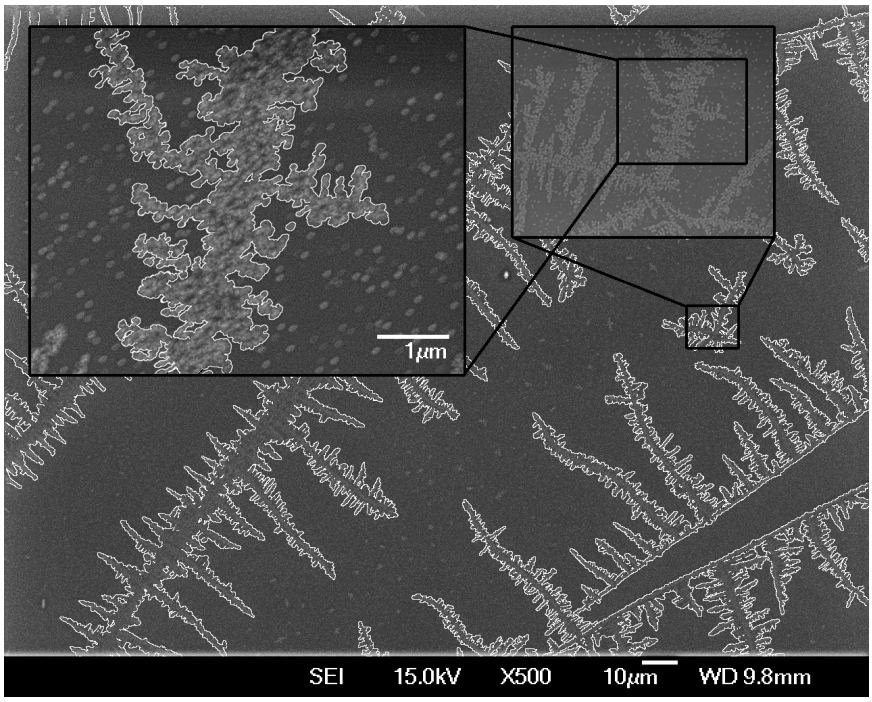

FIGURE 3.26. Zoom sequence for fractal structure coated with Sb.

There is a range of fractal dimensions associated with both types of structures. This is attributed to the temperature gradient of the sample. The variation is consistent with that reported in the literature [39]. It is shown that the dendritic crystals exhibit fractality for 2.5 orders of magnitude. It is uncommon to find spatial fractals that span this range in physical systems.

3.3. Summary

This chapter discussed the fabrication of four different fractal electrode designs. Both top-down and bottom-up approaches were used to make exactly self-similar and statistically self-similar electrode geometries. Lithography techniques were exploited to create exact fractals as isolated metal structures and as bas-relief electrodes. A graphite electrode was texturalized with Sb fractals using the principles of DLA. Finally,

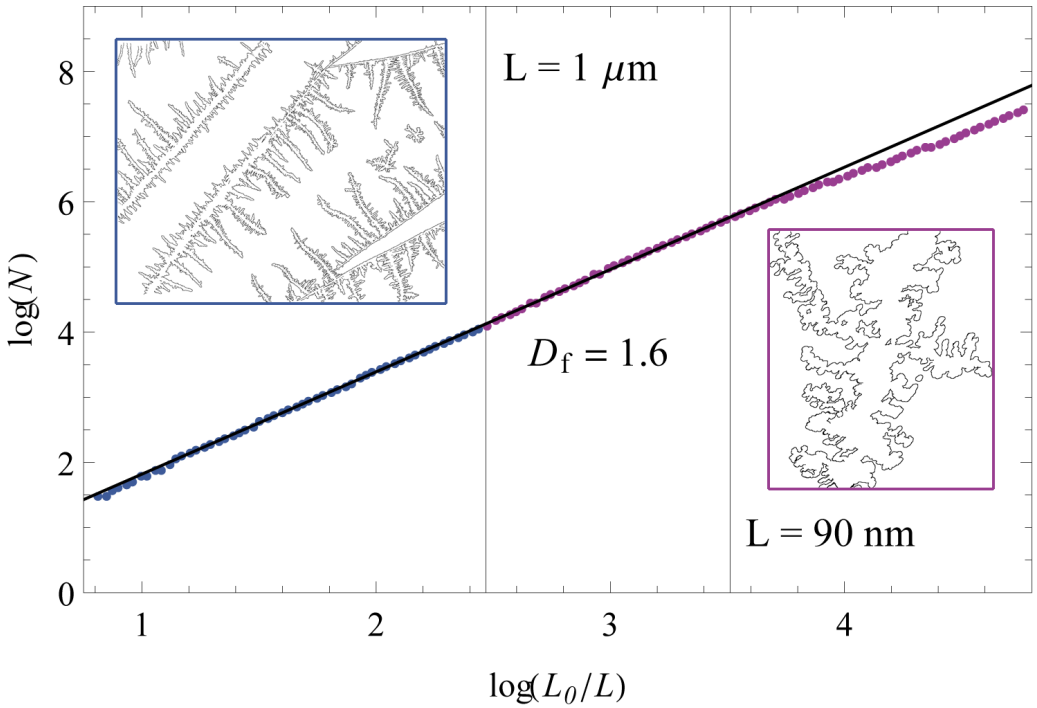

FIGURE 3.27. The scaling plot of the Sb-coated PMMA analyzed at different magnifications. The blue and purple points relate to the images on the left and right, respectively. Their relation to each other can be seen in Figure 3.26. The structure shows fractal behavior over an impressive 2.5 orders of magnitude with a fractal dimension of $D_f = 1.6$. The structure ceases its fractal behavior at the resolution of the Sb nanoclusters, $L = 90$ nm. The data have been vertically offset to show that the gradient fits both sets of data.

a crystallization technique for PMMA was demonstrated as well as its subsequent coating in Sb as an approach for making self-assembled millimeter-sized fractal electrodes.

The HafSOx design was used to make several fractal shapes. Among these shapes were Sierpinski carpets, Sierpinski pillars, H trees, angled H trees, an array of pillars, a fractal arrangement of pillars, and a square platform as a control structure. However, none were brought to the completed level of metal deposition. Overall, the HafSOx fabrication is excellent at achieving very narrow linewidths but is limited to short heights of less than $20\,\mathrm{nm}$. Taller structures may be possible if reactive ion etching is used rather than wet etching.

The SU-8 designs were limited to just the H tree at two different fractal dimensions, $D_\mathrm{f} = 1.5$ and 2.0, an array of the smallest iteration of Hs, and a square platform control. The height of the SU-8 design was $2\,\mu\mathrm{m}$. This is the method that the Taylor lab is most likely to carry forward in its experiments.

The Sb-HOPG design is a proof of principle for texturalizing a flat electrode surface with DLA fractals. AFM characterization was not carried out on these samples, but the heights are most likely between 10–$30\,\mathrm{nm}$, based on the literature for Sb deposition [42].

The Sb-PMMA electrode was a successful design in fabricating a fractal branching metal on an insulating substrate. The different morphologies are a function of temperature and can be tuned. Furthermore, it was shown that the object is fractal for over 2.5 orders of magnitude. Ensuring the Sb coverage is optimized is the last step to finalizing this electrode design.

CHAPTER IV

FRACTAL ELECTRODES FOR A RETINAL IMPLANT

The research presented in this chapter was a collaborative effort. Bill Watterson assisted with the photodiode simulations. The neural adhesion experiments were performed by Bill Watterson and Associate Professor Maria Thereza Perez at Lund University in Sweden. I was the primary contributor to the remainder of the work presented.

In this chapter, the fractal electrode's role in a retinal implant is explored. There are three different capacities that the fractal electrode might play in a retinal implant. In Section 4.1, the top contact of a photodiode is replaced with a fractal design and the resulting dynamics are explored using a circuit model called modified nodal analysis. Section 4.2 tasks the fractal electrode with stimulating neurons. Electric field simulations are carried out for various electrode designs using the finite element method. Finally, in Section 4.3, the physical adhesion of neurons on fractal electrodes is studied. The retinal neurons of mice are cultured on substrate samples with various electrode designs. The further developments and future directions of these projects will be discussed in the concluding chapter.

4.1. Photodiode Dynamics

A subretinal implant is an electronic device containing an array of photodiodes, each with an electrode for neural stimulation, that is inserted into the eye to replace the natural photoreceptors. The light levels inside the eyeball are relatively low, so whatever illumination current is generated in each photodiode should not be squandered. The photodiode is operated in short circuit mode to minimize the diode current. The eyeball

should not be exposed to excessive heat, so it is also important to minimize the Joule heating.

4.1.1. Photodiode Mode of Operation

A photodiode is an electronic device capable of converting absorbed light into an electric currrent. Traditionally, it is made of two differently doped semiconductor materials sandwiched between two metal contacts to extract the current. The semiconductor is regionally doped with electron acceptors (p-type) and donors (n-type). The boundary of these regions is called the PN junction. When a photon is absorbed, an electron-hole pair is created. If the minority carrier happens to diffuse to the PN junction, the intrinsic electric field drives it across the junction. This separation of charges produces the illumination current. A high resistance in the photodiode contacts will cause charge to build up. This charge produces its own electric field that drives a current opposing the illumination current. This opposition current is called the diode current. The sum of the currents is called the photocurrent. The circuit diagram for a photodiode is shown in Figure 4.1.

The bottom of the photodiode (Figure 4.2) is completely covered by a metal to efficiently extract the photocurrent. However, the top contact must not completely cover the top because light must pass into the photoactive material. The efficiency of a photodiode relies on absorbing as much light as possible and extracting as much current as possible. It is the purpose of this section to examine whether the high perimeter-to-surface-area ratio of a fractal top contact can be beneficial in this regard.

The electrical behavior of two hypothetical photodiodes is shown in an I-V curve in Figure 4.2. There are three parameters that explain the shape of the curve. The short circuit current (y-intercept) and the open circuit voltage (x-intercept) are the maximum

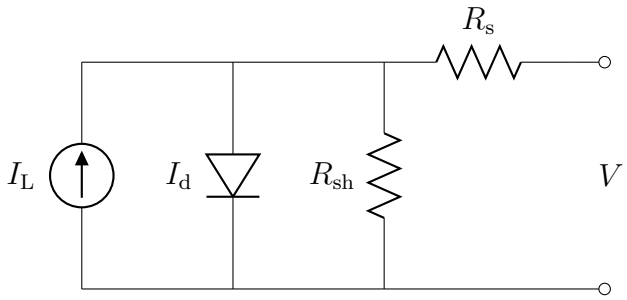

FIGURE 4.1. Photodiode circuit model. A photodiode can be modeled electrically as a series resistance and a current source in parallel with a diode and a shunt resistor. The current source acts as the illumination current caused by photon absorption. The diode models the internal electric field generated by the increased concentration of majority carriers. In an ideal photodiode, the shunt resistance would be infinite, preventing any internal voltage drops due to defects. The series resistance accounts for the resistance of the semiconductor, metal, and metal-semiconductor junction resistances.

current and voltage possible. A third variable called the fill factor is a measure of the curvature. Our simulation will model a photodiode in short circuit mode (also shown in Figure 4.2), in order to maximize the current available. The lower coverage of the fractal top contact will allow more light into the device producing a higher short circuit current.

The simulation of the top electrode's electrical properties relies on a technique called modified nodal analysis (MNA). It is an algorithmic approach to solving Kirchoff's laws for large symbolic circuits. The mechanics of the simulation will be explained using a simple circuit and then applied to the photodiode case. The simulation focuses on just the effect of the geometry of the top contact as the rest of the photodiode is identical.

4.1.2. Modified Nodal Analysis

Modified nodal analysis is a method for solving an electrostatics or electrodynamics problem by viewing a physical system as a network of circuit elements [54]. The system can be divided into a discrete space where every two nodes are connected by a simple circuit element. The example in Figure 4.3 shows five nodes, all connected by resistors of

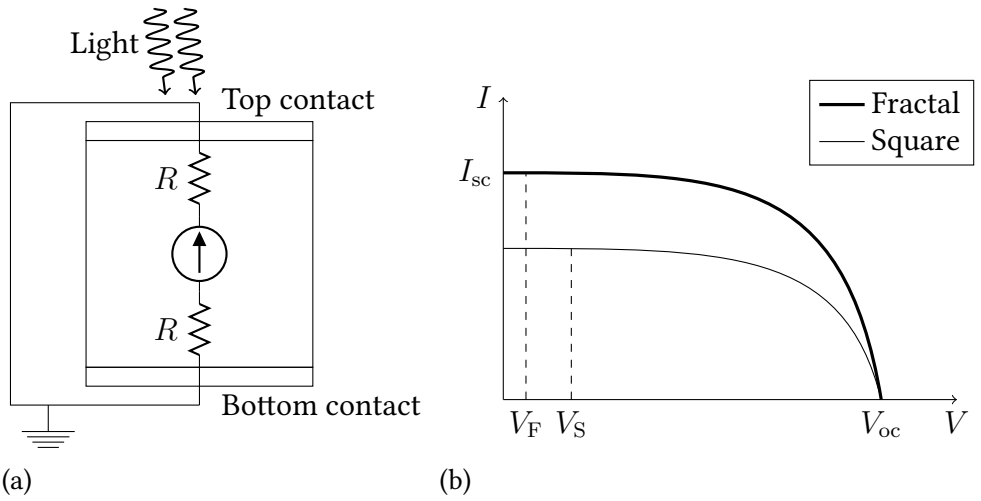

FIGURE 4.2. (a) Schematic of a photodiode operating in short circuit mode. Upon absorbing light, the PN junction acts a current source with series resistance. (b) Schematic of an IV curve for two photodiodes with different top contacts. The short circuit current I_{sc} is dependent on the amount of light absorbed by the photodiode. The open circuit voltage V_{oc} is the maximum voltage difference across the photodiode when there is no load. Because of the fractal top contact's smaller coverage, it absorbs more light and has a higher short circuit current. The smaller resistance of the fractal design creates a smaller voltage drop in the circuit.

varying resistances R_i. A voltage is applied to node b and node f is set to ground. The voltage at each node and the current in the circuit can be solved by applying Kirchoff's laws. In this way, bitmap representations of large electrical networks can be solved using optimized algorithms.

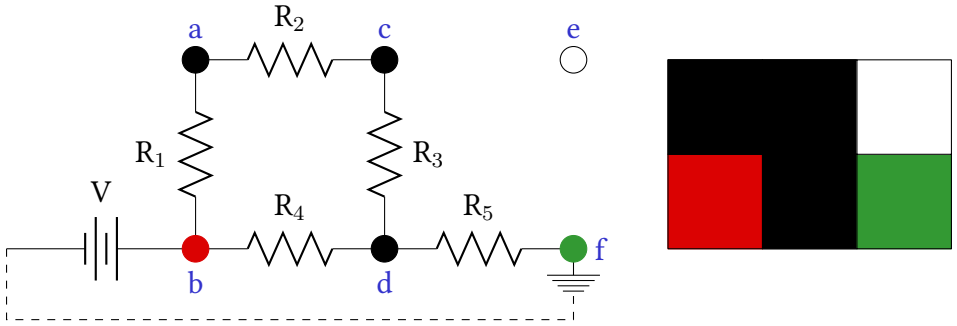

FIGURE 4.3. An example of a circuit in its standard circuit element form and in bitmap representation form. This equivalence allows us to simulate large resistor networks based on an image of their geometry.

The problem is ultimately solved by finding a solution for the matrix equation

$$\mathbf{A}\mathbf{x} = \mathbf{b}. \tag{4.1}$$

The elements of the matrix are allocated according to the following set of rules. $\mathbf{A}$ is an $(m+n) \times (m+n)$ matrix, where m is the number of independent voltage sources and n is the number of nodes. For this example, $m = 1$ and $n = 6$. The matrix $\mathbf{A}$ contains information about which nodes are neighbors and their internodal conductances. The vector $\mathbf{b}$ has $(m+n)$ elements, with the first n holding the value of a current source at node n and the last m holding the values of the voltage sources. The vector $\mathbf{x}$ also has $(m+n)$ elements, which upon solving will produce the voltage at each node n and the current associated with each voltage source m.

Each type of circuit element affects the matrix equation in a different way. For example, at node i, the conductance of each connected node $j, k, \ldots$ is added at $\mathbf{A}_{ii}$ and

subtracted at $\mathbf{A}_{ij,ji}$, $\mathbf{A}_{ik,ki}$, etc. This is summarized in the following matrix equation called a resistor stamp

$$\begin{array}{c|cc|} & A_i & A_j \\ \hline i & \frac{1}{R_{ij}} & -\frac{1}{R_{ij}} \\ j & -\frac{1}{R_{ij}} & \frac{1}{R_{ij}} \\ \end{array} .$$

The stamps for different circuit elements are available [55]. After applying these rules to the circuit in Figure 4.3, the resulting matrix equation is

$$\begin{bmatrix} \frac{1}{R_1}+\frac{1}{R_2} & -\frac{1}{R_1} & -\frac{1}{R_2} & 0 & 0 & 0 & 0 \\ -\frac{1}{R_1} & \frac{1}{R_1}+\frac{1}{R_4} & 0 & -\frac{1}{R_4} & 0 & 0 & 1 \\ -\frac{1}{R_2} & 0 & \frac{1}{R_2}+\frac{1}{R_3} & -\frac{1}{R_3} & 0 & 0 & 0 \\ 0 & -\frac{1}{R_4} & -\frac{1}{R_3} & \frac{1}{R_3}+\frac{1}{R_4}+\frac{1}{R_5} & 0 & 0 & 0 \\ 0 & 0 & 0 & 0 & 0 & 0 & 0 \\ 0 & 0 & 0 & 0 & 0 & 0 & -1 \\ 0 & 1 & 0 & 0 & 0 & -1 & 0 \end{bmatrix} \begin{bmatrix} V_a \\ V_b = V \\ V_c \\ V_d \\ V_e = 0 \\ V_f = 0 \\ I \end{bmatrix} = \begin{bmatrix} 0 \\ 0 \\ 0 \\ 0 \\ 0 \\ 0 \\ V \end{bmatrix} . \tag{4.2}$$

The solution to this equation is $\mathbf{x} = \mathbf{A}^{-1}\mathbf{b}$. Because of the possible magnitude of the equation (up to 5×10^6 elements), we use the Eigen [56] and SuperLU [57] libraries to invert $\mathbf{A}$ and solve for $\mathbf{x}$.

4.1.3. Comparing Top Contact Geometries

The different types of connections in the resistance network of a photodiode are shown in Figure 4.4. There are three different resistance values to consider. The resistance between two metal nodes is R_{mm}, two semiconductor nodes is R_{ss}, and the resistance between a metal-semiconductor interface is R_{ms}. Each uncovered semiconductor also

acts as a current source. One metal node in the center of the geometry is also grounded to put the photodiode in short circuit mode.

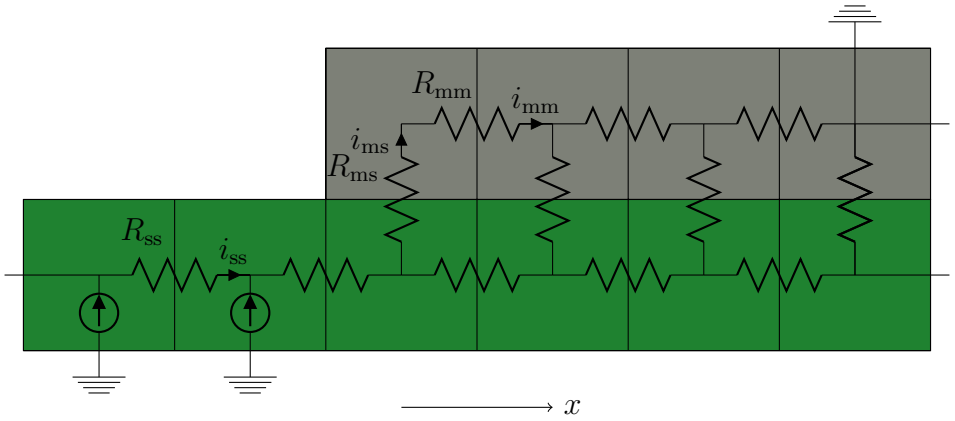

FIGURE 4.4. Internodal resistances between the semiconductor and metal nodes in a photodiode model. There are three different types of connections. Metal-metal connections run along the top nodes and are modeled by a resistance R_{mm}, semiconductor-semiconductor connections run along the bottom nodes and are given by R_{ss}, and the metal-semiconductor junctions connect the two layers vertically. Their resistance is R_{ms}. Semiconductor nodes below the metal contact are modeled without current sources.

The two top contact geometries are shown in Figure 4.5. The geometries are a central square contact and an H tree top contact. The square contact has the same geometry as the Artificial Silicon Retina device developed by the company Optobionics [11]. The photodiode is a $20\,\mu\mathrm{m}$ square of Si with a gold (Au) top contact. The square electrode is $9\,\mu\mathrm{m}$ on each side. The width of the H tree fingers is $80\,\mathrm{nm}$ at its narrowest and $520\,\mathrm{nm}$ at its widest. Our starting hypothesis is that the H tree geometry will outperform the square geometry by allowing the carriers to leave the more resistive semiconductor layer sooner.

The nodal analysis is performed at a resolution of $20\,\mathrm{nm/pixel}$ such that there are two layers of 10^6 pixel each. The semiconductor thickness is taken to be $1\,\mu\mathrm{m}$. The height of the metal contact is $250\,\mathrm{nm}$. The values for the variables of each node are given in Table 4.1. The resistivity of Au is $2.4 \times 10^{-8}\,\Omega\,\mathrm{m}$ [58]. The Si resistivity assumes a phosphorus

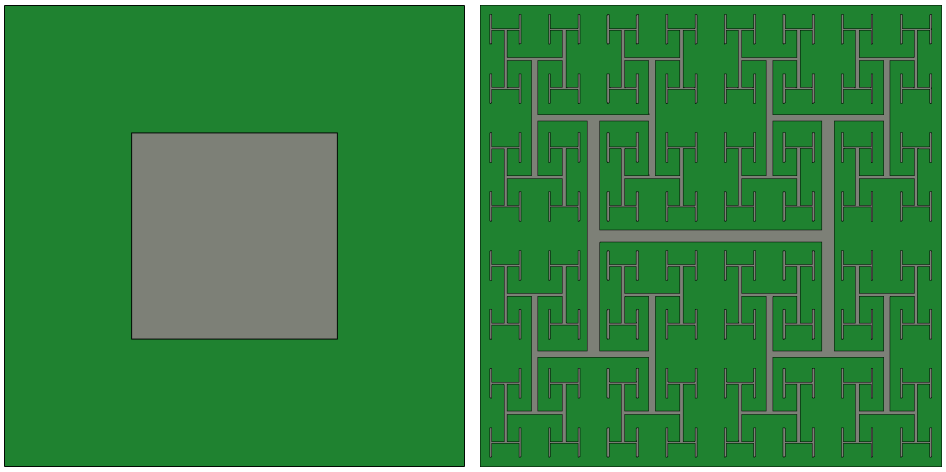

(a) (b)

FIGURE 4.5. Two different photodiode top contact geometries are modeled using MNA. (a) A $9\,\mu$m square electrode sits atop a $20\,\mu$m square photodiode. (b) A four iteration H tree acts as the top contact on a $20\,\mu$m square photodiode.

doping level of $10^{19}\,/\text{cm}^3$, which provides an approximate resistivity of $5.5 \times 10^{-5}\,\Omega\,\text{m}$ [59]. The contact resistance is taken to be $10^{-10}\,\Omega\text{m}^2$ as within the typical range for metal-semiconductor contacts [60].

Variable	Value	Description
R_{mm}	$0.1\,\Omega$	$R = \rho \times L/A = 2.4 \times 10^{-8}\,\Omega\,\text{m} \times 20\,\text{nm}/(20\,\text{nm} \times 250\,\text{nm})$
R_{ss}	$55\,\Omega$	$R = \rho \times L/A = 5.5 \times 10^{-7}\,\Omega\,\text{m} \times 20\,\text{nm}/(20\,\text{nm} \times 1\,\mu\text{m})$
R_{ms}	$2.5 \times 10^5\,\Omega$	$R = \rho_{\text{c}}/A = 10^{-10}\,\Omega\text{m}^2/(20\,\text{nm} \times 20\,\text{nm})$
I	$1.2 \times 10^{-13}\,\text{A}$	$I = J \times A = 300\,\text{A/m}^2 \times 20\,\text{nm}^2$
V_{appl}	$0\,\text{V}$	The metal contacts are shorted.

TABLE 4.1. The resistance, current, and applied voltage values for each node in the simulation.

The simulation outputs the voltage at each node and the amount of current flowing through each node. The voltages of each node are presented as temperature maps in Figure 4.6, with the color scales ranging 0 (blue) to 0.8 (red) μV for the square contact and 0 (blue) to 0.3 (red) μV for the H tree. These voltages in the μV range are much smaller than the open circuit voltage of Si at $730\,\text{mV}$ [59]. This is consistent with the assumption

that the photodiode is operating in short circuit mode (Figure 4.2). Large gradients in voltage represent highly resistive paths. The higher voltage in the square case is due to the charge buildup in the corners of the photodiode, as they have the furthest distance to travel before reaching the lower resistivity of a metal contact.

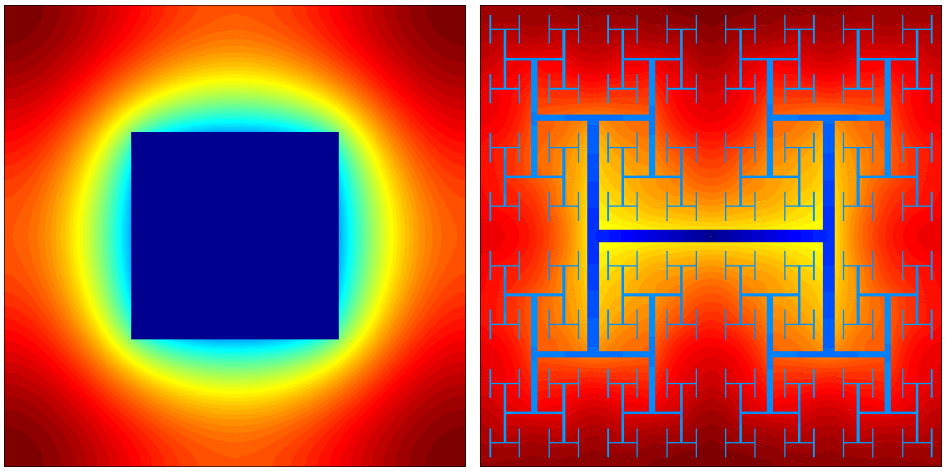

(a) (b)

FIGURE 4.6. The voltage maps for the two photodiodes with different top contact geometries. Blue to red scales the voltage $0–0.8\,\mu V$ and $0–0.3\,\mu V$, respectively for the (a) square and (b) H tree. The higher voltage for the square top contact is due to charge buildup in the corners. The distance to the metal contact is greater for this geometry.

Joule heating is used as a performance indicator for the two geometries. The square of the voltage difference between two nodes is divided by that nodal resistance. The power loss is summed for every nodal connection. The results for the two top contact geometries are shown in Figure 4.7.

The H tree geometry reduces the power loss by half. The H tree loses more power in the metal-metal connections because of the thin branches of the metal contact. It also suffers in the metal-semiconductor junction due to the current crowding phenomenon, which will be explored next. However, the H tree is successful at reducing the semiconductor-semiconductor losses by shortening the distance that carriers must travel in the highly resistive semiconductor material. The H tree's losses are also relatively

higher due to the higher incoming power. The H tree geometry lets 6% more light pass into the photodiode. The higher incoming power causes more Joule heating.

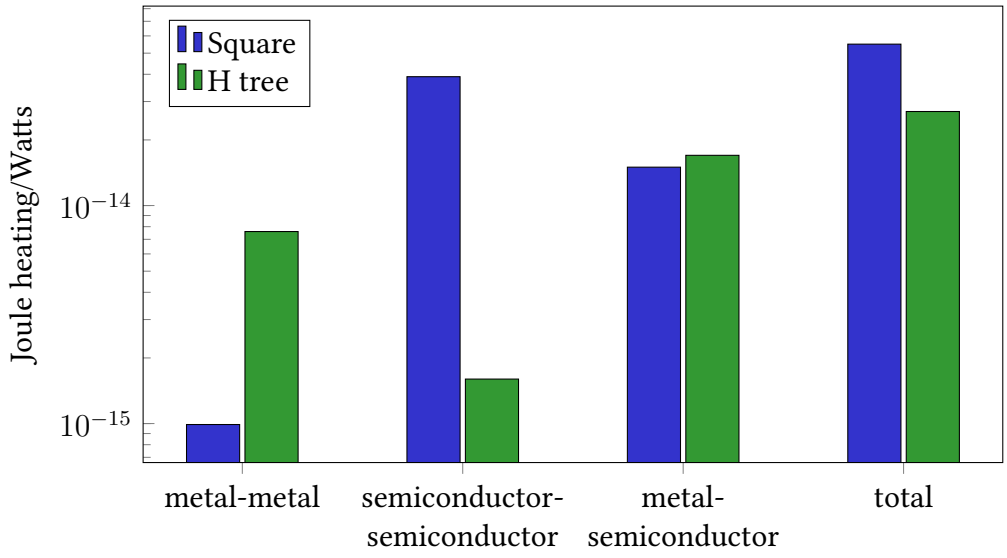

FIGURE 4.7. Power lost to Joule heating for each type of nodal connection and the total power loss for each geometry. The H tree loses more power in the metal-metal and metal-semiconductor connections due to the thin branches of the H tree and current crowding, respectively. The H tree outperforms the square geometry by reducing the distance that carriers travel in the highly resistive semiconductor, thereby reducing the Joule heating in the semiconductor. There is also a small relative increase in the H tree's losses due to its smaller coverage. The H tree geometry allows 6% more light to pass into the photodiode, increasing the Joule heating.

A closer look at the metal-semiconductor connection provides another insight to designing an effective top contact. Current crowding is the name given to the nonuniform current distribution that arises from a semiconductor's junction with a metal contact. Consider the geometry for which the current is flowing parallel to the surface of the semiconductor (Figure 4.4). As the current reaches the metal-semiconductor interface, the current has two options: continue flowing through the semiconductor or flow into the metal. As the current travels along the semiconductor, some amount enters the metal

at each node. The voltage drop V_{ms} across the metal-semiconductor junction is given by

$$V_{\mathrm{ms}} = i_{\mathrm{ms}} R_{\mathrm{ms}}, \tag{4.3}$$

where i_{ms} is the current flowing into the metal and R_{ms} is the metal-semiconductor resistivity in $\Omega\,\mathrm{m}$.

The voltage drop across the next junction will be smaller because of the current that has already left the semiconductor. That relationship in differential form is

$$\frac{\partial V_{\mathrm{ms}}(x)}{\partial x} = -r_{ss} i_{ss}, \tag{4.4}$$

where r_{ss} is the resistivity of the semiconductor-semiconductor interface in Ω/m.

Kirchoff's current conservation law provides the final equation. The amount of current lost along each semiconductor-semiconductor node is the current diverted to the metal

$$\frac{\partial i_{ss}(x)}{\partial x} = -i_{ms} \tag{4.5}$$

Combining Equations 4.3, 4.4, and 4.5 provides

$$\frac{\partial^2 V_{ms}(x)}{\partial x^2} = L_T^2 V_{ms}. \tag{4.6}$$

The solution to this differential equation is an exponential with the characteristic length L_T, called the transfer length, given by,

$$L_T = \sqrt{\frac{R_{\mathrm{ms}}}{r_{\mathrm{ss}}}}. \tag{4.7}$$

Based on the values in Table 4.1, the transfer length of this system is $L_T = 1.35\,\mu\mathrm{m}$.

Returning now to the simulation, the current through each metal-semiconductor node junction is calculated,

$$I_i = (V_{\mathrm{m_i}} - V_{\mathrm{s_i}}/R_{\mathrm{ms}}). \tag{4.8}$$

This simulation accurately models the exponential decrease in current entering the metal as a function of distance into the electrode. In the case of the square electrode, the current fell to $1/e$ of its original value at a distance of $\lambda = 1.27\,\mu\mathrm{m}$, within $6\,\%$ of its expected value of $L_\mathrm{T} = 1.3\,\mu\mathrm{m}$. The results are shown in Figure 4.8.

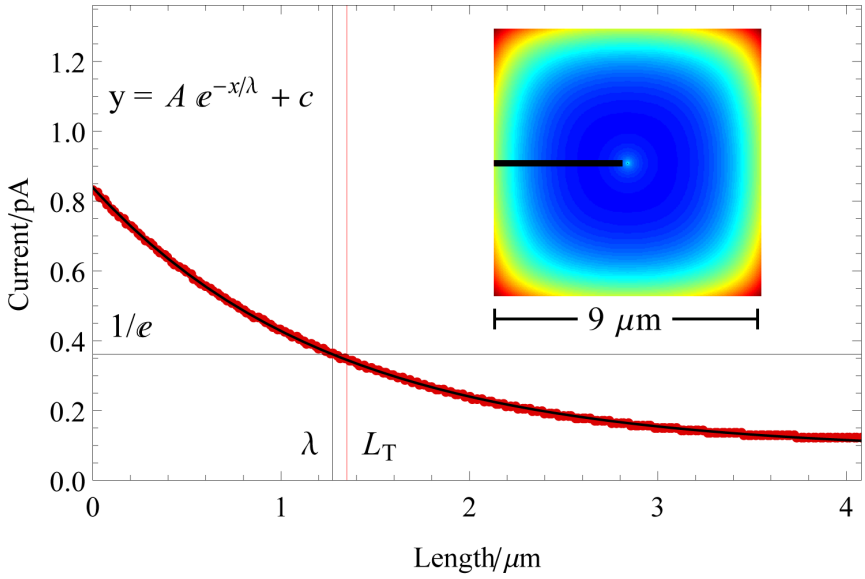

FIGURE 4.8. Photodiode simulation results for the square top contact exhibiting current crowding. The current entering the metal from the semiconductor falls off exponentially as a function of distance into the electrode. The characteristic length λ of the fit line is within $6\,\%$ error from the expected transfer length $L_T = 1.3\,\mu\mathrm{m}$. The current falls to $37\,\%$ of its original value by this length scale.

The current crowding effect is ruinous for an H tree design with such narrow fingers, Figure 4.9. At the contact's widest point, the current transfer only drops from $0.786\,\mathrm{pA}$ to $0.777\,\mathrm{pA}$ over a distance of $140\,\mathrm{nm}$. This is only a $1\,\%$ decrease in current transferred to the metal. Beyond $140\,\mathrm{nm}$, the current entering the metal is forced to increase because of current continuity. The current must make it to ground, regardless of the resistance.

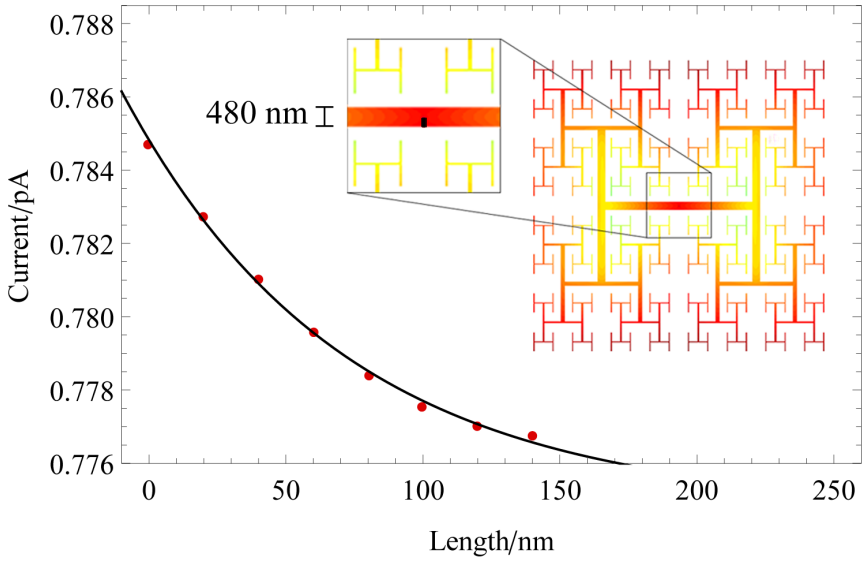

FIGURE 4.9. Photodiode simulation results for the H tree top contact exhibiting current crowding. The amount of current transferred as a function of distance falls by only $1\,\%$ of its original value. The majority of the current flows underneath the metal to the ground at the center of the electrode and is forced through at high resistive loss. The terrible performance of this contact is due to the narrow widths of the H tree fingers.

A possible solution to avoid the narrow fingers of the H tree but also extend the reaches of the square contact would be to use a Sierpinski carpet as a top contact. A Sierpinski carpet covers $(1 - 8^n/9^n) \times 100\%$ of its surface area. A two iteration Sierpinski carpet would then cover $80\,\%$ of the photodiode, but the average distance a carrier would have to travel through the semiconductor would be shorter and the top contact's narrowest width would be $2.2\,\mu\text{m}$. Modifying the geometry of the Sierpinski carpet to decrease coverage and maintain wide contacts could prove beneficial for both aspects. This idea will be revisited in Chapter V.

4.2. Electric Field Simulations

This section will explore the effects of using a fractal geometry for an electrode to stimulate neurons. Neurostimulation is performed in an electrolytic fluid with an AC

electric field. The electric field emanating from the electrode depolarizes the neuron, initiating the propagation of an electrochemical signal in the neuron. As a first step towards understanding the effects of using a fractal electrode, the DC electric field emanating into a vacuum is studied using the finite element method. A fractal geometry that produces an equivalent electric field to that of a square electrode is presented.

The photodiode from the previous section operates in short circuit mode with an ammeter in series, refer to Figure 1.2. A voltage amplifier that is regulated by the value of the ammeter applies a voltage to the stimulating electrode. Electrical simulations determine the effects of designing the stimulating electrode with a fractal geometry.

COMSOL Multiphysics is a software engine designed to simulate different kinds of physics applied to computer-aided design (CAD) geometries [61]. It solves problems using the finite element method. This is a numerical technique that reiteratively solves boundary value problems for many neighboring volume elements until a steady state solution is found. A limiting factor in the solution of problems with fractal geometries using the finite element method is the number of volume elements for which the relevant physics needs to be solved. The multiscale behavior of a fractal necessitates solving physics for small features over long distances. This limits the feasible number of iterations in any model. Up to four iterations of an H tree, spanning 1.2 decades, are modeled in these simulations.

The relevant physics explored here is Laplace's equation,

$$\nabla^2 V = 0, \tag{4.9}$$

which states that the divergence of the gradient of the electric field potential V is 0 when there are no free charges. The geometry consists of a $20\,\mu\text{m} \times 20\,\mu\text{m}$ square region. A ground electrode ($1\,\mu$m wide) follows the perimeter of the square. At the center is

a $10\,\mu m \times 10\,\mu m$ stimulating electrode, see Figure 4.10. The height of the stimulating and ground electrodes is $1\,\mu m$. The Dirichlet boundary conditions are a voltage on the stimulating electrode set to $1\,V$ and the ground electrode set to $0\,V$. The electrode is situated in free space with the potential going to zero at infinity. The material properties of the simulation were set such that the metal electrode is a perfect conductor (i.e. $\rho = 0\,\Omega\,m$) and the permittivity of the medium is ϵ_0.

The first four iterations of an H tree are compared to a square electrode design. The electric potentials of three designs (H2, H4, and the square) are shown in Figure 4.10. The lower iterations, such as H2, have electric potentials that fall off faster with distance from the electrode. As the number of iterations of the H tree increases, the electric potential behaves more similarly to the square electrode. The surface areas of the square electrode and the four iterations of the H tree are given in Table 4.2. The increased surface area on the interior of the fractal electrode does not contribute to the electric potential. This shielding of the interior of the electrode is the Faraday cage in effect. The relevant metric here is the amount of metal that lies on the bounding perimeter. The square's actual perimeter and bounding perimeter is the same. The higher iterations of the H tree have more metal on the bounding perimeter and thus approach the same behavior as the square electrode.

	Square	H1	H2	H3	H4
Surface area / μm^2	96	20	72	160	340

TABLE 4.2. Surface areas of various electrode geometries with a height of $1\,\mu m$.

The average of the electric field $\mathbf{E}$ in the plane as a function of distance above each electrode is shown in Figure 4.11. The electric field falls off fastest for H1, but at near equivalent rates for H4 and the square.

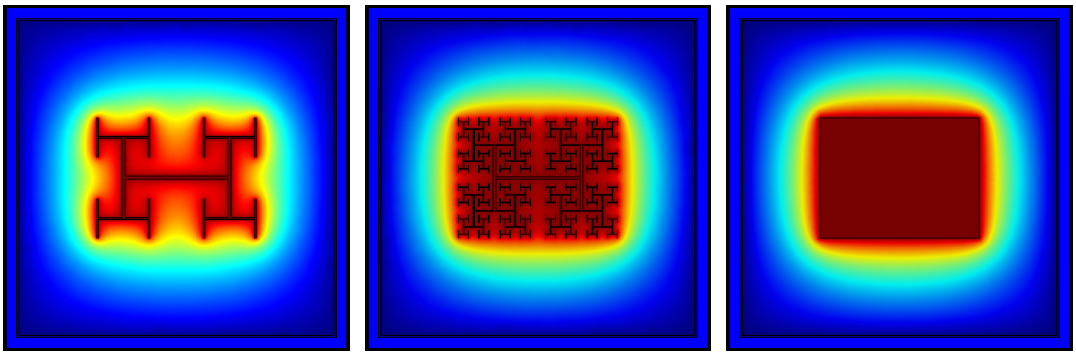

(a) (b) (c)

FIGURE 4.10. The geometry of a fractal electrode can be tuned such that the way the electric potential extends into space matches that of the square electrode. Each image shows the electric potential of an electrode with a rectangular ground on the perimeter of the image. (a) H2 and (b) H4 have the same fractal dimension ($D_{\mathrm{f}} = 2$). The electric potential of (b) H4 and (c) the square electrode are effectively equivalent.

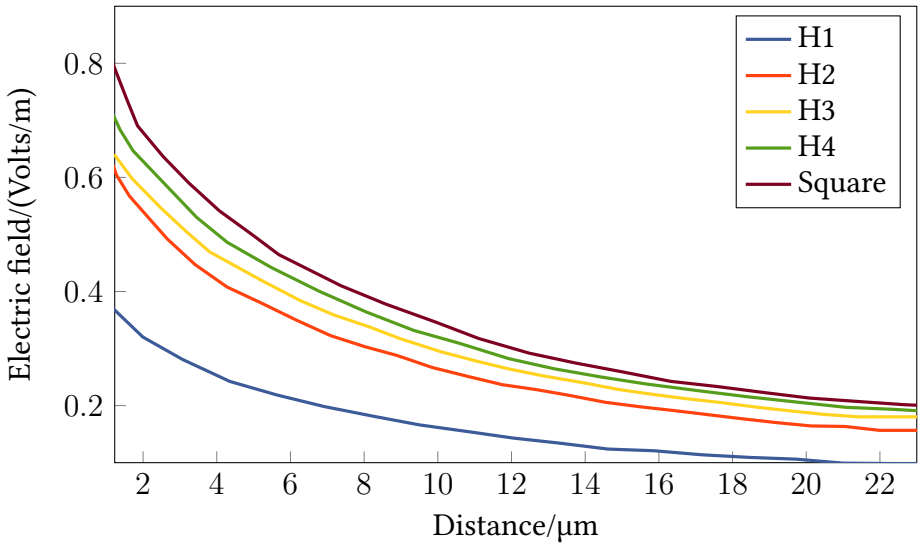

FIGURE 4.11. Average of the electric field versus distance above the electrode for four iterations of the H tree and the square electrode. The behavior of the electric field tends to that of the square for higher iterations of the H tree.

It is not feasible to experimentally measure the electric field at all points in space. Rather, the capacitance of the electrodes would be measured. The capacitance of the higher iteration fractal electrodes approaches that of the square. Gauss' law states that the electric field $\mathbf{E}$ integrated over a surface S is equal to the charge enclosed Q_{enc}, or

$$Q_{enc} = \epsilon_0 \oint_S \mathbf{E} \cdot d\mathbf{A}. \tag{4.10}$$

When a voltage difference V is applied between the stimulating electrode and the ground electrode, the charge Q is distributed through the system. The capacitance C determines the amount of charge Q necessary to produce the voltage difference V and is given by

$$C = \frac{Q}{V}. \tag{4.11}$$

The integral of the electric field flux through the surface of a Gaussian cube provides the charge enclosed Q_{enc}. The capacitances of the electrodes are calculated with the charge Q_{enc} and the applied voltage V. The capacitances are shown in Figure 4.12. The results indicate that the capacitance of an H tree electrode tends to that of the square electrode, as the number of iterations increases.

To summarize, a voltage is applied to the stimulating electrode. The electric field in space is calculated using the finite element method. Integrating the electric field flux through a Gaussian surface provides the charge enclosed. The capacitance then is calculated via the measured charge and the applied voltage.

The square and H4 have effectively the same charge, but different surface areas and therefore different charge densities. That is, when the voltage of an electrode is set, the charge density is dependent on the particular geometry. The charge density, and thus the local electric field, will be higher at the four corners of the square and at each of the H's

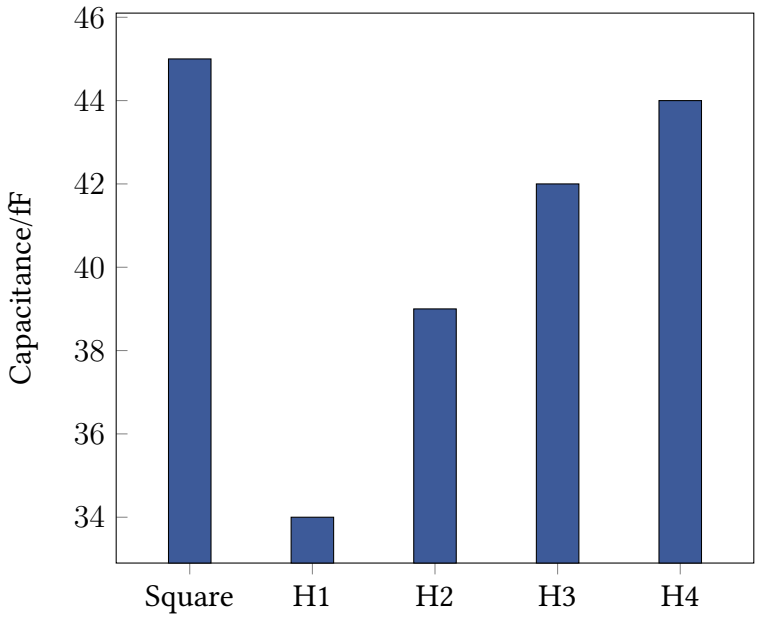

FIGURE 4.12. The calculated capacitances for five different electrode geometries, a square and four iterations of an H tree. The capacitance of the H tree tends to that of the square electrode for higher iterations of the H tree.

needle-like protrusions at the boundary. At a distance, these local maxima for the square and H4 are averaged out and the average electric fields approach the same value. The result is that the electric field emanating from an electrode with thin fingers and gaps is the same as that of a square electrode, as long as the actual perimeters and the bounding perimeters are equivalent. This result is significant because the electrical performance of the electrode need not be forfeited while, as we shall see in the next section, the adhesion of neurons is enhanced by these fine features.

4.3. Neural Adhesion

An experiment for neural adhesion is performed by culturing mouse retinal cells on various substrates and measuring the resultant cell density and neurite growth. The technique will be described briefly here, but there are more in-depth explanations elsewhere [62]. The retinal neurons are removed from the retinal pigment epithelium

and are mechanically agitated in solution. They are then filtered through a $20\,\mu m$ mesh filter to break off existing axons and dendrites such that the soma can regrow neurites once on the substrate. The somas are deposited on the sample substrate and kept in a clean environment to grow. After three days, the neurons are fixed in place and stained for fluorescent microscopy. The neuron nuclei are stained blue with 4',6-diamidino-2-phenylindole (DAPI). Neurons are stained red with β-tubulin III. Glial cells, which act as physical and nutritional support for the neurons, are tagged with the green fluorescent protein (GFP) and thus fluoresce green.

Neurons attach to a substrate through a series of connections. Transmembrane receptors (integrins) on the surface of the neuron attach to the extracellular matrix (ECM) proteins, which themselves bind to proteins (e.g. arginylglycylaspartic acid (RGD)) on the surface of the substrate. The ECM is the framework of molecules outside the cell that the cell uses to interact with its environment. Actively controlling the arrangement of binding proteins on the substrate has been shown to improve adhesion [63, 64]. The experiments presented here do not control the placement of binding proteins on the surface, but allow the binding proteins from the solution to settle on the surface. This method tests the dependence of adhesion by topography alone.

The topography of the substrate can affect neuron adhesion in a number of ways [65, 66]. The total number or concentration of binding proteins can be influenced by topography. The substrate stiffness plays a role in the binding strength. Localized charge buildup on the surface of the substrate can also affect protein binding. Furthermore, the cell is not a passive object. It can try to maximize its own interaction area with the environment. This is believed to be the reason that neurons have a strong adhesion with nanorods [67–69].

These experiments are designed to test the adhesion of retinal neurons to two types of materials and a number of different topographies. The electrode materials tested here are HafSOx and SU-8, with and without HfO_2 coatings.

4.3.1. HafSOx Electrode

The fabrication process for the HafSOx electrodes was described in Chapter III. The substrates tested have six electrode designs, each $100\,\mu m \times 100\,\mu m$, and spaced $400\,\mu m$ apart. The designs include an H tree, an angled H tree, a Sierpinski carpet, a fractal arrangement of pillars, a regular array of pillars, and a square. See Figure 4.13 for designs and site locations. The different designs are distributed through twenty-five sites per substrate to account for local fluctuations in cell density.

The HafSOx electrodes without the HfO_2 layer are able to support neuron survival. However, none of the designs show that the neurons prefer to attach to or grow near the electrode designs. An example of the results are shown in Figure 4.14.

The substrates that are coated with $3\,nm$ of HfO_2 show an increase in cell attachment and neurite outgrowth compared to the substrates without HfO_2. However, there is still no preference for the electrode sites. An overview of the substrate and a closer look at the neurons is shown in Figure 4.15. The $20\,nm$ heights of the HafSOx structures are too short to elicit a response in the neurons. This result is applicable to the photodiode aspect of the retinal implant. If the neurons do not respond to structures with heights up to $250\,nm$, then the neurons will not crowd the photodiode by adhering to the top contact.

4.3.2. SU-8 Electrode

The fabrication process for the SU-8 electrodes was described in Chapter III. These electrode designs are fabricated with a height of $2\,\mu m$. While SU-8 is an easy-to-use

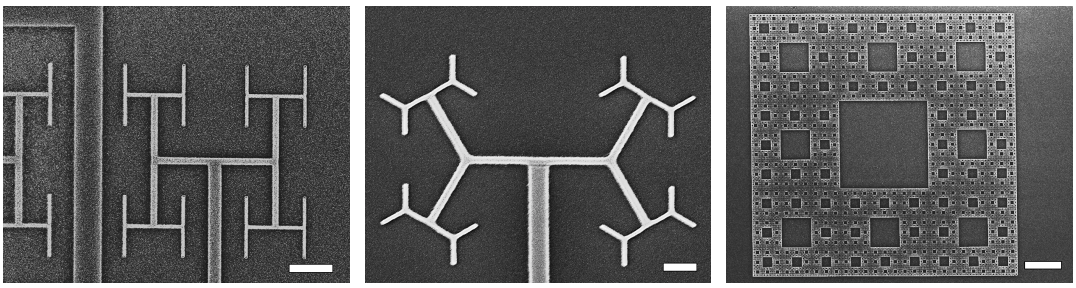

(a) (b) (c)

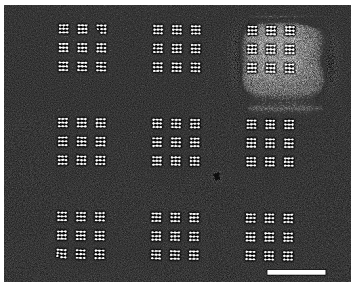

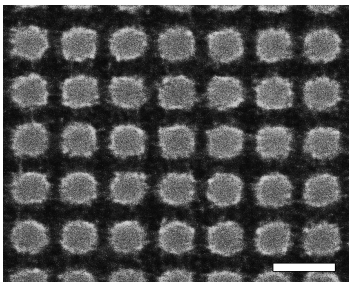

1	2	3	4	5
3	4	5	6	1
5	6	1	2	3
1	2	3	4	5
6	4	1	2	6

(d) (e) (f)

FIGURE 4.13. HafSOx electrode designs and site locations. (a) H tree, scale bar is 1 µm. (b) Angled H tree, scale bar is 200 nm. (c) Sierpinski carpet, scale bar is 2 µm. (d) Fractal array of pillars, scale bar is 1 µm. (e) Regulary array of pillars, scale bar is 200 nm. (f) The electrode designs are arranged on the substrate in such a way as to reduce the effect of random local fluctuations in neuron density. The numbers correspond to the designs: 1 H tree, 2 Angled H tree, 3 Sierpinski carpet, 4 Fractal array of pillars, 5 Regular array of pillars, 6 Square platform. Images taken by Kurtis Fairley.

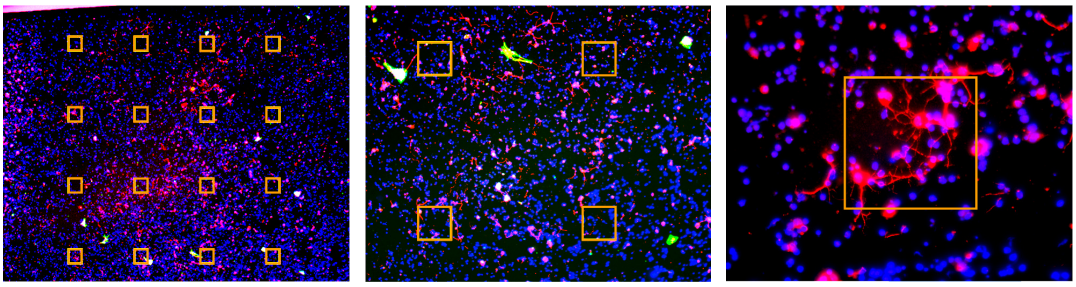

(a) (b) (c)

FIGURE 4.14. Fluorescence microscopy images of HafSOx electrodes without the HfO_2 coating. Each box is 100 µm wide. The staining process dyes nuclei blue, neurons red, and glial cells green. The homogeneous distribution of staining indicates that there is no preferential adhesion for the electrodes.

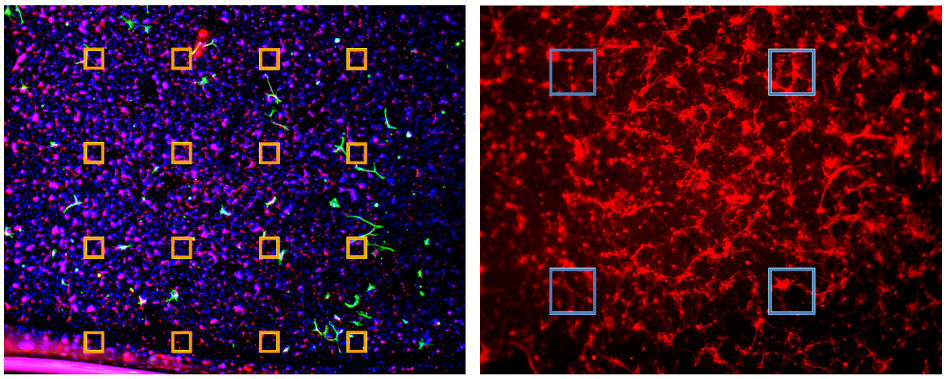

(a) (b)

FIGURE 4.15. Fluorescence microscopy images of HafSOx electrodes with a 3 nm coating of HfO_2. Each box is 100 µm wide. There is no preferential adhesion for the electrode sites. The 20 nm electrodes are too short to evoke a response from the neurons.

photoresist for lithography, it is known to be toxic to neurons [70–72]. Three different processing methods are used to combat this cytotoxicity. The unprocessed SU-8 acts as a control. The first processing method covers the photoresist with a 20 nm layer of HfO_2. The second method employs a three day hard bake at 150 °C. This is believed to increase neuronal viability by completing the cross-linking process in the photoresist, removing toxic molecules, or changing the surface characteristics of the photoresist [70]. The third method employs the three day hard bake and then coating with HfO_2.

Each sample comprises three control electrodes and an H tree of one fractal dimension in a 4×4 site configuration, shown in Figure 4.16. The electrodes are 500 µm wide and spaced 500 µm apart. Three different fractal dimensions, $D_f = 1.5$, 1.7, and 2.0, are used for the H tree in different samples to test whether one fractal dimension performs better than the others. The controls include a square with the same bounding area as the fractal patterns (500 µm × 500 µm), a square with the same surface area as the fractal patterns (52 µm × 52 µm), and a regular array of small Hs that match the smallest iteration H in the fractal. These designs are chosen to differentiate the effects that surface area (large square versus small square), large edges (H tree versus small Hs), and

multiscale features (H trees of different D_{f}) have on the adhesion and growth of neurons. The contributing factors may include the concentration of proteins that can build up on the different geometries, the number of edges that the neuron's growth scheme can detect, and any resonances between the shape of the neuron and the geometry of the electrode.

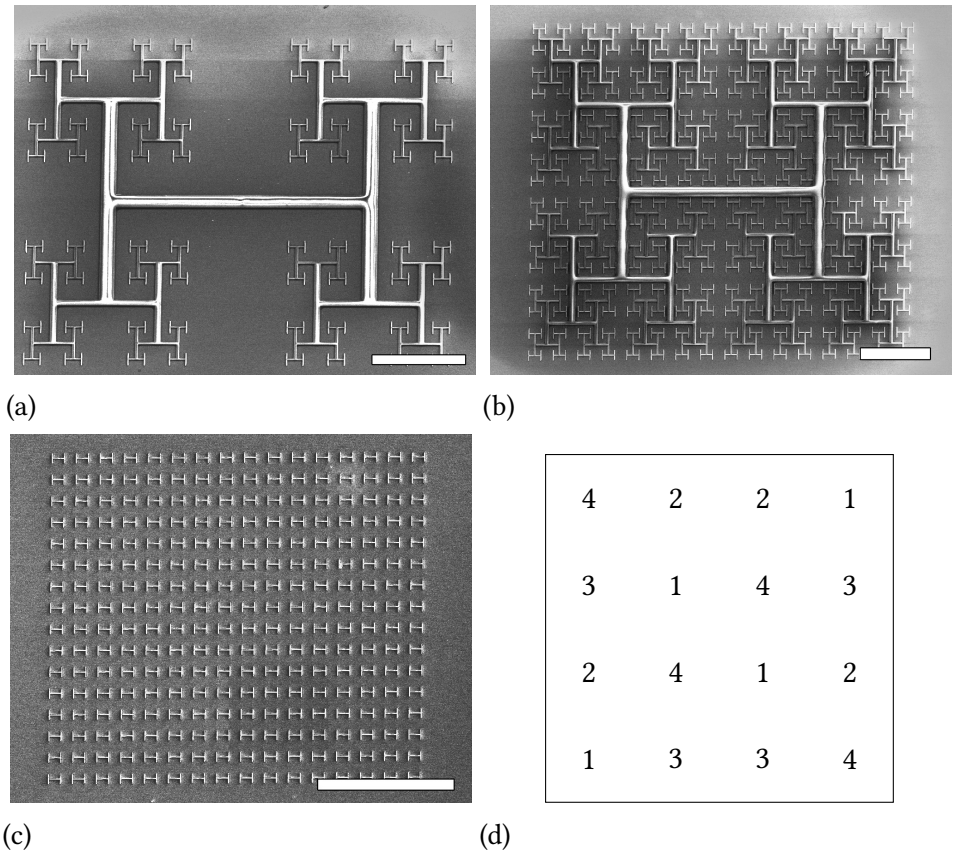

FIGURE 4.16. SU-8 electrode designs and site locations. Each substrate has only one H tree of a particular D_{f}, an array of small Hs, a square platform equal in surface area to the fractal design, and a square platform with the same bounding area. (a) H tree of $D_{\mathrm{f}} = 1.5$, scale bar is $100\,\mu$m. (b) H tree of $D_{\mathrm{f}} = 2$, scale bar is $100\,\mu$m. (c) Array of small Hs, scale bar is $200\,\mu$m. (d) The electrode designs are arranged on the substrate in such a way as to reduce the effect of random local fluctuations in neuron density. The numbers correspond to the designs: 1 H tree, 2 Array of small Hs, 3 Small square, 4 Large square. Images taken by Bill Watterson.

The raw images from fluorescence microscopy are processed to measure the adhesion as a function of processing method and electrode design. The adhesion performance is

measured by cell density in each electrode area and a random unpatterned spot ($500\,\mu m \times 500\,\mu m$) between electrodes, as an extra control. The raw images are thresholded and separated into clusters of nuclei, single nuclei, and stray counts, see Figure 4.17. The numbers of clusters and single nuclei above the electrode are summed and divided by the area that the electrode spans.

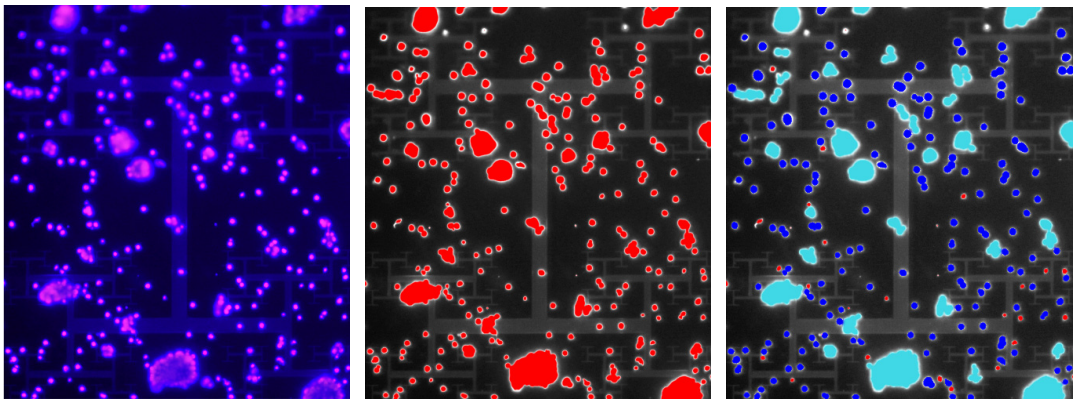

(a) (b) (c)

FIGURE 4.17. The thresholding and counting process to calculate the area of an electrode occupied by neurons. (a) The image is cropped to the area bounded by the electrode design. (b) A thresholding filter roughly selects the relevant nuclei. (c) The nuclei are divided into clusters (cyan), singles (blue), and stray selections that are not counted (red). Images taken by Bill Watterson.

The results are charted in Figure 4.18. The processing method that includes the hard bake and HfO_2 coating performs best. It is curious that the hard bake method alone performs worse than the control, considering the results of other experiments [70]. The performance benefits of the electrode designs for any one processing method are not immediately apparent. For the substrate that is both hard baked and coated with HfO_2, the large square electrode outperforms the others, but there is an uneven distribution of nuclei across the substrate as a whole. Overall, the results suggest that hard baking and coating the SU-8 in HfO_2 is beneficial, but more experiments are necessary to understand the effects of the different electrode geometries. The highest cell density is reported at

5200 cells/mm^2, indicating that this SU-8 treatment is a viable technique for retinal cell cultures.

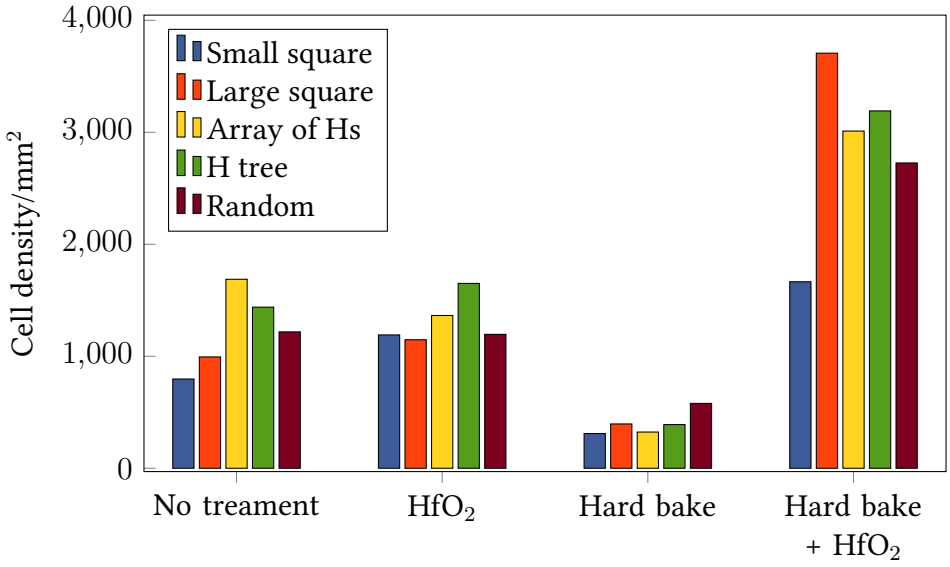

FIGURE 4.18. Cell density above each test pattern for the four substrate processing methods and an unpatterned test area that is chosen at random between electrode sites. The preliminary results indicate that the hard bake plus HfO_2 coating create a better environment for the neurons than the other methods of treating SU-8 for cytocompatibility. Within that treating method, the small square performs the worst. However, more experiments are necessary to generate the statistics to make meaningful statements.

A problem arose during the experiments that needs to be addressed in the future, see Figure 4.19. The appearance of nuclei outside the substrate area means that some cells were likely washed off of the substrate and onto the microscope slide during the staining stage. On another sample substrate, there was an inhomogeneous distribution of neurons that cannot be accounted for by the presence of the electrodes. This suggests that, although the cells were growing along the topography, some did not firmly attach to the substrate and were removed during staining.

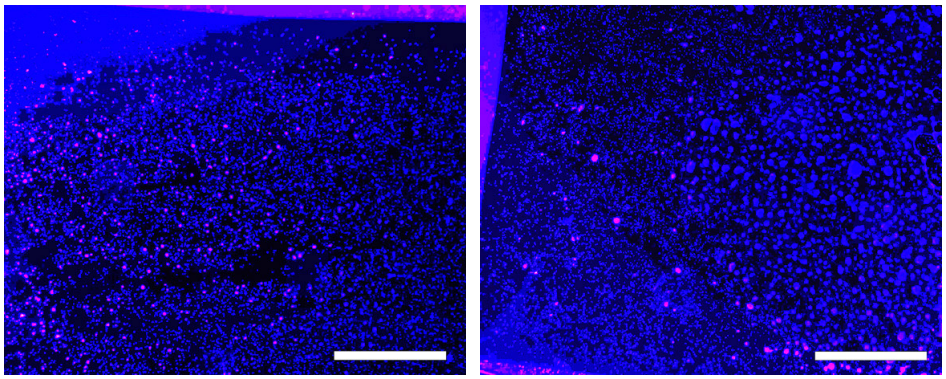

(a) (b)

FIGURE 4.19. Fluorescence microscope images showing the accidental removal of neuron nuclei during staining. The nuclei are stained blue using DAPI. Overexposing the image changes the color of the cells to pink. The appearance of cells on the microscope slide indicate that they were washed off of the substrate during the staining stage. The scale bars are 2 mm. (a) There are nuclei appearing on the microscope slide (top-right corner) indicating that they came loose during the staining stage. (b) The nuclei were not distributed uniformly across the substrate. The left half of this substrate may have lost neurons during staining. Images taken by Bill Watterson.

There are examples of neurites growing along the H trees (Figure 4.20). This growth behavior strengthens the hypothesis that certain electrode geometries will not only be compatible, but beneficial, to the adhesion of neurons on substrate surfaces.

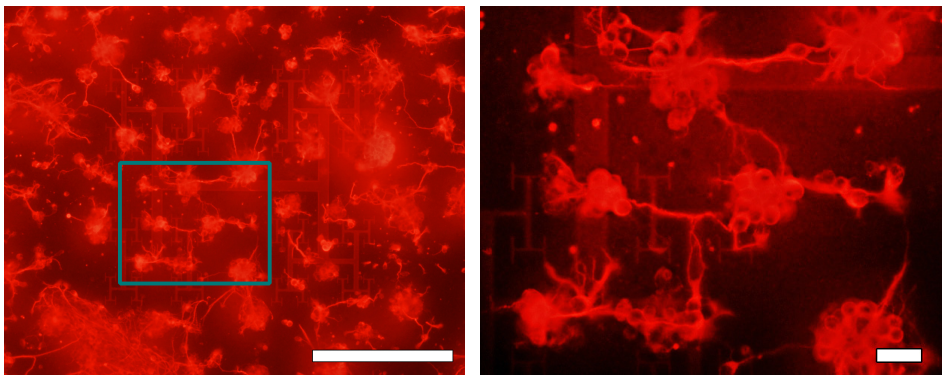

(a) (b)

FIGURE 4.20. Fluorescence micrographs of neurites growing along an H tree electrode. The box from (a) is magnified in (b). Neurites growing along the topography of the fractal pattern take 90° turns to remain attached to the electrode. Scale bar in (a) is $200\,\mu\text{m}$ and in (b) is $20\,\mu\text{m}$. Images taken by Bill Watterson.

CHAPTER V

CONCLUSION

This chapter briefly highlights the results of this dissertation while introducing the framework for where this research will go next. In Section 5.1, a research proposal for a retinal implant that can provide color vision is introduced. This section draws from many research ideas explored through this dissertation. Section 5.2 focuses on a more realistic simulation for neural stimulation. Rather than simulating the electric field in free space, an electrolytic fluid is introduced. The presence of a conducting medium necessitates an AC electric field.

5.1. Artificial Color Vision

Along with reducing the resistive losses in the photodiode, a fractal top contact can provide another special feature by enhancing transmission at selective wavelengths. A surface plasmon polariton (SPP) is an electromagnetic wave that can travel along a metal-dielectric interface. Light incident on the metal film can create create SPPs that enhance the transmittance of light at certain wavelengths [73–75]. The holes in the metal film act as a diffraction grating creating constructive interference. Enhanced transmission occurs at wavelengths associated with the hierarchy of hole sizes, which is related to the fractal dimension.

Three different fractal top contacts will be designed with different values of D_{f} that selectively enhance the transmission of visible light at the red, green, and blue (RGB) wavelengths. A color sensitive retinal implant can be created by organizing the photodiode array into RGB triplets. This new feature is quickly met by a new problem. A red photodiode is useless without the ability to connect to a "red" bipolar cell. A recent

study on the retinas of zebrafish found that at least some of the cone-specific bipolar cells have unique dendritic tree morphologies [76]. While the zebrafish retina is different from the human retina, the fact that there are generally 10–13 different types of bipolar cells in mammals [77] suggests that there may be some selective features between types of bipolar cells in humans as well. As an illustrative example, one such color sensitive photodiode / stimulating electrode pair is shown in Figure 5.1. The next generation of neural adhesion experiments will aim to find electrode geometries that promote adhesion with specific dendritic patterns.

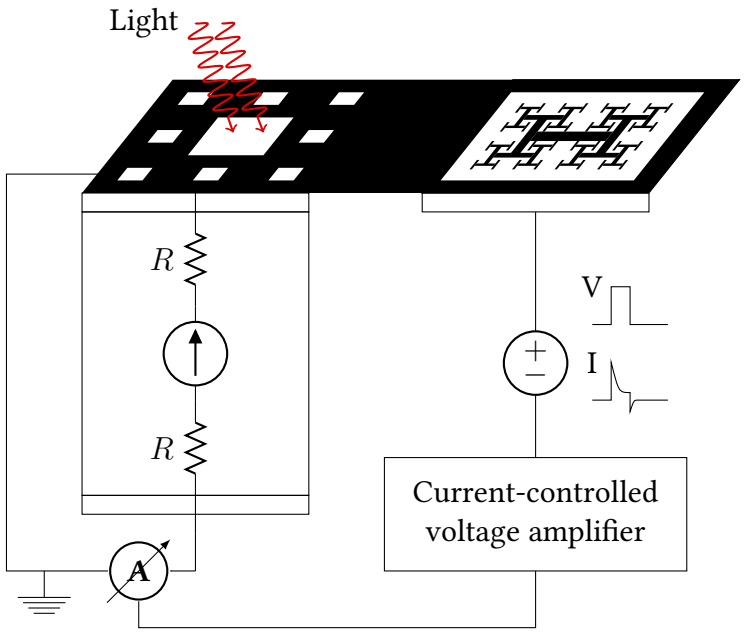

FIGURE 5.1. Schematic of the proposed geometry for a photodiode / stimulating electrode pair in a subretinal implant. The photodiode operates in short circuit mode with the grounded top contact electrically connected to the grounded perimeter of the stimulating electrode geometry. The stimulating electrode delivers a square voltage pulse. The amplitude is controlled by the amount of current generated by the photodiode, up to a maximum of $1.5\,\mathrm{V}$. This $1.5\,\mathrm{V}$ limit exists to inhibit electrolysis. The voltage pulse creates a charge-balanced current that depolarizes the neuron to induce a signal in the neuron. After a millisecond interval, which assures the neuron is stimulated, the current is reversed to avoid any unwanted electrochemistry deteriorating the surface of the electrode. This also allows time for the neuron to return to its resting state.

A user-friendly front end will be developed for the box counting analysis and best-of-R^2 fitting procedure. These tools will be used to assess the morphologies of retinal bipolar cells. The results of those studies will inform the next set of experiments in neural adhesion.

Three factors affecting neural adhesion (surface area, edge concentration, and resonant geometry) will be isolated using various electrode geometries (Figure 4.16). Recall that the neuron adheres to proteins on the surface by way of the extracellular matrix. The amount of accessible protein is a function of surface area. This factor will be tested by varying the size of square electrodes. The presence of edges is known to be beneficial for neural adhesion [62, 69]. The concentration of edges will be tested by comparing adhesion to the H tree and to the array of small Hs, refer to Figure 4.16. The preliminary results show that the neurites will take 90° turns in order to stay attached to the electrode. The idea behind testing resonant geometry is that although the neuron will grow along a surface in spite of sharp turns, is there a geometry commensurate to the neuron's natural shape that can promote adhesion to an even greater degree? Testing fractal electrodes of varying D_f will answer this question. Most excitingly, do neurons with different dendritic morphologies prefer electrodes that resonate with their geometry?

The ultimate goal is to fabricate a photodiode array of RGB triplets, where, for example, red light incident on a red photodiode creates a stimulating electric field emanating from a "red" stimulating electrode. If successful, this would be the first retinal implant with the ability to restore color vision.

5.2. AC Simulations

Neuron do not exist in free space, but live inside the body. To move beyond the simulations from Chapter IV, an electrolytic fluid must be introduced into the simulation.

The ions in this fluid respond to the static electric field by rearranging themselves to cancel the field, just like in a metal conductor. However, unlike in a metal conductor, it does take an appreciable amount of time for these ions to rearrange. The stimulating electrode is given a square voltage pulse, inducing a charge-balanced current, refer to Figure 5.1. The cathodic pulse comes first, depolarizing the neuron. A millisecond delay ensures the neuron will be stimulated by the electric field emanating from the electrode. The anodic pulse is then delivered to restore charge balance. Balancing the charge is necessary to inhibit the release of ions from the electrode into the body due to unwanted electrochemistry at the surface.

Rather than using COMSOL's finite element method, the new simulations are carried out using modified nodal analysis (MNA). MNA takes the above dynamics into account by creating an equivalent circuit model with an electrode-electrolyte surface capacitance and a bulk fluid resistivity. The simulation solves for the time varying potential between the stimulating electrode and the grounded perimeter electrode.

The goal of these simulations is to model the neuron as a passive component first and eventually an active component in the circuit. The cell walls of the neuron have both a surface capacitance and resistance. When modeled as an active component, the neuron's cell walls will also include a variable resistance. In this way, a voltage applied to the stimulating electrode will affect the potential on the inside of the neuron. The neuron will transmit its signal when the membrane potential of the soma passes a threshold. Once these simulations are working, the effect of various electrode geometries will be tested. The most efficient geometries can then be fabricated for use in a retinal implant.

5.3. Fiat Lux

The future is bright. It's only a matter of time before one of the proposed solutions to blindness reaches a breakthrough that makes quality vision available and affordable. With one epiretinal implant already approved by the FDA, the path is cleared for more retinal implants to follow. The subretinal implant architecture has the obvious advantage of utilizing the body's builtin retinal circuitry. A subretinal implant with color vision would be a sight for sore eyes, indeed.

REFERENCES CITED

[1] R. Ratnapriya and E. Y. Chew. Age-related macular degeneration-clinical review and genetics update. *Clin. Genet.*, 84(2):160–166, August 2013.

[2] G. S. Hageman. Age-Related Macular Degeneration. http://webvision.med.utah.edu/book/part-xii-cell-biology-of-retinal-degenerations/age-related-macular-degeneration-amd/. Date Accessed: 10/31/2014.

[3] B. Foundation. Macular Degeneration Facts & Statistics. http://www.brightfocus.org/macular/about/understanding/facts.html. Date Accessed: 10/31/2014.

[4] D. T. Hartong, E. L. Berson, and T. P. Dryja. Retinitis pigmentosa. *Lancet*, 368(9549): 1795–1809, November 2006.

[5] A. E. Fung, G. A. Lalwani, P. J. Rosenfeld, S. R. Dubovy, S. Michels, W. J. Feuer, C. A. Puliafito, J. L. Davis, H. W. Flynn, and M. Esquiabro. An optical coherence tomography-guided, variable dosing regimen with intravitreal ranibizumab (Lucentis) for neovascular age-related macular degeneration. *Am. J. Ophthalmol.*, 143(4):566–583, April 2007.

[6] S. D. Schwartz, C. D. Regillo, B. L. Lam, D. Eliott, P. J. Rosenfeld, N. Z. Gregori, J.-P. Hubschman, J. L. Davis, G. Heilwell, M. Spirn, J. Maguire, R. Gay, J. Bateman, R. M. Ostrick, D. Morris, M. Vincent, E. Anglade, L. V. Del Priore, and R. Lanza. Human embryonic stem cell-derived retinal pigment epithelium in patients with age-related macular degeneration and Stargardt's macular dystrophy: follow-up of two open-label phase 1/2 studies. *Lancet*, October 2014.

[7] S. Nirenberg and C. Pandarinath. Retinal prosthetic strategy with the capacity to restore normal vision. *Proc. Natl. Acad. Sci.*, 109(37):15012–15017, August 2012.

[8] R. P. Taylor. Vision of beauty. *Phys. World*, 24(May):22–27, May 2011.

[9] H.-C. Lee, S.-C. Wu, T.-C. Yang, and T.-J. Yen. Efficiently Harvesting Sun Light for Silicon Solar Cells through Advanced Optical Couplers and A Radial p-n Junction Structure. *Energies*, 3(4):784–802, April 2010.

[10] C. Sekirnjak, P. Hottowy, A. Sher, W. Dabrowski, A. M. Litke, and E. J. Chichilnisky. High-resolution electrical stimulation of primate retina for epiretinal implant design. *The Journal of Neuroscience*, 28(17):4446–4456, 2008.

[11] A. Y. Chow, V. Y. Chow, K. H. Packo, J. S. Pollack, G. A. Peyman, and R. Schuchard. The artificial silicon retina microchip for the treatment of vision loss from retinitis pigmentosa. *Arch. Ophthalmol.*, 122(4):460–469, April 2004.

[12] M. S. Humayun, J. D. Weiland, G. Y. Fujii, R. Greenberg, R. Williamson, J. Little, B. Mech, V. Cimmarusti, G. Van Boemel, G. Dagnelie, and E. de Juan. Visual perception in a blind subject with a chronic microelectronic retinal prosthesis. *Vision Res.*, 43(24):2573–2581, November 2003.

[13] J. F. Rizzo, J. Wyatt, J. Loewenstein, S. Kelly, and D. Shire. Perceptual efficacy of electrical stimulation of human retina with a microelectrode array during short-term surgical trials. *Invest. Ophthalmol. Vis. Sci.*, 44(12):5362–5369, December 2003.

[14] E. Zrenner, K. U. Bartz-Schmidt, H. Benav, D. Besch, A. Bruckmann, V.-P. Gabel, F. Gekeler, U. Greppmaier, A. Harscher, S. Kibbel, J. Koch, A. Kusnyerik, T. Peters, K. Stingl, H. Sachs, A. Stett, P. Szurman, B. Wilhelm, and R. Wilke. Subretinal electronic chips allow blind patients to read letters and combine them to words. *Proc. Biol. Sci.*, 278(1711):1489–1497, May 2011.

[15] L. Greenemeier. FDA Approves First Retinal Implant. *Sci. Am.*, February 2013.

[16] Webvision. http://webvision.med.utah.edu/. Date Accessed: 10/31/2014.

[17] B. B. Mandelbrot. *The Fractal Geometry of Nature*. Henry Holt and Company, 1983. ISBN 0716711869.

[18] R. P. Taylor. Order in Pollock's Chaos. *Sci. Am.*, pages 116–119, December 2002.

[19] A. K. McAllister. Cellular and Molecular Mechanisms of Dendrite Growth. *Cereb. Cortex*, 10(10):963–973, October 2000.

[20] T. Witten and L. Sander. Diffusion-Limited Aggregation, a Kinetic Critical Phenomenon. *Phys. Rev. Lett.*, 47(19):1400–1403, November 1981.

[21] D. Avnir, O. Biham, D. Lidar, and O. Malcai. Is the Geometry of Nature Fractal? *Science*, 279(5347):39–40, 1998.

[22] Wolfram Research Inc. Mathematica, 2012.

[23] D. M. Bannerman, J. N. P. Rawlins, S. B. McHugh, R. M. J. Deacon, B. K. Yee, T. Bast, W.-N. Zhang, H. H. J. Pothuizen, and J. Feldon. Regional dissociations within the hippocampus–memory and anxiety. *Neurosci. Biobehav. Rev.*, 28(3):273–283, May 2004.

[24] Y. Mu and F. H. Gage. Adult hippocampal neurogenesis and its role in Alzheimer's disease. *Mol Neurodegener*, 6(1):85, 2011.

[25] H. Hampel, K. Bürger, S. J. Teipel, A. L. W. Bokde, H. Zetterberg, and K. Blennow. Core candidate neurochemical and imaging biomarkers of Alzheimer's disease. *Alzheimer's Dement. J. Alzheimer's Assoc. Assoc.*, 4(1):38–48, January 2008.

[26] M. Megffias, Z. Emri, T. Freund, and A. Gulyás. Total number and distribution of inhibitory and excitatory synapses on hippocampal CA1 pyramidal cells. *Neuroscience*, 102(3):527–540, February 2001.

[27] H. Lodish, A. Berk, S. L. Zipursky, P. Matsudaira, D. Baltimore, and J. Darnell. Overview of Neuron Structure and Function. In *Mol. Cell Biol.*, chapter 21. W. H. Freeman, New York, 4th editio edition, 2000.

[28] H. F. Jelinek and G. N. Elston. Dendritic Branching of Pyramidal Cells in the Visual Cortex of the Nocturnal Owl Monkey: a Fractal Analysis. *Fractals*, 11(4):391–396, December 2003.

[29] E. Fernández and H. F. Jelinek. Use of Fractal Theory in Neuroscience: Methods, Advantages, and Potential Problems. *Methods*, 24(4):309–321, 2001.

[30] F. Nooruddin and G. Turk. Simplification and repair of polygonal models using volumetric techniques. *IEEE Trans. Vis. Comput. Graph.*, 9(2):191–205, April 2003.

[31] H. F. Jelinek and E. Fernandez. Neurons and fractals: how reliable and useful are calculations of fractal dimensions? *J. Neurosci. Methods*, 81(1-2):9–18, June 1998.

[32] G. N. Elston and H. F. Jelinek. Dendritic Branching Patterns of Pyramidal Cells in the Visual Cortex of the New World Marmoset Monkey, With Comparative Notes on the Old World Macaque Monkey. *Fractals*, 9(3):297–303, September 2001.

[33] A. Karperien. FracLac, 2013. http://rsb.info.nih.gov/ij/plugins/fraclac/FLHelp/Introduction.htm. Date Accessed: 10/31/2014.

[34] W. Rasband. ImageJ. http://imagej.nih.gov/ij/. Date Accessed: 10/31/2014.

[35] J. T. Anderson, C. L. Munsee, C. M. Hung, T. M. Phung, G. S. Herman, D. C. Johnson, J. F. Wager, and D. A. Keszler. Solution-Processed HafSOx and ZircSOx Inorganic Thin-Film Dielectrics and Nanolaminates. *Adv. Funct. Mater.*, 17(13):2117–2124, September 2007.

[36] A. Telecky, P. Xie, J. Stowers, A. Grenville, B. Smith, and D. A. Keszler. Photopatternable inorganic hardmask. *J. Vac. Sci. Technol. B Microelectron. Nanom. Struct.*, 28(6):C6S19–C6S22, November 2010.

[37] MicroChem Corp. MicroChem SU-8 Negative Epoxy Series Resist, 2014. http://www.microchem.com/Prod-SU8_KMPR.htm. Date Accessed: 10/31/2014.

[38] S. A. Scott. *Self-assembly of Sb and Bi nanostructures on graphite*. PhD thesis, University of Canterbury, 2005.

[39] X. Zhai, W. Wang, G. Zhang, and B. He. Crystal Pattern Formation and Transitions of PEO Monolayers on Solid Substrates from Nonequilibrium to near Equilibrium. *Macromolecules*, 39(1):324–329, January 2006.

[40] A. Perez, P. Melinon, V. Dupuis, L. Bardotti, B. Masenelli, F. Tournus, B. Prevel, J. Tuaillon-Combes, E. Bernstein, A. Tamion, N. Blanc, D. Tainoff, O. Boisron, G. Guiraud, M. Broyer, M. Pellarin, N. Fatti, F. Vallee, E. Cottancin, J. Lerme, J.-L. Vialle, C. Bonnet, P. Maioli, A. Crut, C. Clavier, J. L. Rousset, and F. Morfin. Functional nanostructures from clusters. *Int. J. Nanotechnol.*, 7(4):523–574, January 2010.

[41] S. A. Scott, M. Kral, and S. Brown. Bi on graphite: Morphology and growth characteristics of star-shaped dendrites. *Phys. Rev. B*, 73(20):1–7, May 2006.

[42] S. A. Scott and S. A. Brown. Three-dimensional growth characteristics of antimony aggregates on graphite. *Eur. Phys. J. D*, 39(3):433–438, June 2006.

[43] P. Kowalczyk, O. Mahapatra, D. McCarthy, W. Kozlowski, Z. Klusek, and S. Brown. STM and XPS investigations of bismuth islands on HOPG. *Surf. Sci.*, 605(7-8): 659–667, April 2011.

[44] P. Mélinon, A. Hannour, B. Prével, L. Bardotti, E. Bernstein, A. Perez, J. Gierak, E. Bourhis, and D. Mailly. Functionalizing surfaces with arrays of clusters: role of the defects. *J. Cryst. Growth*, 275(1-2):317–324, February 2005.

[45] W. Lopes. Nonequilibrium self-assembly of metals on diblock copolymer templates. *Phys. Rev. E*, 65(3):1–14, February 2002.

[46] R. L. Chamousis, L. Chang, W. J. Watterson, R. D. Montgomery, R. P. Taylor, A. J. Moule, S. E. Shaheen, B. Ilan, J. van de Lagemaat, and F. E. Osterloh. Effect of fractal silver electrodes on charge collection and light distribution in semiconducting organic polymer films. *J. Mater. Chem. A*, 2(39):16608–16616, August 2014.

[47] K. Pielichowski and J. Njuguna. *Thermal degradation of polymeric materials*. Smithers Rapra Press, 2005. ISBN 978-1-85957-498-0.

[48] Y. Grohens, G. Castelein, P. Carriere, J. Spevacek, and J. Schultz. Multiscale Aggregation of PMMA Stereocomplexes at a Surface: An Atomic Force Microscopy Investigation. *Langmuir*, 17(1):86–94, 2001.

[49] S. Bywater and P. E. Black. Thermal Depolymerization of Polymethyl Methacrylate and Poly-α-methylstyrene in Solution in Various Solvents1,2. *J. Phys. Chem.*, 69 (9):2967–2970, 1965.

[50] K. Smolders and J. Baeyens. Thermal degradation of PMMA in fluidised beds. *Waste Manag.*, 24(8):849–857, January 2004.

[51] M. Fragalafi, G. Compagnini, L. Torrisi, and O. Puglisi. Ion beam assisted unzipping of PMMA. *Nucl. Inst. Methods Phys. Res. B*, 141(1-4):169–173, 1998.

[52] MicroChem Corp. MicroChem PMMA Positive Resists, 2014. http://www.microchem.com/Prod-PMMA.htm. Date Accessed: 10/31/2014.

[53] S. B. Darling and A. Hoffmann. Tuning metal surface diffusion on diblock copolymer films. *J. Vac. Sci. Technol. A Vacuum, Surfaces, Film.*, 25(4):1048, 2007.

[54] E. Cheever. Analysis of Resistive Circuits. http://www.swarthmore.edu/NatSci/echeeve1/Ref/mna/MNA1.html. Date Accessed: 10/31/2014.

[55] V. Litovski. *VLSI circuit simulation and optimization*. Springer, 1997.

[56] G. Guennebaud, B. Jacob, and Others. Eigen v3. http://eigen.tuxfamily.org. Date Accessed: 10/31/2014.

[57] X. S. Li. An Overview of {SuperLU}: Algorithms, Implementation, and User Interface. *ACM Trans. Math. Softw.*, 31(3):302–325, September 2005.

[58] D. C. Giancoli. *Physics: Principles With Applications*. Pearson Education, 2013. ISBN 9780321928894.

[59] C. Honsberg and S. Bowden. PVeducation.org. http://pveducation.org/. Date Accessed: 10/31/2014.

[60] D. K. Schroder. *Semiconductor Material and Device Characterization*. Wiley-IEEE Press, 2006. ISBN 978-0-471-73906-7.

[61] COMSOL Inc. COMSOL Multiphysics, 2011. http://www.comsol.com/. Date Accessed: 10/31/2014.

[62] G. Piret, M.-T. Perez, and C. N. Prinz. Neurite outgrowth and synaptophysin expression of postnatal CNS neurons on GaP nanowire arrays in long-term retinal cell culture. *Biomaterials*, 34(4):875–887, January 2013.

[63] E. A. Cavalcanti-Adam, T. Volberg, A. Micoulet, H. Kessler, B. Geiger, and J. P. Spatz. Cell spreading and focal adhesion dynamics are regulated by spacing of integrin ligands. *Biophys. J.*, 92(8):2964–2974, April 2007.

[64] M. Schvartzman, M. Palma, J. Sable, J. Abramson, X. Hu, M. P. Sheetz, and S. J. Wind. Nanolithographic Control of the Spatial Organization of Cellular Adhesion Receptors at the Single-Molecule Level. *Nano Lett.*, 11(3):1306–1312, 2011.

[65] G. Bugnicourt, J. Brocard, A. Nicolas, and C. Villard. Nanoscale Surface Topography Reshapes Neuronal Growth in Culture. *Langmuir*, 30(15):4441–4449, 2014.

[66] L. Micholt, A. Gärtner, D. Prodanov, D. Braeken, C. G. Dotti, and C. Bartic. Substrate topography determines neuronal polarization and growth in vitro. *PLoS One*, 8(6): e66170, 2013.

[67] W. Hällström, T. Mårtensson, C. Prinz, P. Gustavsson, L. Montelius, L. Samuelson, and M. Kanje. Gallium phosphide nanowires as a substrate for cultured neurons. *Nano Lett.*, 7(10):2960–2965, October 2007.

[68] W. Hällström, C. N. Prinz, D. Suyatin, L. Samuelson, L. Montelius, and M. Kanje. Rectifying and sorting of regenerating axons by free-standing nanowire patterns: a highway for nerve fibers. *Langmuir*, 25(8):4343–4346, April 2009.

[69] C. Prinz, W. Hällström, T. Mårtensson, L. Samuelson, L. Montelius, and M. Kanje. Axonal guidance on patterned free-standing nanowire surfaces. *Nanotechnology*, 19(34):345101, August 2008.

[70] V. N. Vernekar, D. K. Cullen, N. Fogleman, Y. Choi, A. J. García, M. G. Allen, G. J. Brewer, and M. C. LaPlaca. SU-8 2000 rendered cytocompatible for neuronal bioMEMS applications. *J. Biomed. Mater. Res. Part A*, 89(1):138–151, 2009.

[71] P. Xue, J. Bao, Y. J. Chuah, N. V. Menon, Y. Zhang, and Y. Kang. Protein Covalently Conjugated SU-8 Surface for the Enhancement of Mesenchymal Stem Cell Adhesion and Proliferation. *Langmuir*, 30(11):3110–3117, 2014.

[72] G. Blagoi, S. U. Keller, A. Johansson, A. Boisen, and H. M. Dufva. Functionalization of SU-8 Photoresist Surfaces with IgG Proteins. *Appl. Surf. Sci.*, 255(5):2896–2902, 2008.

[73] X. Huang, S. Xiao, D. Ye, J. Huangfu, Z. Wang, L. Ran, and L. Zhou. Fractal plasmonic metamaterials for subwavelength imaging. *Opt. Express*, 18(10): 10377–10387, May 2010.

[74] Y.-J. Bao, B. Zhang, Z. Wu, J.-W. Si, M. Wang, R.-W. Peng, X. Lu, J. Shao, Z.-f. Li, X.-P. Hao, and N.-B. Ming. Surface-plasmon-enhanced transmission through metallic film perforated with fractal-featured aperture array. *Appl. Phys. Lett.*, 90 (25):251914, 2007.

[75] G. Volpe, G. Volpe, and R. Quidant. Fractal plasmonics: subdiffraction focusing and broadband spectral response by a Sierpinski nanocarpet. *Opt. Express*, 19(4): 3612–3618, February 2011.

[76] Y. N. Li, T. Tsujimura, S. Kawamura, and J. E. Dowling. Bipolar cell-photoreceptor connectivity in the zebrafish (Danio rerio) retina. *J. Comp. Neurol.*, 520(16): 3786–3802, 2012.

[77] T. Euler, S. Haverkamp, T. Schubert, and T. Baden. Retinal bipolar cells: elementary building blocks of vision. *Nat. Rev. Neurosci.*, 15(8):507–519, July 2014.